

The EUMETSAT
Network of
Satellite
Application
Facilities



ROM SAF

Radio Occultation Meteorology

ROM SAF CDOP-2

Visiting Scientist Report 27:

**Development of wave optics code for the retrieval of
bending angle profiles for reflected rays**

Michael Gorbunov

Danish Meteorological Institute (DMI)
European Centre for Medium-Range Weather Forecasts (ECMWF)
Institut d'Estudis Espacials de Catalunya (IEEC)
Met Office (METO)

DOCUMENT AUTHOR TABLE

	<i>Author(s)</i>	<i>Function</i>	<i>Date</i>	<i>Comment</i>
Prepared by:	Michael Gorbunov	ROM SAF Visiting Scientist	10/05/2016	
Reviewed by (internal):	Estel Cardellach	ROM SAF Local Manager	21/4/2016	
Approved by:	Kent B. Lauritsen	ROM SAF Project Manager	10/5/2016	

DOCUMENT CHANGE RECORD

<i>Issue/Revision</i>	<i>Date</i>	<i>By</i>	<i>Description</i>
Draft 1	28/03/2016	MG	First draft
Draft 2	10/05/2016	MG	Updated after comments by E. Cardellach and K B. Lauritsen
1.0	10/05/2016	MG	First version

VS Author

This VS study was carried out by Dr. Michael Gorbunov, IAP, Moscow, Russia; Email: m_e_gorbunov@mail.ru

VS Duration

The VS study was performed during December 2015 – March 2016 at the home institute of the candidate and with visits to DMI and IEEC during December 2015.

ROM SAF

The Radio Occultation Meteorology Satellite Application Facility (ROM SAF) is a decentralised processing center under EUMETSAT which is responsible for operational processing of GRAS radio occultation data from the Metop satellites and radio occultation (RO) data from other missions. The ROM SAF delivers bending angle, refractivity, temperature, pressure, and humidity profiles in near-real time and offline for NWP and climate users. The offline profiles are further processed into climate products consisting of gridded monthly zonal means of bending angle, refractivity, temperature, humidity, and geopotential heights together with error descriptions.

The ROM SAF also maintains the Radio Occultation Processing Package (ROPP) which contains software modules that will aid users wishing to process, quality-control and

assimilate radio occultation data from any radio occultation mission into NWP and other models.

The ROM SAF Leading Entity is the Danish Meteorological Institute (DMI), with Cooperating Entities: i) European Centre for Medium-Range Weather Forecasts (ECMWF) in Reading, United Kingdom, ii) Institut D'Estudis Espacials de Catalunya (IEEC) in Barcelona, Spain, and iii) Met Office in Exeter, United Kingdom. To get access to our products or to read more about the ROM SAF please go to: <http://www.romsaf.org>

Intellectual Property Rights

All intellectual property rights of the ROM SAF products belong to EUMETSAT. The use of these products is granted to every interested user, free of charge. If you wish to use these products, EUMETSAT's copyright credit must be shown by displaying the words "copyright (year) EUMETSAT" on each of the products used.

List of Contents

EXECUTIVE SUMMARY	5
1. INTRODUCTION	7
1.1 PURPOSE OF DOCUMENT	7
1.2 BACKGROUND	7
2. CT2 ALGORITHM OF THE BENDING ANGLE RETRIEVAL.....	8
2.1 LIST OF VARIABLES	8
2.2 GEOMETRIC OPTICAL PROCESSING	10
2.2.1 <i>Vacuum Model</i>	10
2.2.2 <i>Smooth phase excess model</i>	10
2.3 WAVE OPTICAL PROCESSING.....	11
2.3.1 <i>Fourier Integral Operator</i>	11
2.3.2 <i>Radio Holographic Filter</i>	11
2.3.3 <i>Shadow Border Determination</i>	12
2.3.4 <i>Phase Filtering and Differentiation</i>	13
2.3.5 <i>Radio Holographic Analysis</i>	13
2.3.6 <i>Determination of Bending Angles and CT Amplitude</i>	14
3. PRELIMINARY CONSIDERATIONS AND EXAMPLES ON REFLECTED SIGNALS.....	15
3.1 REFLECTED RAYS RETRIEVAL IN IMPACT PARAMETER DOMAIN.....	16
3.2 REFLECTED RAYS RETRIEVAL IN TIME DOMAIN.....	16
3.3 REFLECTED RAYS RETRIEVAL FROM WIGNER FUNCTION.....	16
3.4 REFLECTED RAYS RETRIEVAL IN MODIFIED IMPACT PARAMETER SPACE	17
3.5 EXAMPLES OF REFLECTIONS IN COSMIC OBSERVATIONS	17
3.6 EXAMPLES OF REFLECTIONS IN SIMULATED DATA.....	32
3.7 DISCUSSION	43
4. REFLECTION RETRIEVAL IMPLEMENTATION	44
4.1 PHASE MODEL FOR REFLECTED RO SIGNALS	44
4.2 RADIO HOLOGRAPHIC INDEX OF REFLECTIONS	46
4.3 FILTERING IN IMPACT PARAMETER SPACE	48
4.4 REFLECTED BENDING ANGLE RETRIEVAL IN TIME DOMAIN	48
5. EXAMPLES OF PROCESSING COSMIC DATA	51
6. EXAMPLES OF PROCESSING METOP DATA	71
7. COMPARISON WITH THE ROM SAF DATABASE	85
8. CONCLUSIONS	99
8.1 ACKNOWLEDGMENTS	99
9. REFERENCES	100
10. LIST OF ACRONYMS	102

Executive Summary

The objectives of the VS project are:

- O1. To implement Wave Optics-based algorithms to extract the reflected BA profiles.
- O2. To propose and check a methodology to identify reflected signals in RO data, based on some descriptors of the expected reflected BA branch.

The tasks to be done by the VS are:

T1. Calculate the impact parameter corresponding to the border between the direct and reflected rays

The reflection border corresponds to the shadow border as it is evaluated in the current version of OCC. Its height is evaluated as the correlation maximum of the CT amplitude with the θ -function. This ray height is the border between the direct and reflected rays, because the amplitude of reflected rays is much lower than that of direct rays.

T2. Calculate two BA's: BA: the usual one; BA-R: the reflected part

The OCC code is modified in such a way that the CT algorithm is applied twice: for direct rays above the shadow border and for reflected ones below the border.

T3. Estimate (and flag) if there is a reflection, based on calculating a specific RMS value of the BA spread

Currently, the OCC and ROPP packages evaluate the BA spread by means of radio holographic analysis in sliding windows. This technique is also applied to reflected BA profiles, after tuning some specific parameters. Implementation of this task required an analysis of RO data with reflections to tune up the specific threshold of the BA spread corresponding to the presence of reflection. The ROM SAF provided data set, VFR list, which was used for this purpose.

T4. Results from some tests with COSMIC and Metop data

OCC package after processing a RO event optionally writes a file containing information on current options and occultation parameters. As part of this activity the updated code writes out some reflected BA characteristics that allow for the automation of extracting RO events with reflections from large data arrays. COSMIC and Metop data were processed and statistical characteristics of the reflections were evaluated by means of a comparison with the list of visually inspected cases (VFR) provided by the ROM SAF.

T5: Report with a description of the algorithm

Current report summarizes the results of this work, a joint scientific paper is under the preparation for publishing in a peer-reviewed journal.

The resulting OCC code with the above modifications serves as a prototype to be recoded into ROPP code. This will be done by the ROM SAF afterward, and not as part of this activity.

1. Introduction

1.1 Purpose of Document

This document contains the results from the ROM SAF Visiting Scientist activity on the development of wave optics code for the retrieval of bending angle profiles for reflected rays. The document is organized as follows: Chapter 2 describes the current version of the CT2 bending angle retrieval, which was not designed for the retrieval of reflected rays. Chapter 3 contains the preliminary considerations of the problem, its possible solutions, and examples from COSMIC observations and Wave Optical Propagator (WOP) simulations. Chapter 4 describes our implementation of the reflection retrieval and its results. Chapters 5 and 6 contain examples for COSMIC and Metop. Chapter 7 contains comparison with ROM SAF database. In Chapter 8, we offer our conclusions. Chapter 9 contains the references.

1.2 Background

A clear signature of signal reflected by the Earth's surface was revealed as early as the beginning of 21st century, by means of the radio holographic analysis of CHAMP radio occultation (RO) data [1, 2]. Similar patterns were also found in Microlab-1 GPS/MET data [10, 11]. It was pointed out that the utilization of reflected signals can be useful for the enhancement of the retrievals. Reflections are mostly observed above water (ocean) or snow (Antarctica). Another application of reflected signals is linked to the altimetry [3, 4].

Currently, the main means of identification of reflections remains the radio holographic analysis [5, 6, 7, 11] or its advanced version based on the Wigner Distribution Function (WDF) [12, 13]. However, it is known that the techniques based on different approximations for the Fourier Integral Operator are also capable of retrieving the reflected part of the bending angle (BA) profile. These techniques include: Canonical Transform (CT) methods [14, 15], Full Spectrum Inversion (FSI) [8], and Phase Matching (PM) [9].

In this Visiting Scientist activity, we aim at the enhancement of current retrieval algorithms by implementing modules for the retrieval of reflected parts of BA profiles.

2. CT2 algorithm of the bending angle retrieval

The purpose of this Chapter is to describe the current CT2 algorithm of the bending angle (BA) retrieval.

2.1 List of Variables

Fortran variable	Mathematical notation	Explanation
TR	t or t_i	Time (s)
XLEO	$\mathbf{x}_L(t)$	LEO (Rx) coordinates in ECEF frame (km)
XGPS	$\mathbf{x}_G(t)$	GPS (Tx) coordinates in ECEF frame (km)
VLEO	$\mathbf{v}_L(t)$	LEO (Rx) velocity in ECEF frame (km/s)
VGPS	$\mathbf{v}_G(t)$	GPS (Tx) velocity in ECEF frame (km/s)
P	$p(t)$ or p_i	Geometric optical impact parameter (km)
U0	$\mathbf{u}_0(t)$	Tx–Rx unit vector
D0	$d_0(t)$	Vacuum relative Doppler shift (dimensionless)
Gamma	γ	Relativistic factor (usually 1).
C_Light	c	Light velocity in vacuum (km/s)
S0	$S_0(t)$	Vacuum phase path (km)
DS	$\Delta S(t)$	Observed phase excess (m)
DSF	$\overline{\Delta S}(t)$	Smoothed phase excess (m)
DDSF	$\overline{\Delta S}'(t)$	Smoothen phase excess rate (m/s)
DF	$\bar{d}(t)$	Smooth relative Doppler shift (dimensionless)
P0	$\bar{p}(t)$	Smooth impact parameter model (km)
E0	$\bar{\varepsilon}(t)$	Smooth bending angle model (rad)
P_D, PDH	$d\bar{p}(t)/d\bar{d}$	Derivative of impact parameter model over Doppler shift
Y	$Y(t)$	New observational coordinate (dimensionless)

Fortran variable	Mathematical notation	Explanation
FT	$f(t)$ or $f(Y)$	Ancillary function for new coordinate definition
FTI	$f_I(t)$ or $f_I(Y)$	Integral of $f(t)$ over $Y(t)$
SM0	$S_0^{(M)}(t)$	Vacuum phase path with subtracted model (km)
SM, SMH	$S^{(M)}(t)$	Phase path with subtracted model (km)
RE	R_E	Local Earth's curvature radius (km)
A, AH	$A(t)$	Observed amplitude
PH	\tilde{p}	Impact height (km)
UH	$\hat{\Phi}'_2 u(\tilde{p})$	Transformed wave fields
AH	$A'(\tilde{p}), \tilde{A}'(\tilde{p}), A''(\tilde{p})$	Amplitude of transformed wave field
SMH	$\varphi'(\tilde{p}), \tilde{\varphi}'(\tilde{p}), \varphi''(\tilde{p})$	Phase of transformed wave field (rad)
SMF	$\bar{\varphi}'(\tilde{p})$	Smoothed phase of transformed (rad)
DPW	Δp_{RH}	Radio holographic filter width (km)
UR	$u_R(\tilde{p})$	Transformed signal with down-converted frequency
AF	$A_{\text{corr}}(\tilde{p}')$	Correlation of $A''(\tilde{p})$ with $\theta_{\tilde{p}'}$
ZH(IFB)	\tilde{p}_{shd}	The shadow border (km)
ECSS	$\delta\varepsilon$	Estimate of refraction angle covariance (rad)
DH	$d(\tilde{p})$	Relative Doppler frequency shift as a function of impact height
EH	$\varepsilon(\tilde{p})$	Bending angle as function impact height (rad)
PH	$p(\tilde{p})$	Accurate impact parameter as function of impact height (km)
APY	$a(\tilde{p})$	Amplitude function of FIO
AH	$A_{CT}(p)$	CT amplitude

2.2 Geometric Optical Processing

Geometric optical (GO) processing is the first stage of the RO data processing. It serves for the initial evaluation of the occultation parameters and smooth models of the Doppler frequency shift and phase excess.

2.2.1 Vacuum Model

The vacuum relative Doppler frequency shift is evaluated as follows:

$$d_0(t) = \frac{c - \mathbf{v}_G(t) \cdot \mathbf{u}_0(t)}{c - \mathbf{v}_L(t) \cdot \mathbf{u}_0(t)} \gamma - 1, \quad (1)$$

where γ is the relativistic factor. Usually, it is a very good approximation to set $\gamma \equiv 1$, because relativistic effects are already taken into account in the pre-processing of telemetric data and phase excess evaluation. The vacuum phase path is evaluated by the integration of the Doppler relative shift:

$$S_0(t) = -c \int_{t_0}^t d_0(t') dt', \quad (2)$$

where t_0 is the starting moment of time. Although the vacuum phase path should just be equal to the satellite-to-satellite distance, it is numerically advantageous to evaluate it by integrating the vacuum Doppler model.

2.2.2 Smooth phase excess model

The smoothed phase excess $\overline{\Delta S}(t)$ and its derivative $\overline{\Delta S}'(t)$ are obtained by the filtering of the measured phase excess $\Delta S(t)$. The smoothed relative Doppler shift $\overline{d}(t)$ is obtained as follows:

$$\overline{d}(t) = d_0(t) - \frac{\overline{\Delta S}'(t)}{c}. \quad (3)$$

From $\overline{d}(t)$ and satellite orbit data we evaluate the smooth impact parameter model $\overline{p}(t)$, bending angle model $\overline{\varepsilon}(t)$, and the derivative of impact parameter over Doppler shift $d\overline{p}(t)/d\overline{d}$. The ancillary function $f(t)$ is evaluated as follows [15]:

$$f(t) = \overline{p}(t) - \overline{d}(t) \frac{d\overline{p}(t)}{d\overline{d}}. \quad (4)$$

The new coordinate is determined as follows [15]:

$$Y(t) = Y_0 - c \int_{t_0}^t \left(\frac{d\overline{p}(t)}{d\overline{d}} \right)^{-1} dt', \quad (5)$$

where Y_0 is a constant determined in such a way that $Y(t) \geq 0$ for the observation time interval. We evaluate the integral of $f(t)$:

$$f_I(t) = \int_{Y(t_0)}^{Y(t)} f(t') dY(t'). \quad (6)$$

Using this function, we evaluate the vacuum and observed phase path with subtracted model as follows:

$$\begin{aligned} S_0^{(M)}(t) &= S_0(t) - R_E Y(t) + f_I(t), \\ S^{(M)}(t) &= S_0^{(M)}(t) + \Delta S(t), \end{aligned} \quad (7)$$

where R_E is the Earth's local curvature radius. Subtraction of $R_E Y(t)$, a linear function of Y , from the phase corresponds to the reduction of the frequency, which equals the impact parameter, by a constant of R_E . All the functions of time t can also be looked at as functions of the new coordinate Y .

2.3 Wave Optical Processing

Wave optical (WO) is the last stage of the data processing providing the most accurate retrieval algorithms.

2.3.1 Fourier Integral Operator

The measured wave field has the following form:

$$u(t) = A(t) \exp\left(ik(S_0(t) + \Delta S(t))\right). \quad (8)$$

The Fourier Integral Operator is defined as follows [15]:

$$\hat{\Phi}_2 u(\tilde{p}) = \sqrt{\frac{k}{2\pi}} \int A(Y) \exp\left(ikS^{(M)}(Y) - ik\tilde{p}Y\right) dY, \quad (9)$$

where the resulting function still needs to be multiplied with the amplitude function, which will be defined below. The variable \tilde{p} is the impact height (impact parameter with subtracted R_E due to the definition of $S_0^{(M)}(t)$ (7)). The transformed field $\hat{\Phi}_2 u(\tilde{p})$ is represented as follows:

$$\hat{\Phi}_2 u(\tilde{p}) = A'(\tilde{p}) \exp(i\varphi'(\tilde{p})), \quad (10)$$

where $A'(\tilde{p})$ is the amplitude of the transformed field with the missing factor of the aforementioned amplitude function, and $\varphi'(\tilde{p})$ is its accumulated phase. The frequency variable Y is defined in (5) in such a way that it is always positive in the area, where any rays may be expected. This simplifies the evaluation of the accumulated phase $\varphi'(\tilde{p})$. The amplitude function is evaluated using $\varphi'(\tilde{p})$, which is the reason why field $u(\tilde{p})$ is first evaluated up to this factor.

2.3.2 Radio Holographic Filter

The radio holographic filter is intended for noise reduction [16,17]. The filter width in the current version is hardcoded and equals $\Delta p_{RH} = 0.25$ km. Using this filter width, we define the smoothed phase $\bar{\varphi}'(\tilde{p})$ and the signal with the down-converted frequency:

$$u_R(\tilde{p}) = A'(\tilde{p}) \exp\left[i(\varphi'(\tilde{p}) - \bar{\varphi}'(\tilde{p}))\right]. \quad (11)$$

The radio holographic filtering consists in convolving $u_R(\tilde{p})$ with the Gaussian kernel and restoring the phase variation:

$$\begin{aligned}\tilde{u}(\tilde{p}) &= \left\{ u_R(\tilde{p}) * \exp \left[- \left(\frac{\tilde{p}}{\Delta p_{RH}} \right)^2 \right] \right\} \exp(i\tilde{\varphi}'(\tilde{p})) = \\ &= \tilde{A}'(\tilde{p}) \exp(i\tilde{\varphi}'(\tilde{p})).\end{aligned}\quad (12)$$

The filtered amplitude $\tilde{A}'(\tilde{p})$ and $\tilde{\varphi}'(\tilde{p})$ are employed according to the program option – cff (complex field filtering). If option –cff=p is specified, where p stays for the impact parameter domain, both filtered amplitude and phase are used in further processing. If, however, option –cff=pa is specified (impact parameter domain, amplitude only), then it is amplitude only that is used in the further processing. Otherwise, no radio holographic is performed:

$$\begin{cases} A''(\tilde{p}) = \tilde{A}'(\tilde{p}), & \varphi''(\tilde{p}) = \tilde{\varphi}'(\tilde{p}), & \text{–cff=p,} \\ A''(\tilde{p}) = \tilde{A}'(\tilde{p}), & \varphi''(\tilde{p}) = \varphi'(\tilde{p}), & \text{–cff=pa,} \\ A''(\tilde{p}) = A'(\tilde{p}), & \varphi''(\tilde{p}) = \varphi'(\tilde{p}), & \text{otherwise.} \end{cases}\quad (13)$$

2.3.3 Shadow Border Determination

First, we evaluate the light zone amplitude A_{lgt} and the shadow zone amplitude A_{shd} as follows:

$$\begin{aligned}A_{lgt} &= \left(\frac{1}{\Delta \tilde{p}_{lgt}} \int_{p_{\max} - \Delta \tilde{p}_{lgt}}^{p_{\max}} (A''(\tilde{p}))^2 d\tilde{p} \right)^{1/2}, \\ A_{shd} &= \left(\frac{1}{\Delta \tilde{p}_{shd}} \int_{p_{\min} - \Delta \tilde{p}_{shd}}^{p_{\min}} (A''(\tilde{p}))^2 d\tilde{p} \right)^{1/2},\end{aligned}\quad (14)$$

where p_{\max} is the maximum impact height estimate, $p_{\min} = 1.7$ km is the upper estimate of the minimum ray height, $\Delta \tilde{p}_{lgt} = 5$ km, $\Delta \tilde{p}_{shd} = 1$ km. For p_{\max} we use the following estimate:

$$p_{\max} = \min(H_B, \max(p_i)),\quad (15)$$

where H_B is the maximum height for the wave optical processing (25 km by default, can be defined by the option –hb), and p_i is the impact parameter array obtained in geometric optical processing. Scaled amplitude is defined as follows:

$$A_{scl}(\tilde{p}) = \min \left(\frac{A_{lgt} + A_{shd}}{2}, A'(\tilde{p}) - A_{shd} \right).\quad (16)$$

The shadow zone border is estimated from the maximum of the correlation between $A_{scl}(\tilde{p})$ and $\theta_{\tilde{p}'}(-\tilde{p}) = \theta(\tilde{p}' - \tilde{p})$ considered as function of \tilde{p}' . To this end, the following function is evaluated:

$$\begin{aligned}
 A_{\text{corr}}(\tilde{p}') &= \|A_{\text{scl}}\| \frac{(A_{\text{scl}}, \theta_{\tilde{p}'})}{\|A_{\text{scl}}\| \|\theta_{\tilde{p}'}\|} = \frac{(A_{\text{scl}}, \theta_{\tilde{p}'})}{\|\theta_{\tilde{p}'}\|} \\
 &= \frac{\int A_{\text{scl}}, \theta_{\tilde{p}'} d\tilde{p}}{(\int \theta_{\tilde{p}'}^2 d\tilde{p})^{1/2}} = \frac{1}{\sqrt{p_{\text{max}} - \tilde{p}'}} \int_{\tilde{p}'}^{p_{\text{max}}} A_{\text{scl}}(\tilde{p}) d\tilde{p},
 \end{aligned} \tag{17}$$

where we multiplied the correlation function with the constant factor of $\|A_{\text{scl}}\|$, which does not influence its maximum. The location \tilde{p}_E of the maximum of this function provides the estimate of the shadow border.

2.3.4 Phase Filtering and Differentiation

The filter width profile is specified by options $-hfw$ (4 reference heights, km), $-fwo$ (phase filter widths at the reference height, km), and $-fwa$ (amplitude filter widths at the reference height, km). Using the filter, we evaluate the filtered phase derivative, separately for $\tilde{p} < \tilde{p}_{\text{shd}}$ and for $\tilde{p} > \tilde{p}_{\text{shd}}$:

$$\frac{d\bar{\varphi}''(\tilde{p})}{d\tilde{p}} \tag{18}$$

2.3.5 Radio Holographic Analysis

We evaluate the phase model by numerically integrating the phase derivative:

$$\bar{\varphi}''(\tilde{p}) = \int_{p_{\text{min}}}^{\tilde{p}} \frac{d\bar{\varphi}''(\tilde{p}')}{d\tilde{p}'} d\tilde{p}'. \tag{19}$$

The signal with the down-converted frequency is evaluated in a way similar to (11)

$$u_R(\tilde{p}) = A''(\tilde{p}) \exp\left[i(\varphi''(\tilde{p}) - \bar{\varphi}''(\tilde{p}))\right]. \tag{20}$$

The value of the sliding aperture has a hardcoded value of $\Delta p_{RH} = 0.5$ km. For each value of impact height \tilde{p} , a sliding Fourier transform is evaluated:

$$\tilde{u}_R(\tilde{p}, Y) = \sqrt{\frac{k}{2\pi}} \int_{\tilde{p} - \frac{\Delta p_{RH}}{2}}^{\tilde{p} + \frac{\Delta p_{RH}}{2}} u_R(\tilde{p}) \exp(ik\tilde{p}Y) d\tilde{p}. \tag{21}$$

From the sliding spectrum, we evaluate the bending angle spectral width:

$$\delta\varepsilon_{SS}^2(\tilde{p}) = \frac{\int_{-\Delta\varepsilon_M}^{\Delta\varepsilon_M} Y^2 |\tilde{u}_R(\tilde{p}, Y)|^2 dY}{\int_{-\Delta\varepsilon_M}^{\Delta\varepsilon_M} |\tilde{u}_R(\tilde{p}, Y)|^2 dY} \tag{22}$$

The lower-tropospheric bending angle covariance is estimates as follows:

$$\delta\varepsilon^2(\tilde{p}) = \max\left(0, \delta\varepsilon_{SS}^2(\tilde{p}) - \delta\varepsilon_{SS}^2(\tilde{p} = 10 \text{ km})\right). \tag{23}$$

2.3.6 Determination of Bending Angles and CT Amplitude

We evaluate $Y_s(\tilde{p})$:

$$Y_s(\tilde{p}) = -\frac{1}{k} \frac{d\bar{\varphi}''(\tilde{p})}{d\tilde{p}} - \Delta Y, \quad (24)$$

where ΔY is the additional border width of the Y high resolution grid. Because the limits of the grid are $-\Delta Y$ and $Y_{\max} + \Delta Y$, we have to take into account the fact that the lowest value of Y is $-\Delta Y$, rather than 0 as assumed by the Fast Fourier Transform algorithm. We evaluate the dependence $t(Y)$. Then we evaluate the Doppler frequency shift as a function of the impact height:

$$d(\tilde{p}) = \bar{d}(t(Y_s(\tilde{p}))) + \left(\frac{d\bar{p}(t)}{d\bar{d}} \right)^{-1} (R_E + \tilde{p} - \bar{p}(t(Y_s(\tilde{p})))), \quad (25)$$

where the second term corresponds to the linearized deviation of the Doppler frequency shift from its smoothed model.

Using the interpolated orbit data $\mathbf{x}_L(t(Y_s(\tilde{p})))$, $\mathbf{x}_G(t(Y_s(\tilde{p})))$, $\mathbf{v}_L(t(Y_s(\tilde{p})))$,

$\mathbf{v}_G(t(Y_s(\tilde{p})))$, and $d(\tilde{p})$, we evaluate the bending angles $\varepsilon(\tilde{p})$ and impact parameters $p(\tilde{p})$. Because the value of $R_E + \tilde{p}$ is an approximate value of the accurate impact parameter:

$$p(\tilde{p}) \approx R_E + \tilde{p}, \quad (26)$$

these two dependencies allow for a parametric definition of the bending angle profile $\varepsilon(p)$. The dependence of $\varepsilon(p)$ will be mostly single-valued, except maybe some narrow areas. This effect can be corrected for by the monotonization of the array p_i . Due to the mutual relation between \tilde{p} and monotonic p , any function of \tilde{p} can also be used as a function of p .

Now we can evaluate the amplitude function of the FIO [15]:

$$a(p) = \left(\sqrt{|\mathbf{x}_G(t(Y_s(p)))|^2 - p^2} + \sqrt{|\mathbf{x}_L(t(Y_s(p)))|^2 - p^2} \right)^{1/2} \times \left\{ |\mathbf{x}_G(t(Y_s(p)))| |\mathbf{x}_L(t(Y_s(p)))| \sin \theta(t(Y_s(p))) \right\}_{3-D}^{1/2}, \quad (27)$$

where θ is the angle between $\mathbf{x}_G - \mathbf{x}_{LC}$ and $\mathbf{x}_L - \mathbf{x}_{LC}$. The full FIO is defined as follows:

$$\hat{\Phi}_2^{(a)} u(p) = a(p) \hat{\Phi}_2 u(p). \quad (28)$$

The CT amplitude is defined using the amplitude function $a(p)$:

$$A_{CT}(p) = \frac{A''(p)a(p)}{A''_{\text{vac}}}, \quad (29)$$

where A''_{vac} is the normalizing constant, determined in such a way that the “vacuum” value of $A_{CT}(p)$, i.e. its value at large heights, where refractive effects in the amplitude vanish, should be unity.

3. Preliminary Considerations and Examples on Reflected Signals

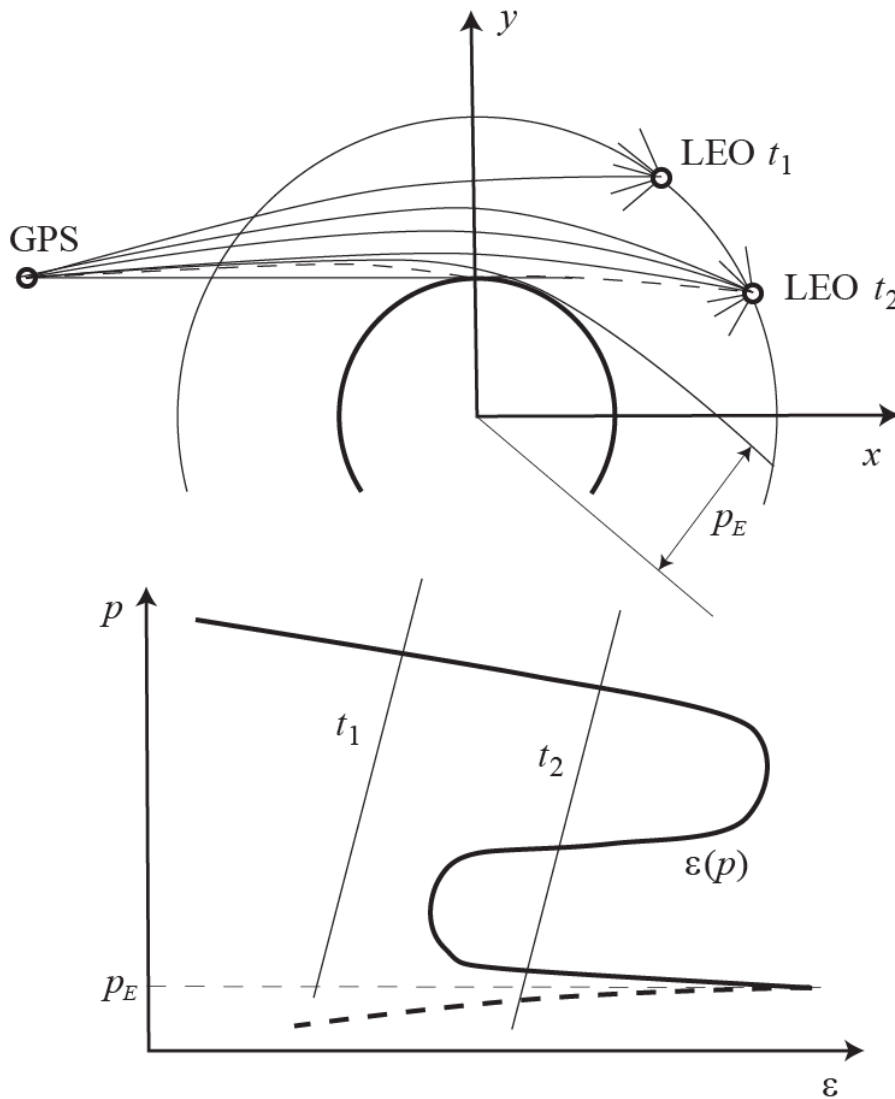


Figure 1. Reflection and multipath propagation geometry.

In Chapter 2, we described the CT2 algorithm of the bending angle retrieval. The current version of the algorithm is designed for the retrieval of bending angles for direct rays. However, there is no principal difference between direct and reflected rays from the view point of the received signal. Reflected rays are characterized by a lower amplitude and by a rapidly increasing bending angle profile. But the same features can also be observed for rays below a wave guide. This allows for the modification of the CT2 algorithm in order to implement also the retrieval of reflected rays. In this Chapter, we will discuss possible ways of this modification. In Sections 3.1 to 3.4, we discuss possible algorithms for the retrieval of reflected rays. In Sections 3.5 and 3.6, we give example of reflections in COSMIC observations and simulations based on ECMWF analyses. In Section 3.7, we present conclusions regarding the optimal retrieval method.

3.1 Reflected Rays Retrieval in Impact Parameter Domain

As we saw, the analysis of the amplitude of the field in the transformed space allows for the determination of the shadow border impact height \tilde{p}_E . Practically, because the energy of reflected rays is much smaller than that of direct rays, this will also be the border between direct and reflected rays. The CT2 algorithm evaluates the filtered phase derivative, separately for $\tilde{p} < \tilde{p}_E$ and for $\tilde{p} > \tilde{p}_E$, which we denote as follows:

$$\frac{d\bar{\varphi}_D''(\tilde{p})}{d\tilde{p}}, \quad \frac{d\bar{\varphi}_R''(\tilde{p})}{d\tilde{p}}, \quad (30)$$

where subscript D stays for direct rays, and subscript R stays for reflected rays. However, it will be necessary to implement an additional option that specifies the filter width for reflected rays. This is explained by the fact that the impact parameter interval for reflected rays is usually as narrow as 100–200 m. This requires a narrow filter window of about 20 m, while the typical setting for processing direct rays in the lowest troposphere is 250 m.

3.2 Reflected Rays Retrieval in Time Domain

The CT2 algorithm is designed for the retrieval of BA profiles in multipath areas, where the profiles are non-monotonic. This is not the case for BA profiles of reflected rays, which always monotonically increase. This makes it convenient to retrieve dependence $p(\varepsilon)$ rather than $\varepsilon(p)$. On the other hand, it is more straightforward to formulate the retrieval algorithm in the time domain, as illustrated by Figure 1. Of course, in the time domain, in presence of reflection, there is always multipath propagation due to the interference of direct and reflected rays. But the field component related to the directed rays can be effectively removed. To this end, we can use the impact parameter domain, where the direct and reflected rays are clearly separated by the border impact height of \tilde{p}_E .

Therefore, we can form the following field $u_R(t)$ in the time domain that only contains the reflections:

$$u_R(t) = \hat{\Phi}_2^{-1} \left[\hat{\Phi}_2 [u(t)] \theta(\tilde{p}_E - \tilde{p}) \right], \quad (31)$$

where $\hat{\Phi}_2$ is the FIO defined by (9) and (27), and $\hat{\Phi}_2^{-1}$ is its inverse. This function can then be processed using the standard geometric optical (GO) technique.

3.3 Reflected Rays Retrieval from Wigner Function

Wigner Distribution Function (WDF) [12,13] can also be used for the retrieval of reflected rays retrieval. WDF is a 2-D pseudo-density $W(\varepsilon, p)$ of energy in the (ε, p) space. The average bending angle as function of impact parameter can be found as follows:

$$\varepsilon(p) = \frac{\int \varepsilon' W(\varepsilon', p) d\varepsilon'}{\int W(\varepsilon', p) d\varepsilon'}. \quad (32)$$

In a similar way, it is possible to obtain dependence $p(\varepsilon)$:

$$p(\varepsilon) = \frac{\int p' W(\varepsilon, p') dp'}{\int W(\varepsilon, p') dp'}, \quad (33)$$

where integration should be performed over the shadow zone in order to retrieve the dependence $p(\varepsilon)$ for reflected rays.

3.4 Reflected Rays Retrieval in Modified Impact Parameter Space

The FIO (9) corresponds to the following linear canonical transform [15]:

$$\begin{aligned} \tilde{p} &= f(Y) + \eta, \\ \xi &= -Y, \end{aligned} \quad (34)$$

where η is the eikonal derivative (momentum) of the original observed field $u(t)$, and ξ is the momentum of the transformed field. This transform can be modified in order to use another coordinate:

$$\tilde{p}' = \tilde{p} + \alpha Y, \quad (35)$$

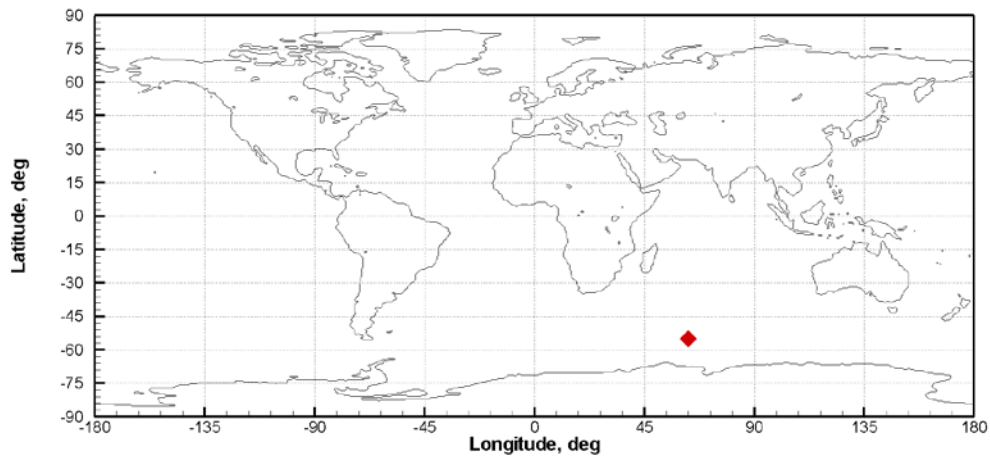
where α is a tunable parameter. The corresponding transform will be written as follows:

$$\begin{aligned} \tilde{p}' &= f(Y) + \alpha Y + \eta \equiv f'(Y) + \eta, \\ \xi &= -Y. \end{aligned} \quad (36)$$

Substituting the modified function $f'(Y)$ into (6), (7), (8), and (9), we obtain the expression for the modified FIO $\hat{\Phi}'_2$. The advantage of this approach is that it can be implemented by a relatively small modification of the existing CT2 algorithm.

3.5 Examples of Reflections in COSMIC observations

Below we give some examples of reflections detected in COSMIC observation (Figure 2 through Figure 15). Each Figure includes the map indicating the event location and the 2-D plot of the WDF for the observed wave field [12] (cf. Figure 1). Reflections are observed over ocean or snow/ice. Many interesting examples are observed over Antarctica.



2008/01/01; 00:07:53.000; 55.22S 62.95E

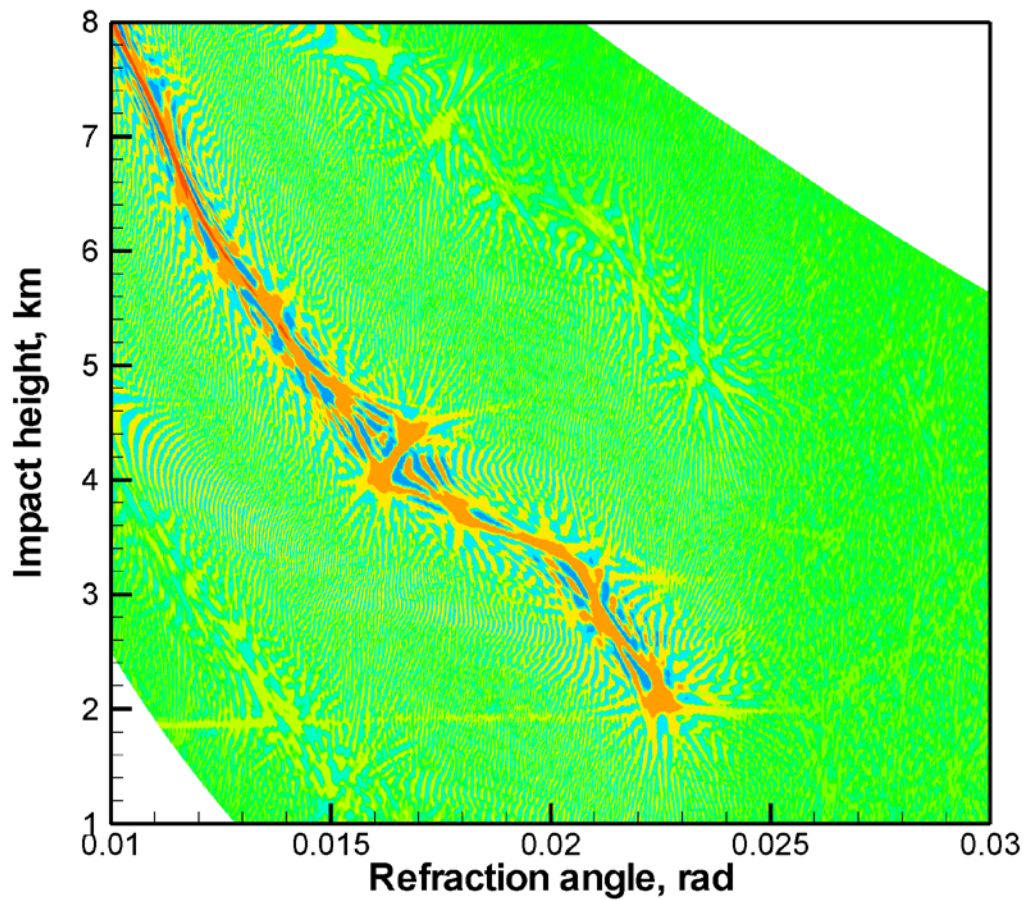
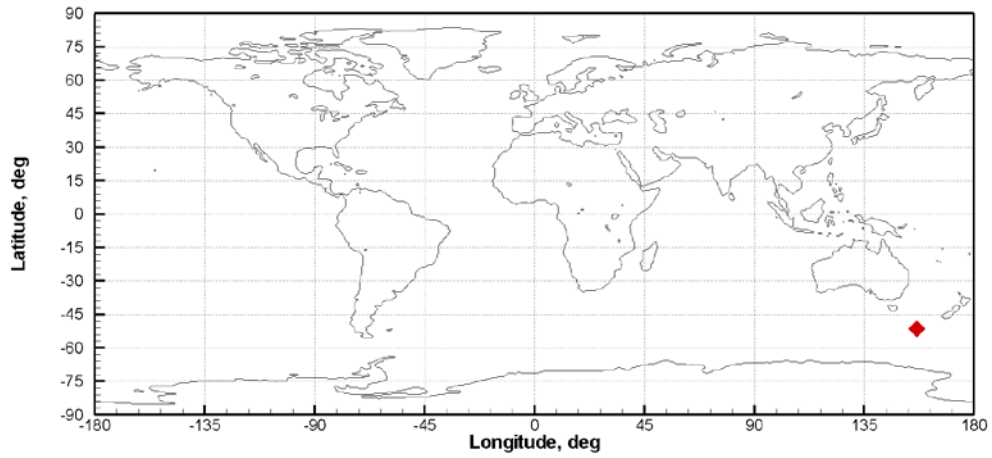


Figure 2. Reflection over ocean.



2008/01/01; 00:22:50.000; 51.48S 156.57E

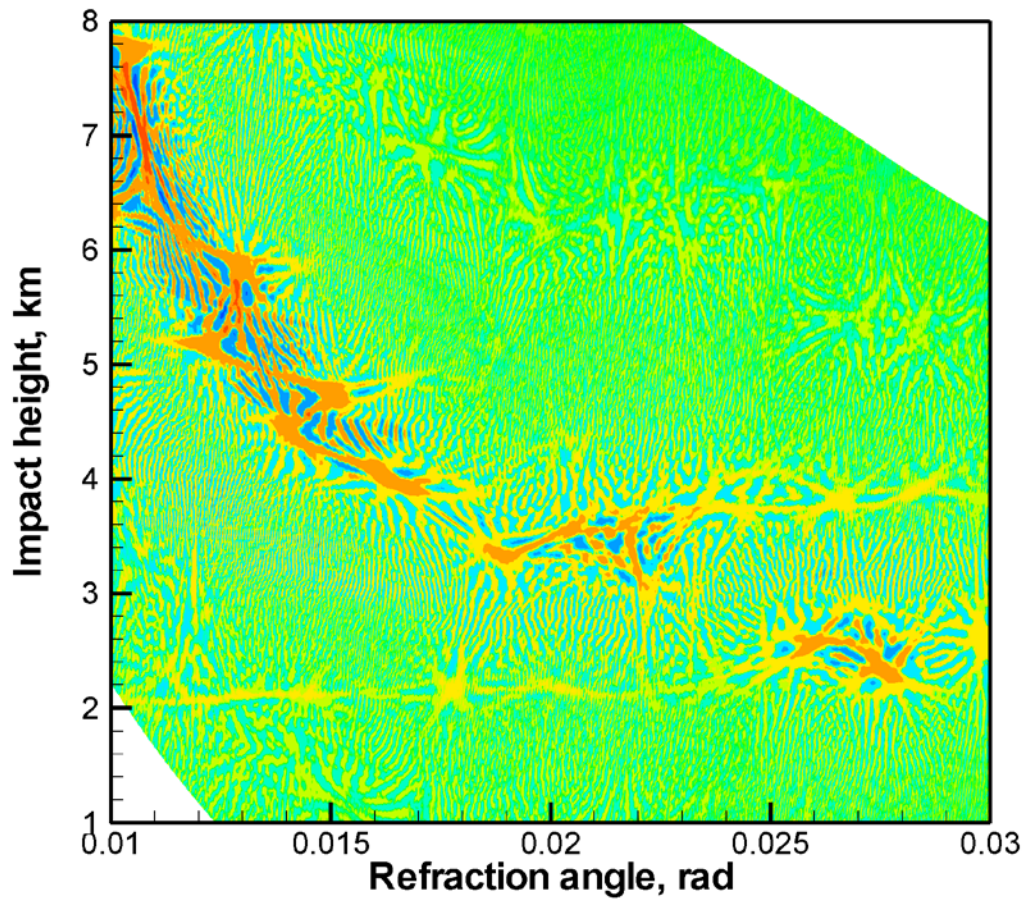
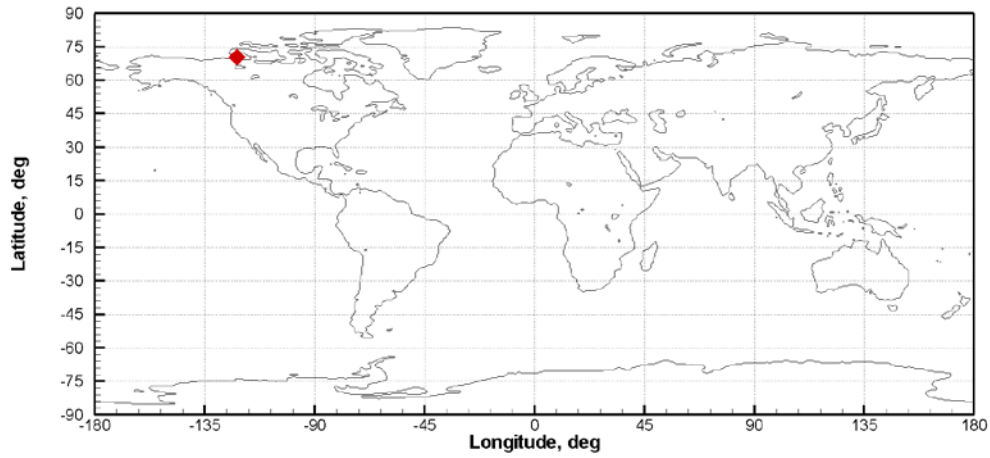


Figure 3. Reflection over ocean.



2008/01/01; 01:02:23.000; 70.28N 121.87W

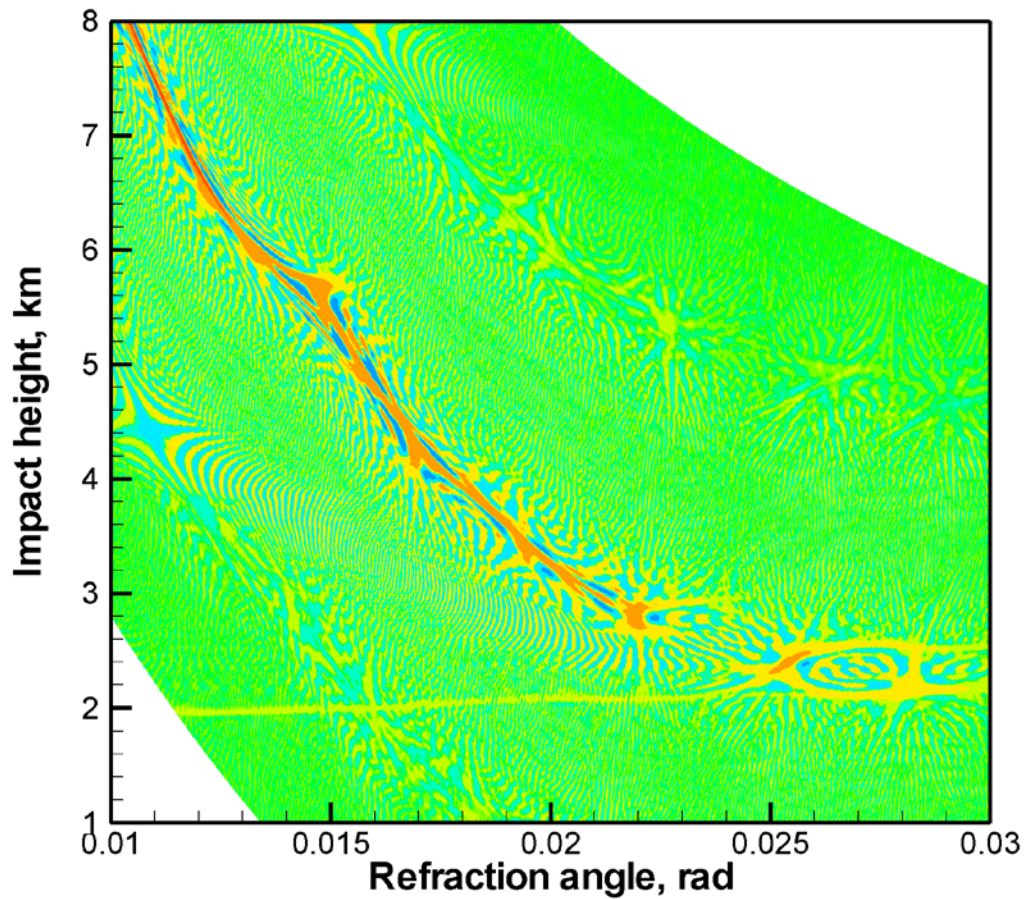
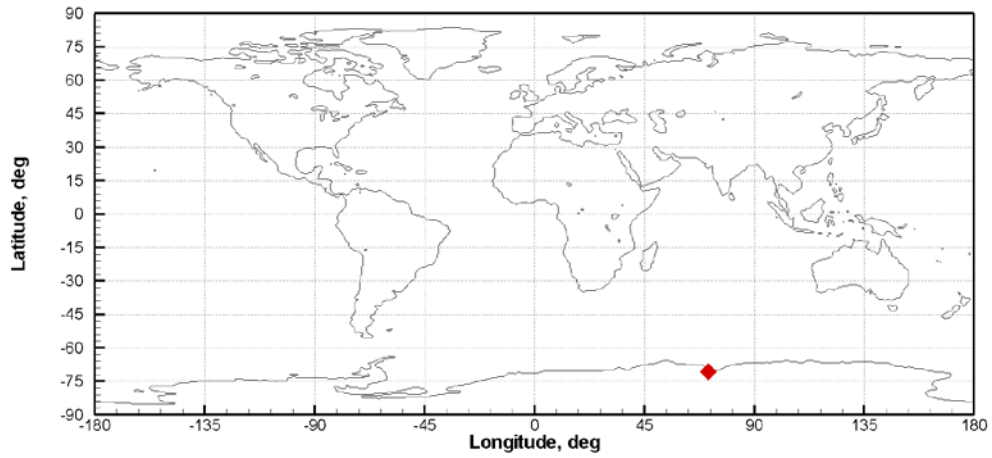


Figure 4. Reflection over ice/snow.



2008/01/01; 01:54:49.000; 70.85S 71.01E

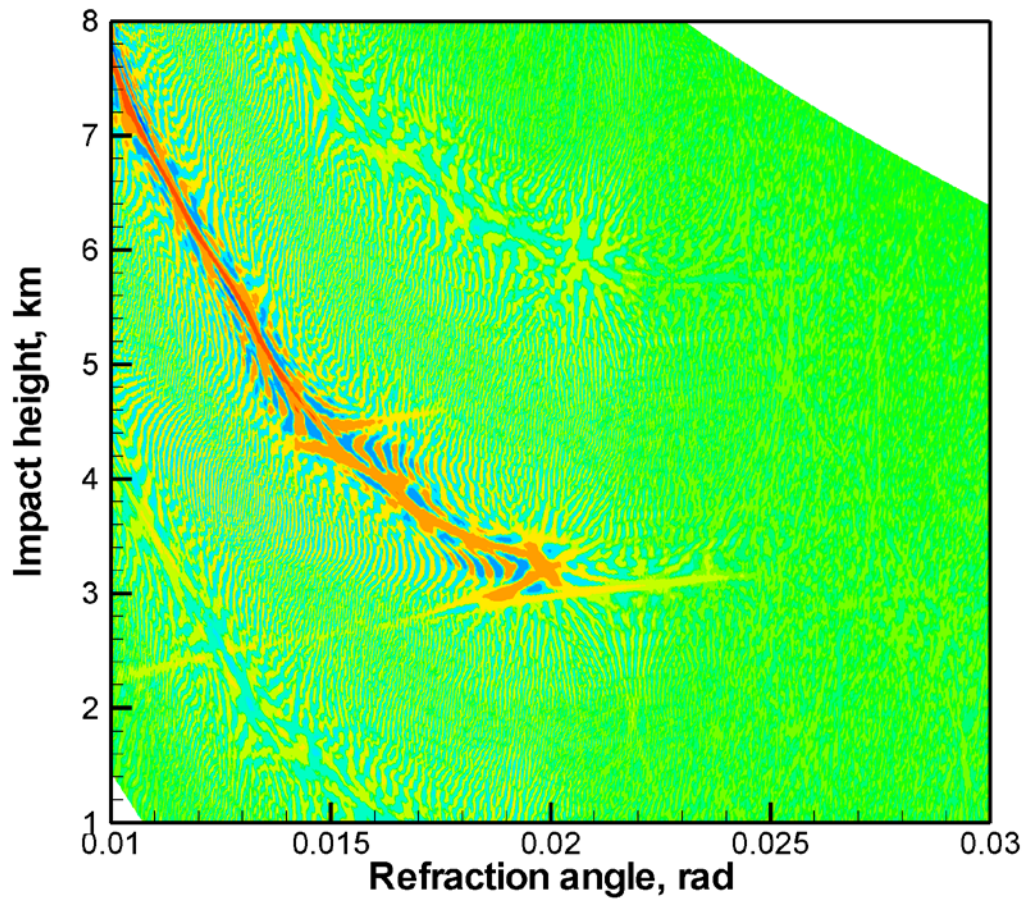
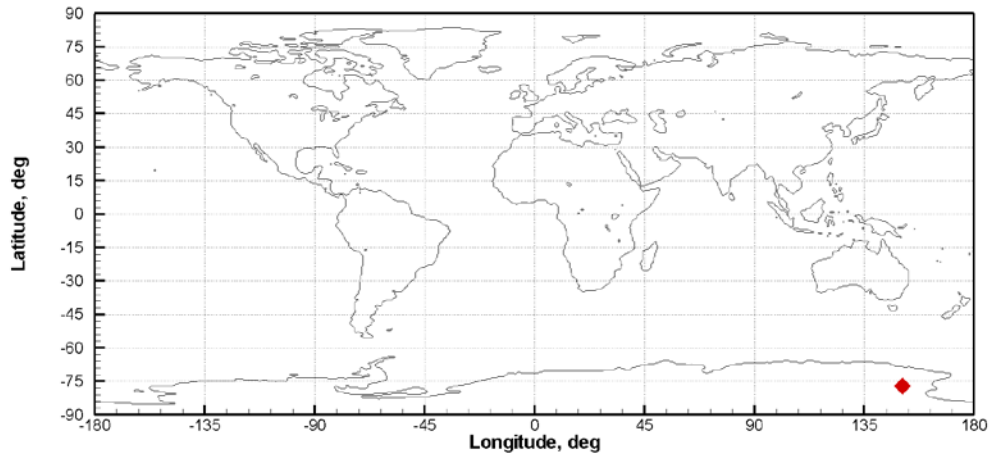


Figure 5. Reflection over ice/snow in Antarctica.



2008/01/01; 01:58:34.000; 77.26S 150.57E

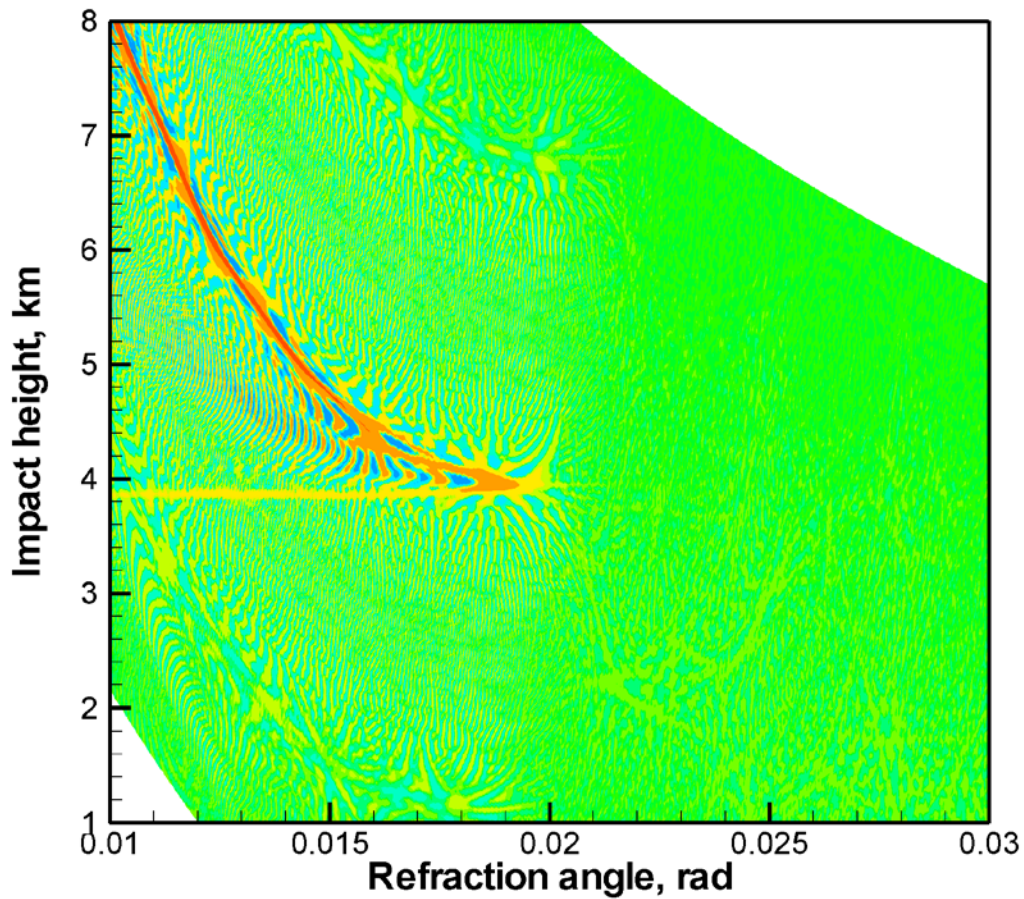
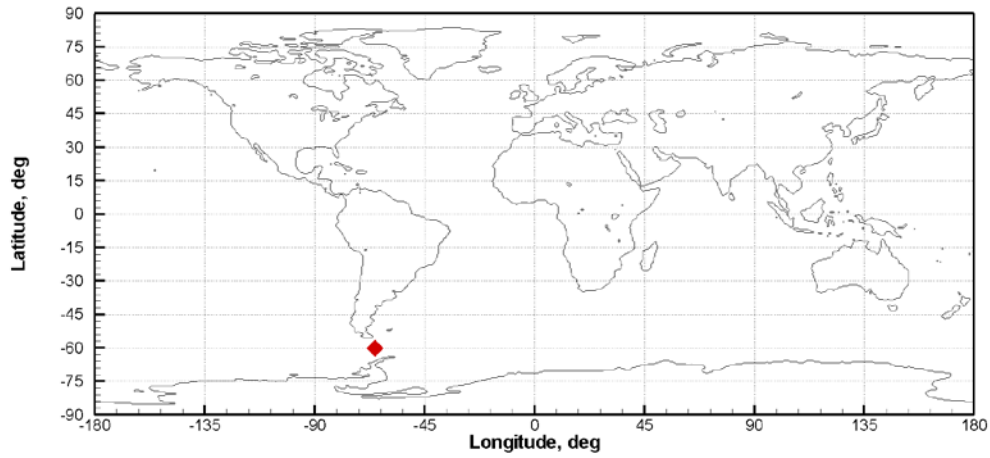


Figure 6. Reflection over ice/snow in Antarctica.



2008/01/01; 01:04:06.000; 60.29S 65.37W

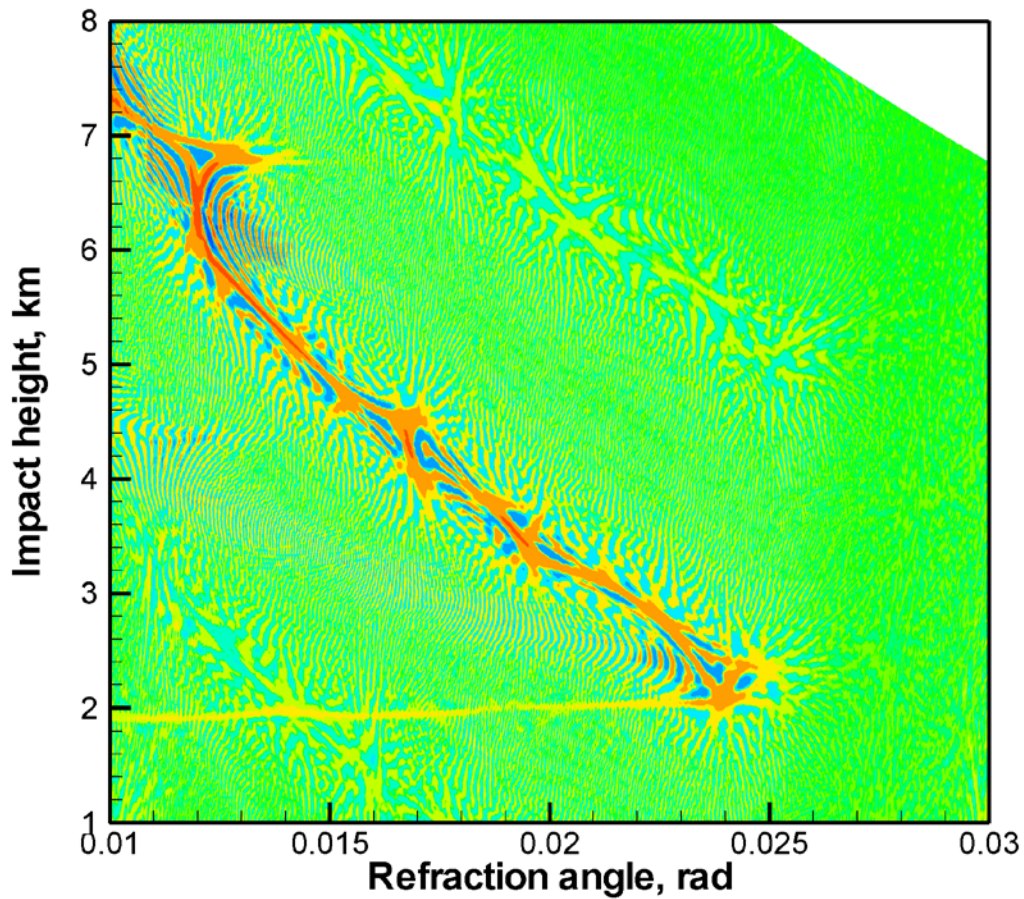
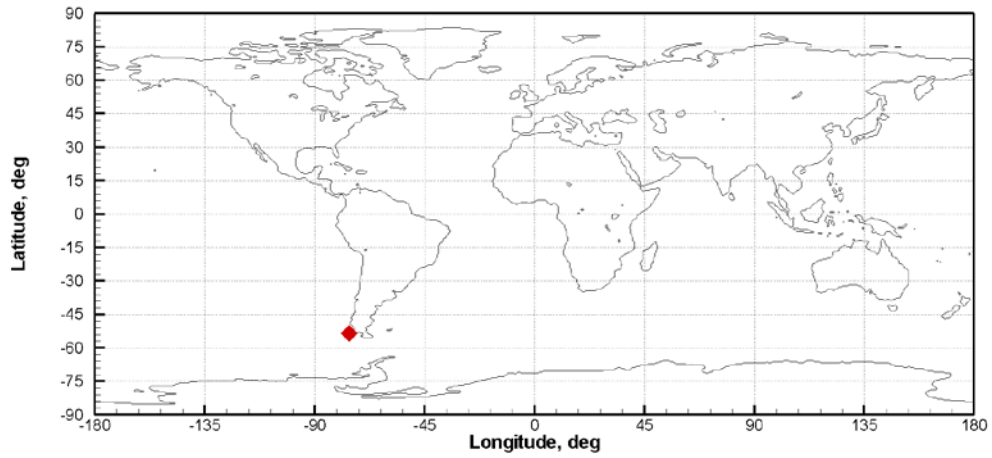


Figure 7. Reflection over ocean.



2008/01/01; 01:06:00.999; 53.61S 75.91W

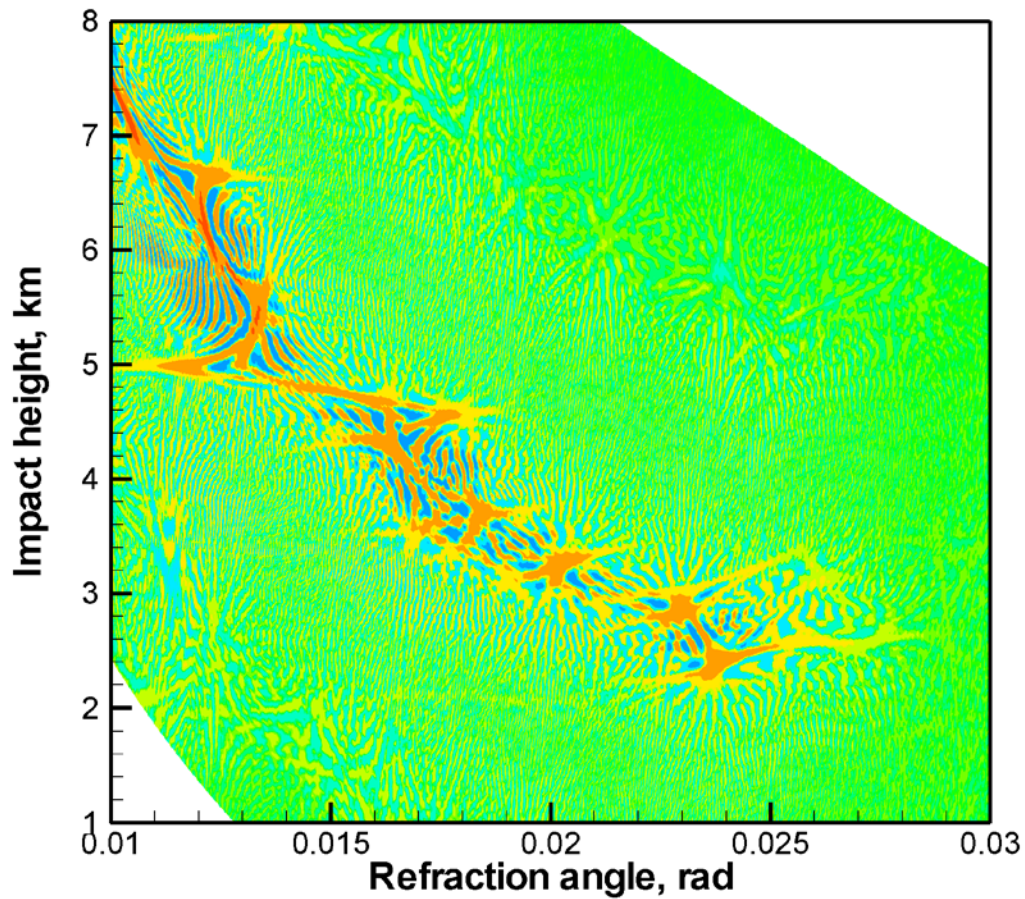
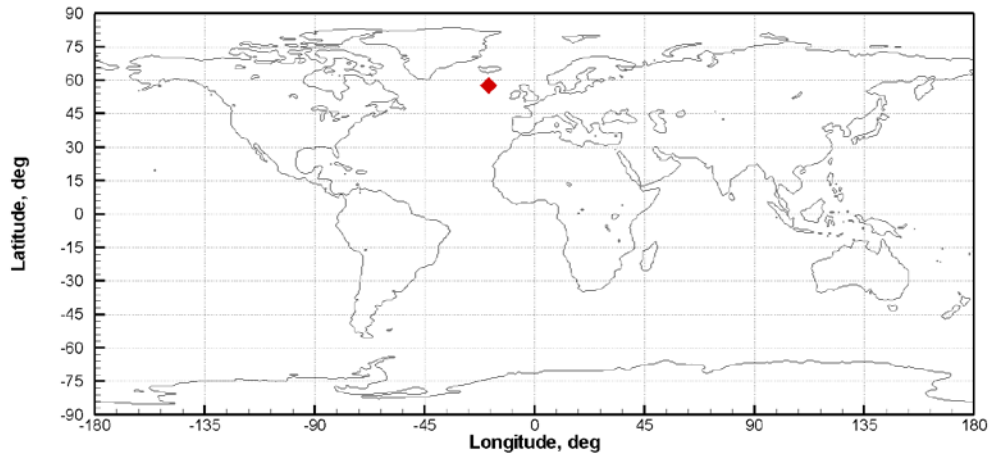


Figure 8. Reflection over ocean.



2008/01/01; 01:24:57.000; 57.77N 18.73W

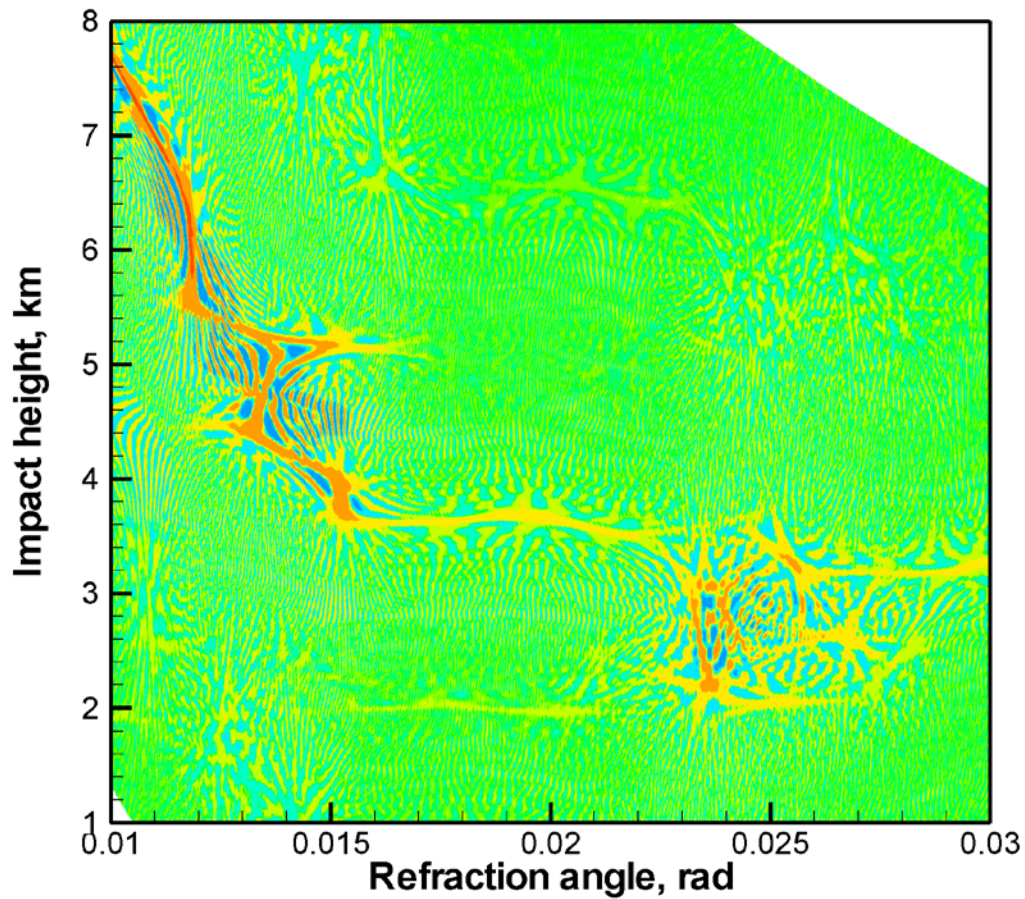
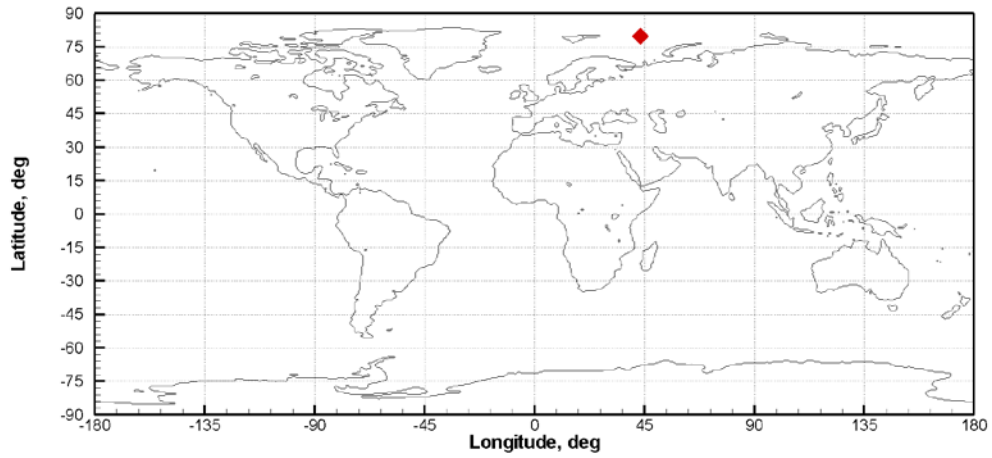


Figure 9. Reflection over ocean.



2008/01/01; 01:47:47.000; 79.89N 43.37E

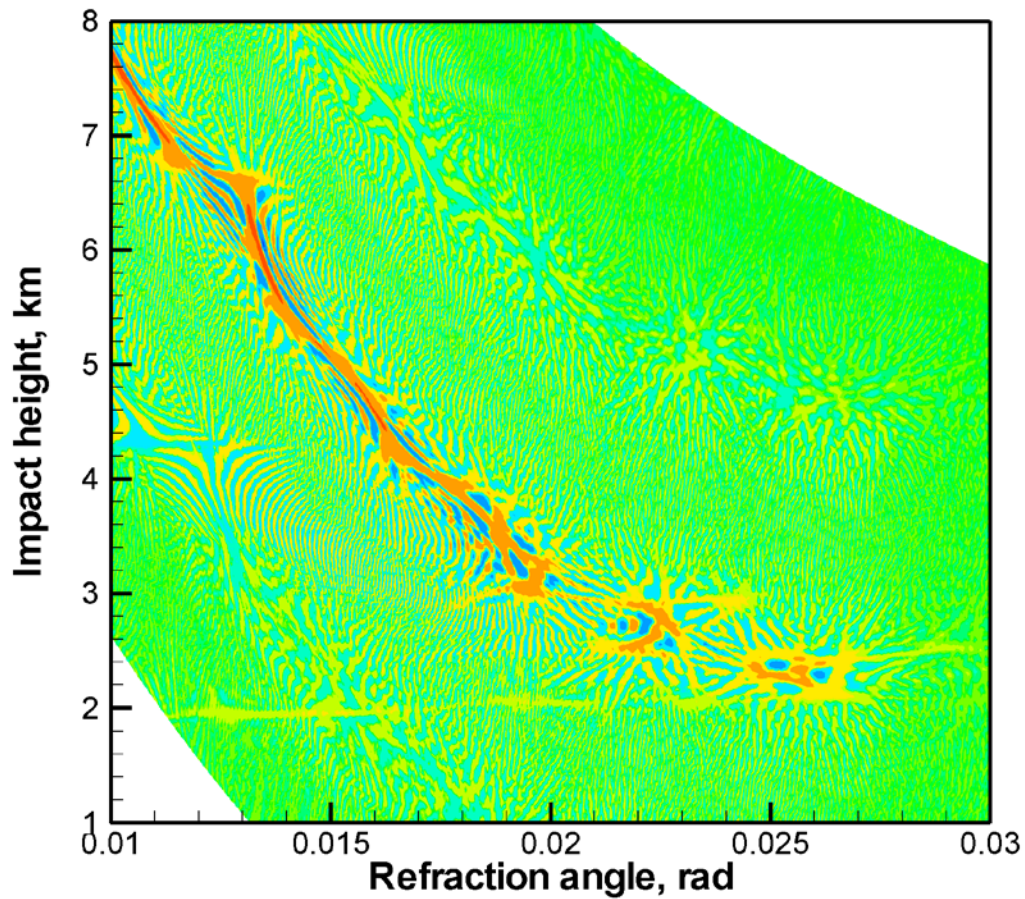
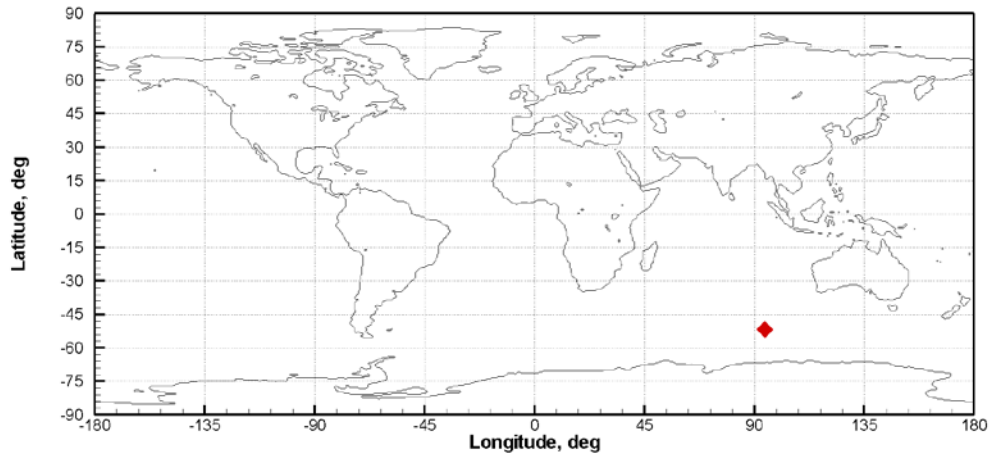


Figure 10. Reflection over ice/snow.



2008/01/01; 01:02:25.000; 51.81S 94.23E

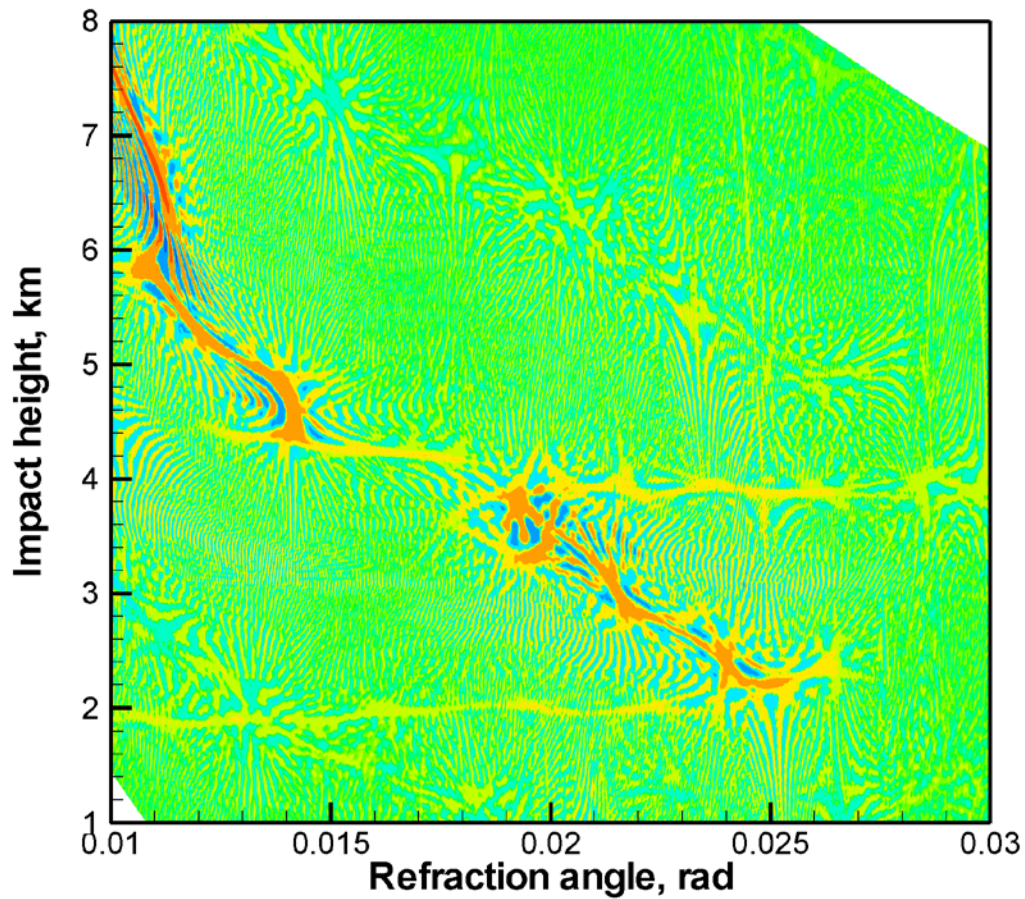
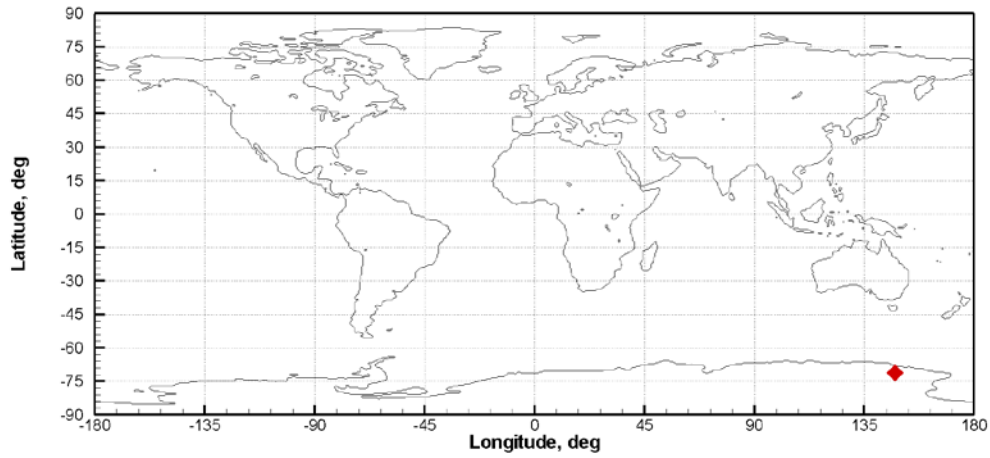


Figure 11. Reflection over ocean.



2008/01/01; 01:10:53.000; 71.27S 147.67E

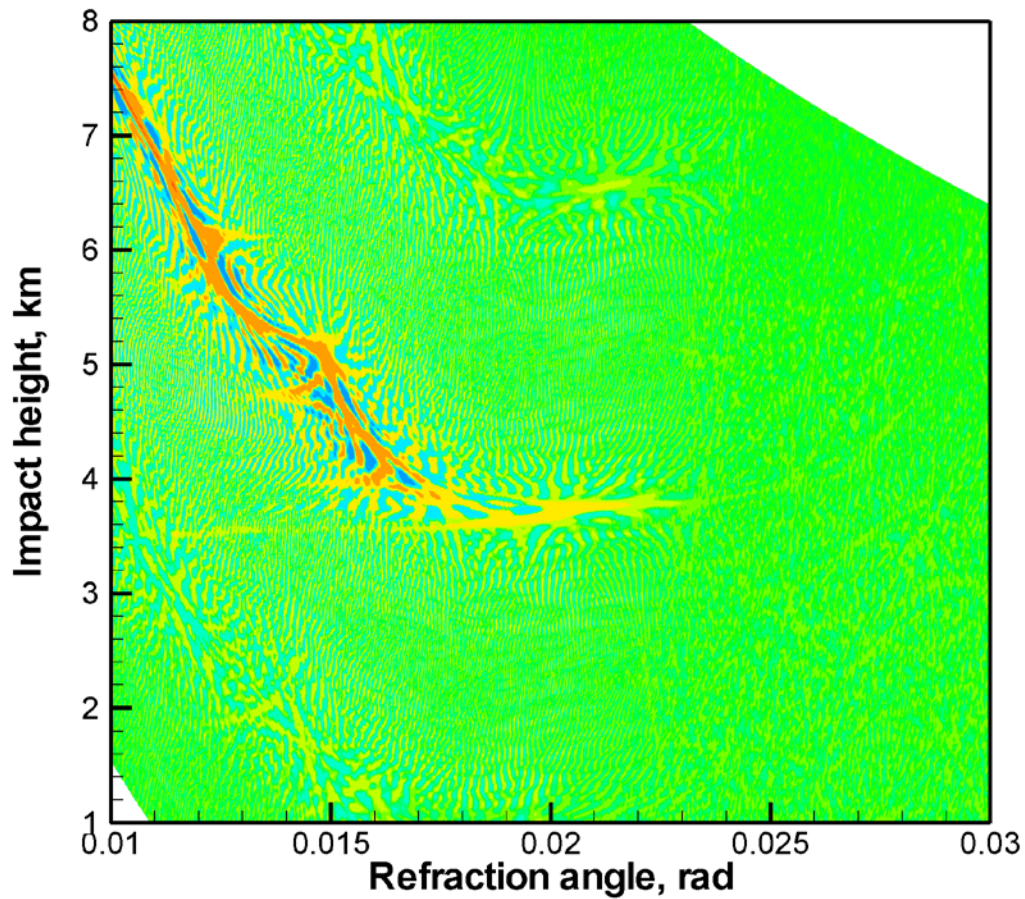
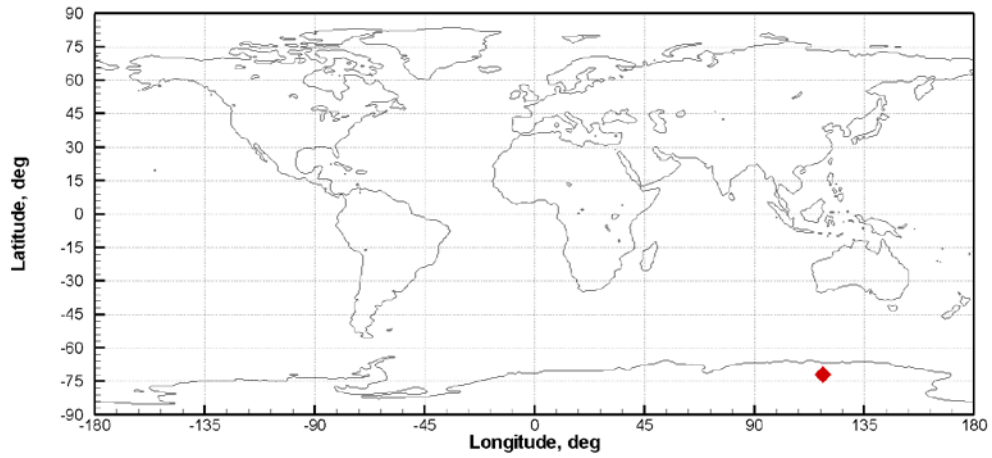


Figure 12. Reflection over Antarctica.



2008/01/01; 01:24:05.000; 71.97S 117.94E

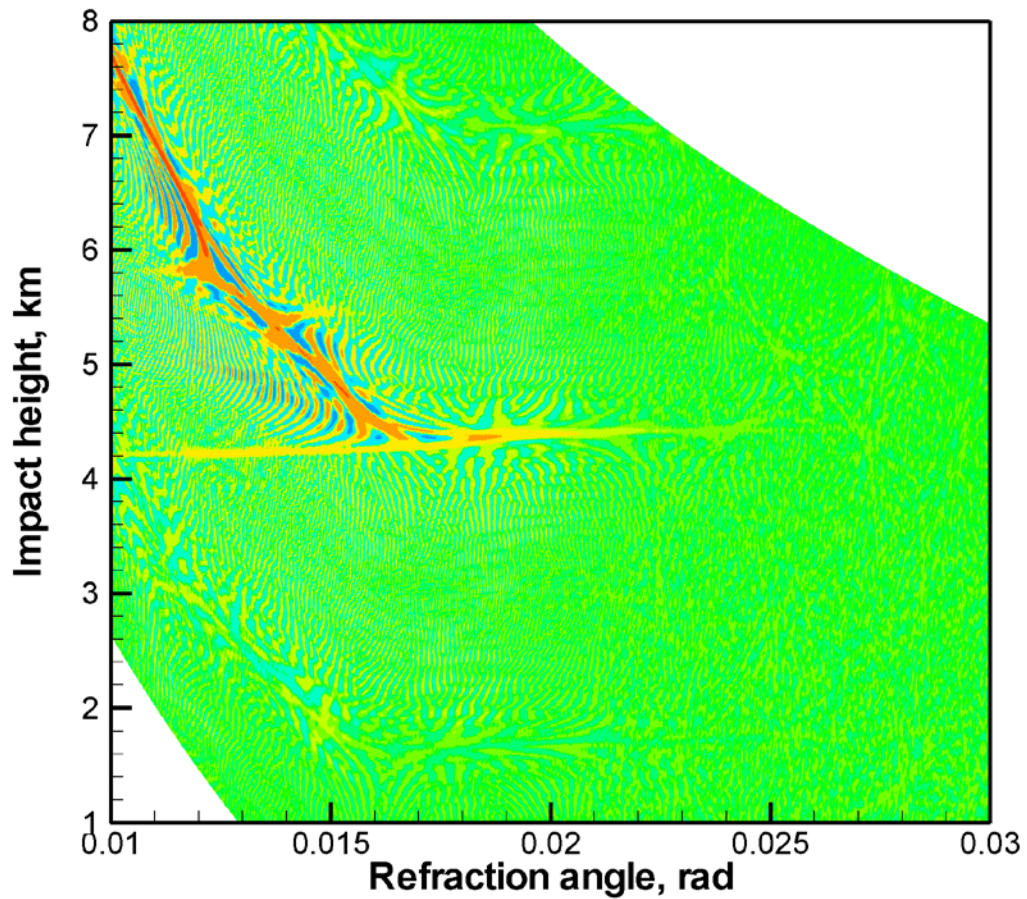
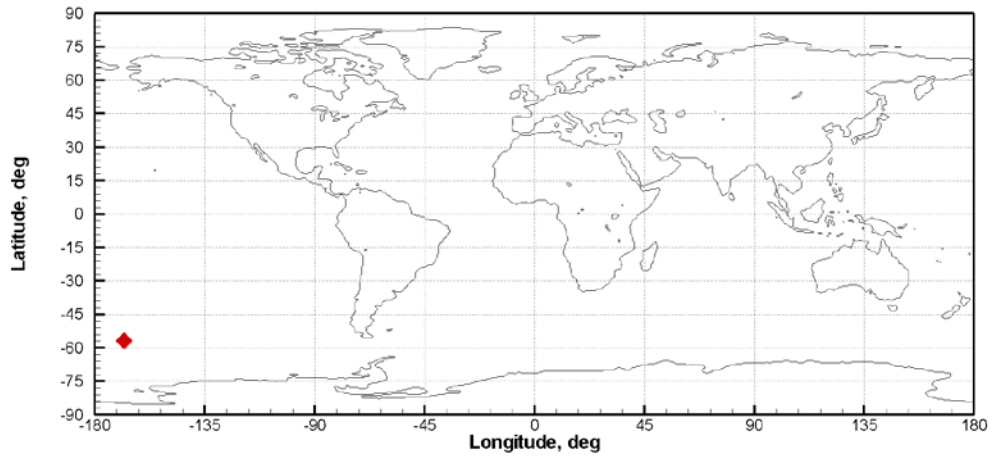


Figure 13. Reflection over Antarctica.



2008/01/01; 01:33:00.000; 56.99S 168.18W

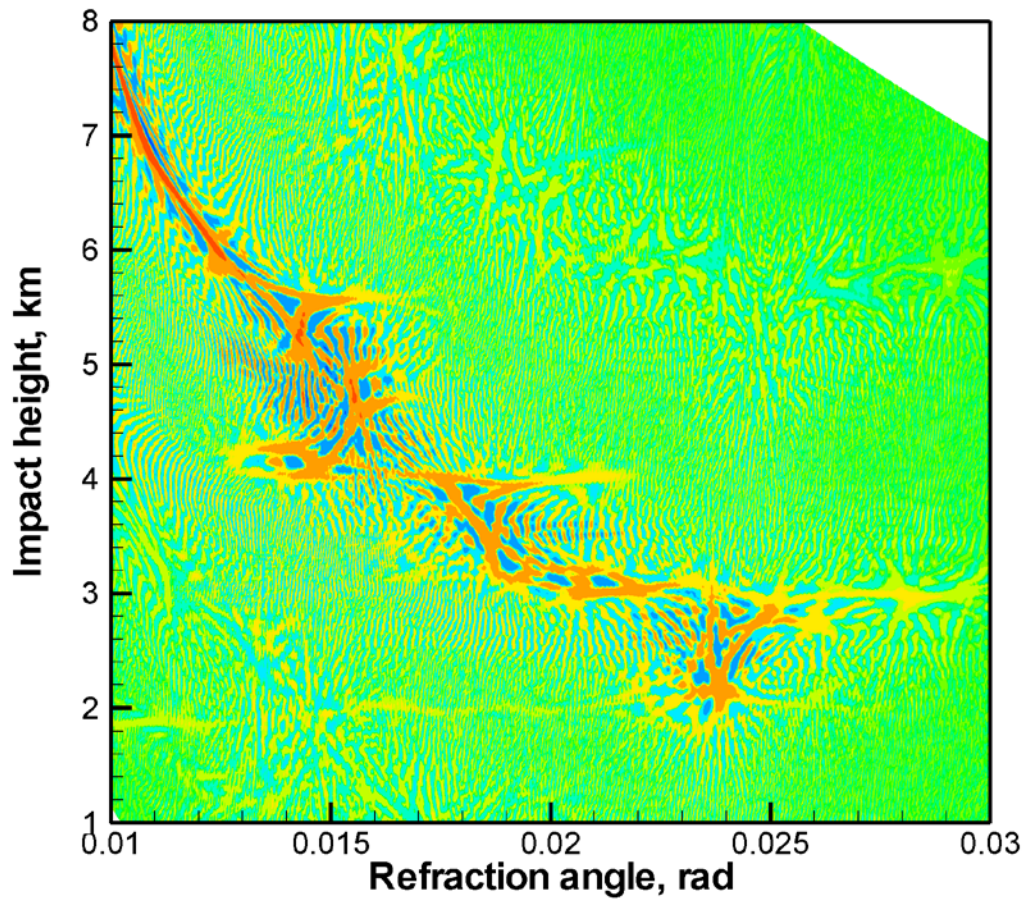
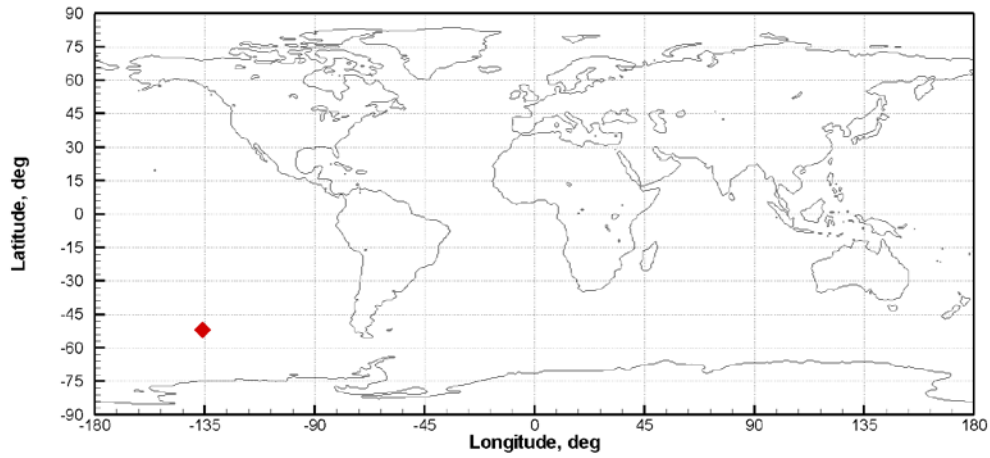


Figure 14. Reflection over ocean.



2008/01/01; 01:37:02.000; 52.12S 135.97W

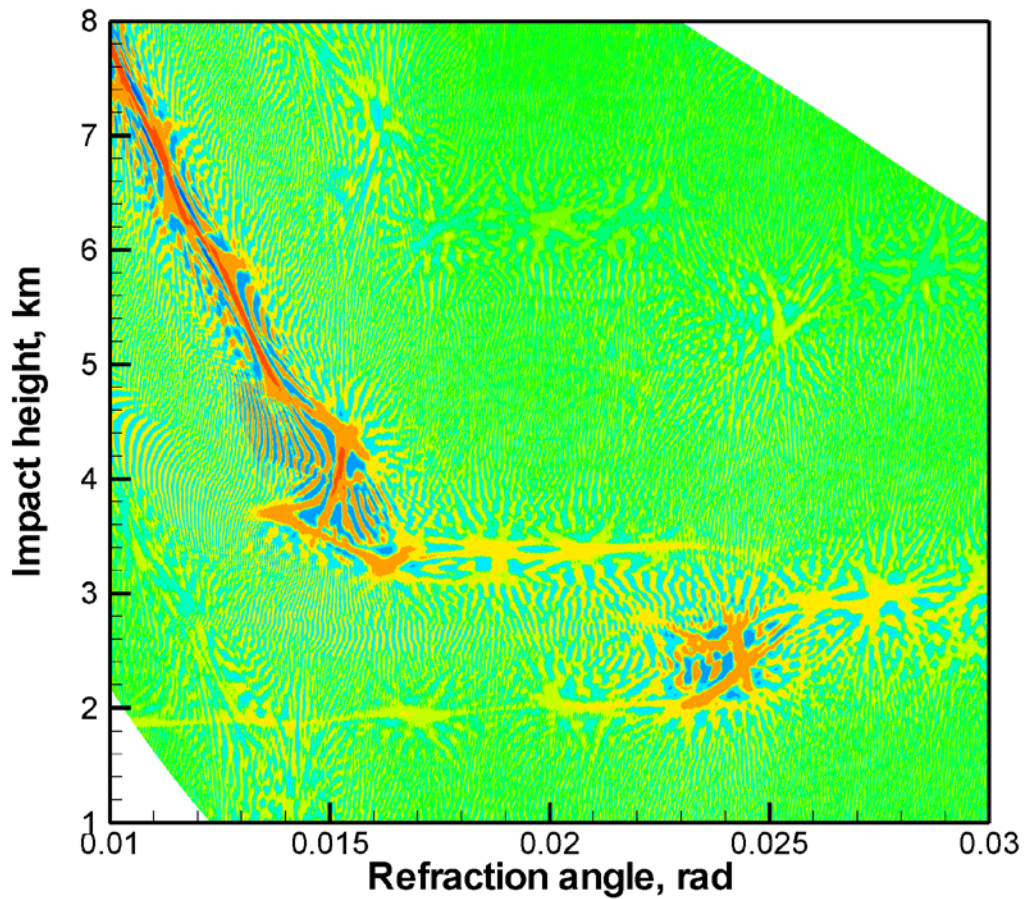
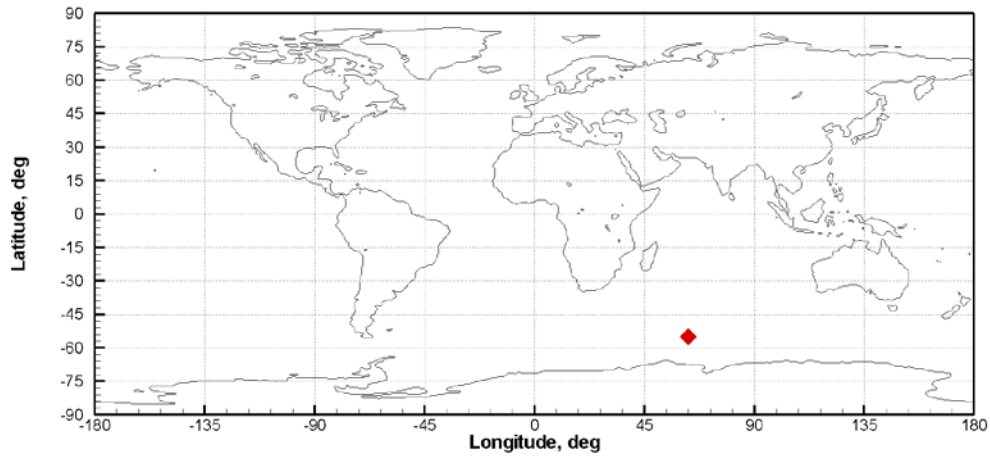


Figure 15. Reflection over ocean.

3.6 Examples of Reflections in Simulated Data

Wave Optical Propagator (WOP) [18] allows for the realistic simulation of RO signals using the split-step method. WOP has also the capability of simulating reflections. This capability utilizes the hard boundary condition in phase screens: the field inside the Earth is set to 0. Setting the field to 0 is equivalent to arranging secondary emitters in antiphase with the incident wave. The secondary emitters will then create the reflected wave obeying the standard reflection law. Because the hard boundary condition as it is currently implemented, is independent from the actual surface properties, WOP can simulate reflections all over the globe, not only above oceans, snow, or ice. Below we show some examples of reflections in simulated data.



2008/01/01; 00:07:53.000; 55.22S 62.95E

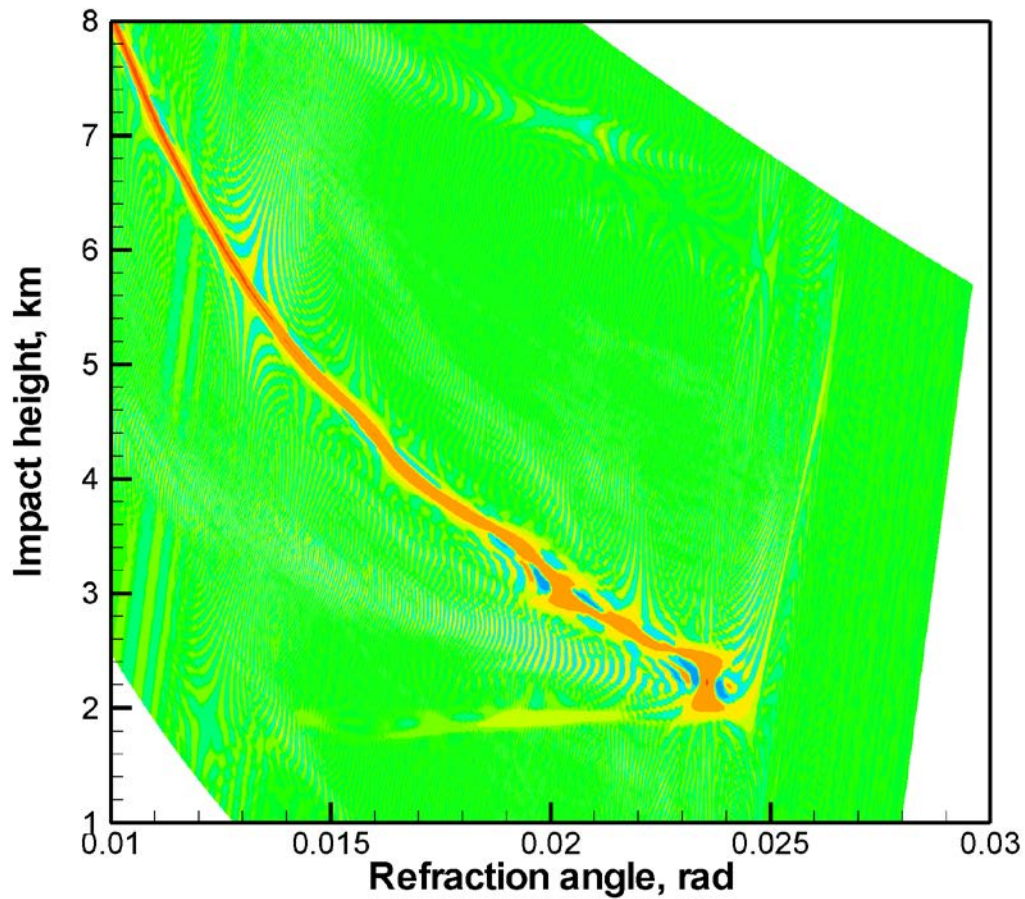
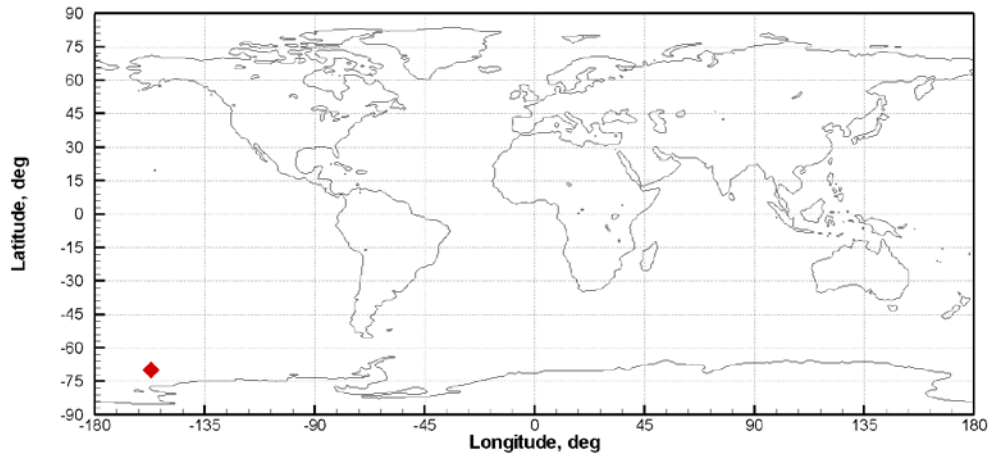


Figure 16. Simulated reflection over ocean.



2008/01/01; 00:18:30.000; 69.98S 156.96W

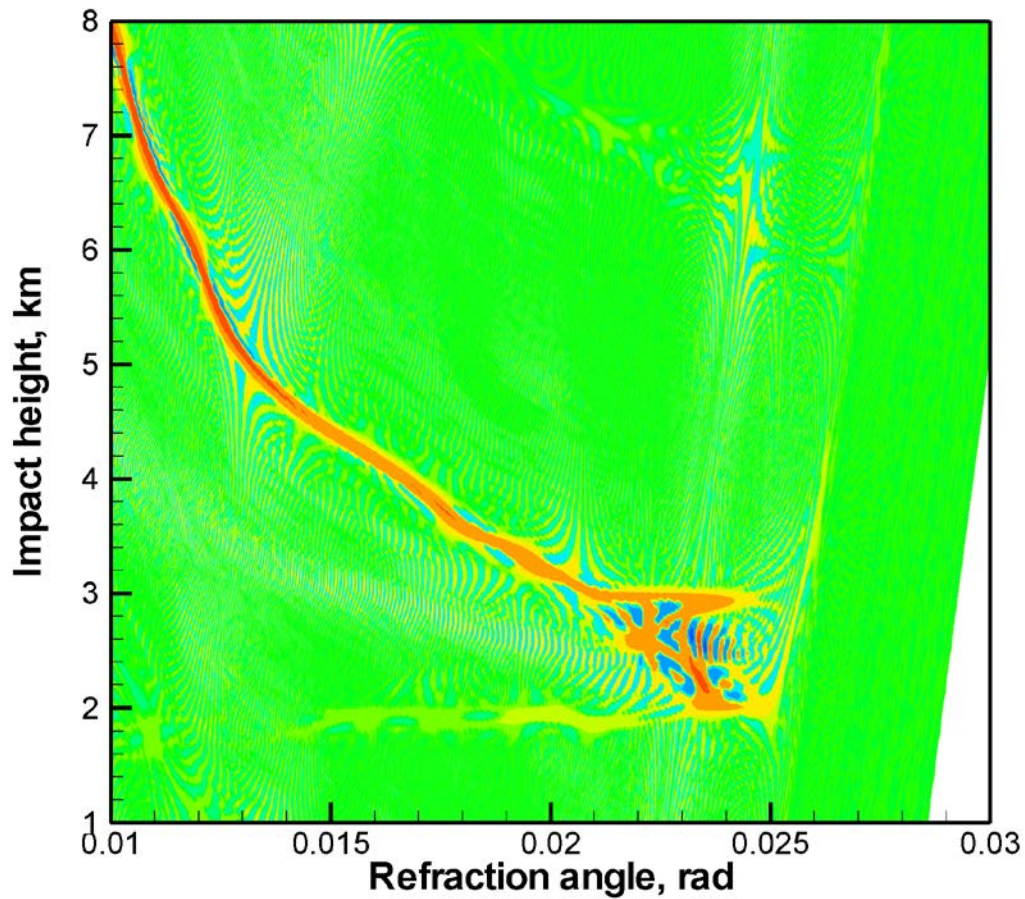
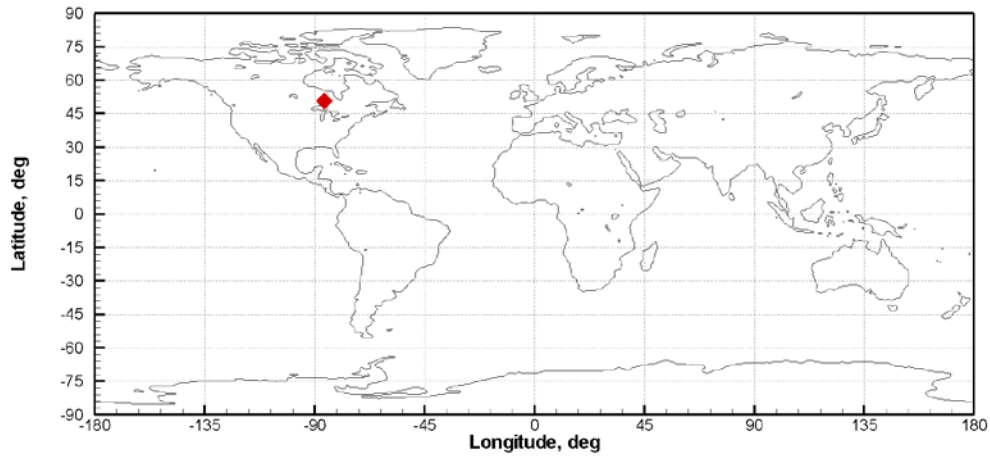


Figure 17. Simulated reflection over ocean.



2008/01/01; 01:01:50.000; 50.66N 86.03W

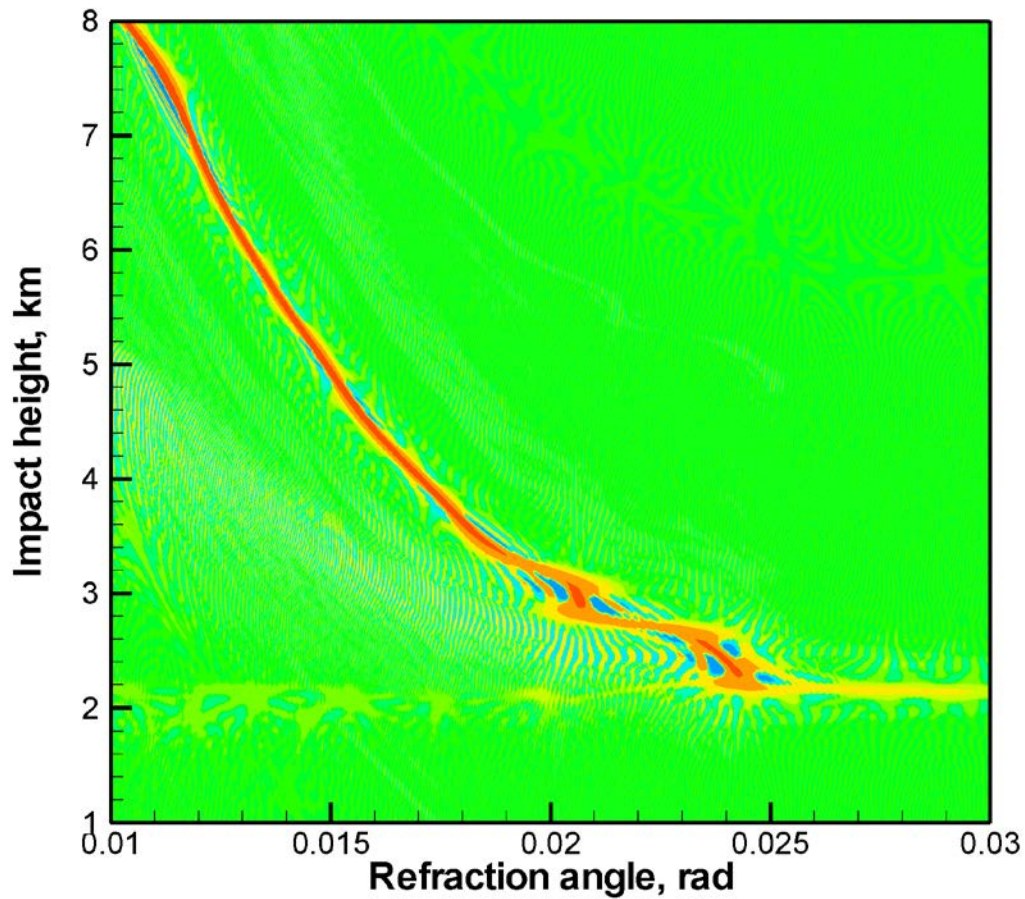
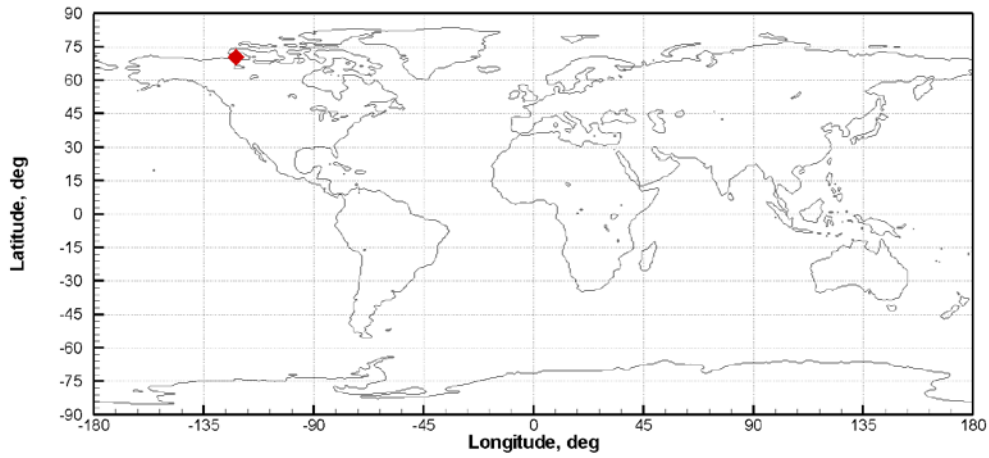


Figure 18. Simulated reflection over land.



2008/01/01; 01:02:23.000; 70.28N 121.87W

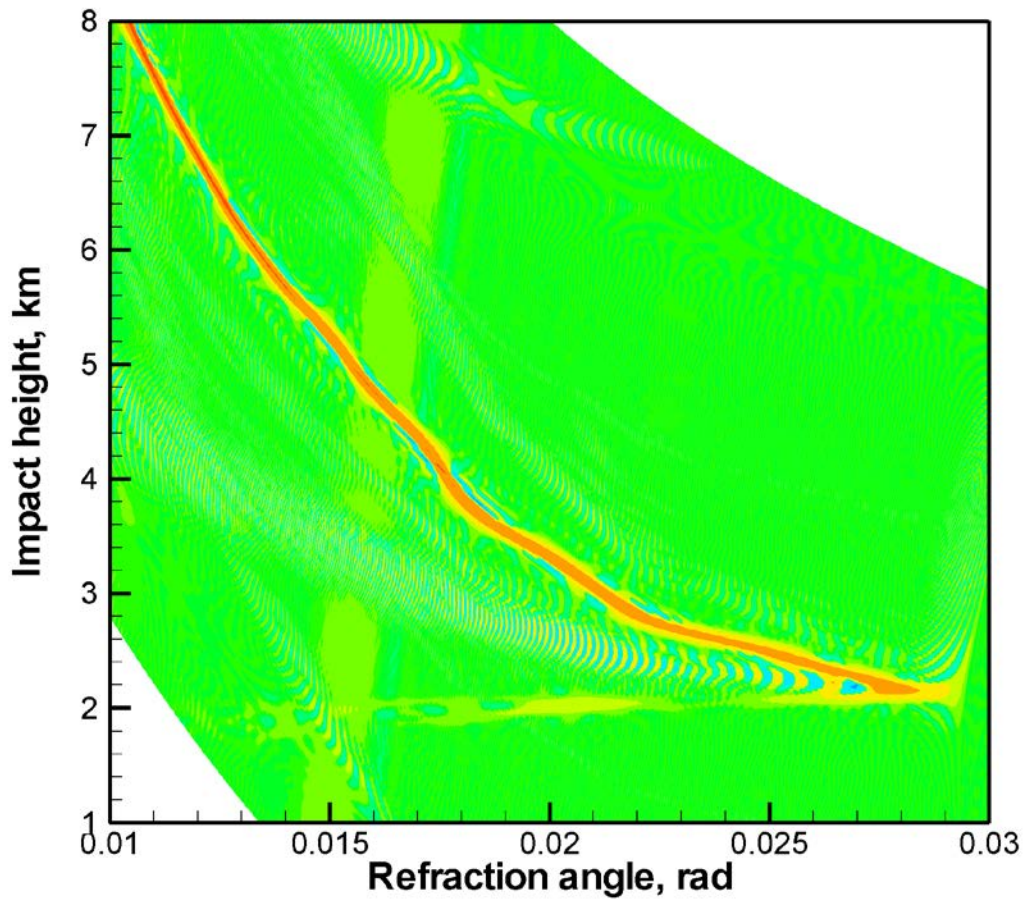
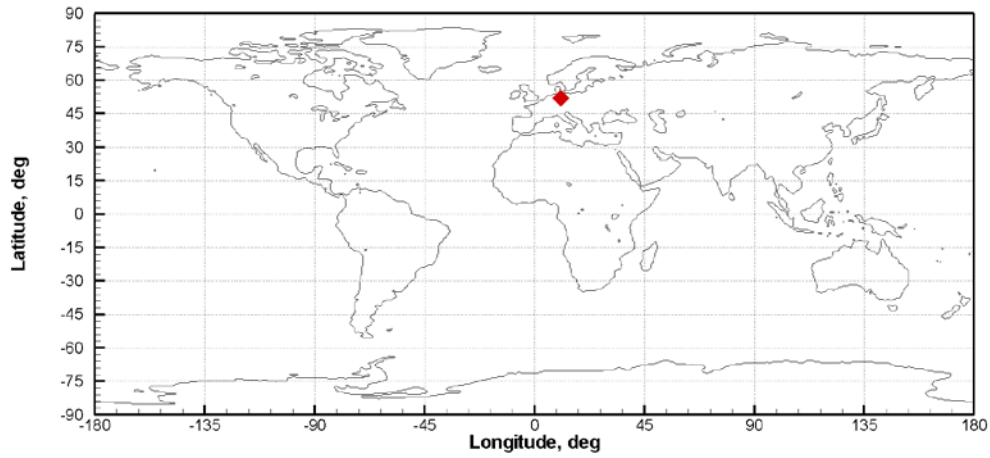


Figure 19. Simulated reflection over land.



2008/01/01; 01:02:30.000; 52.09N 10.81E

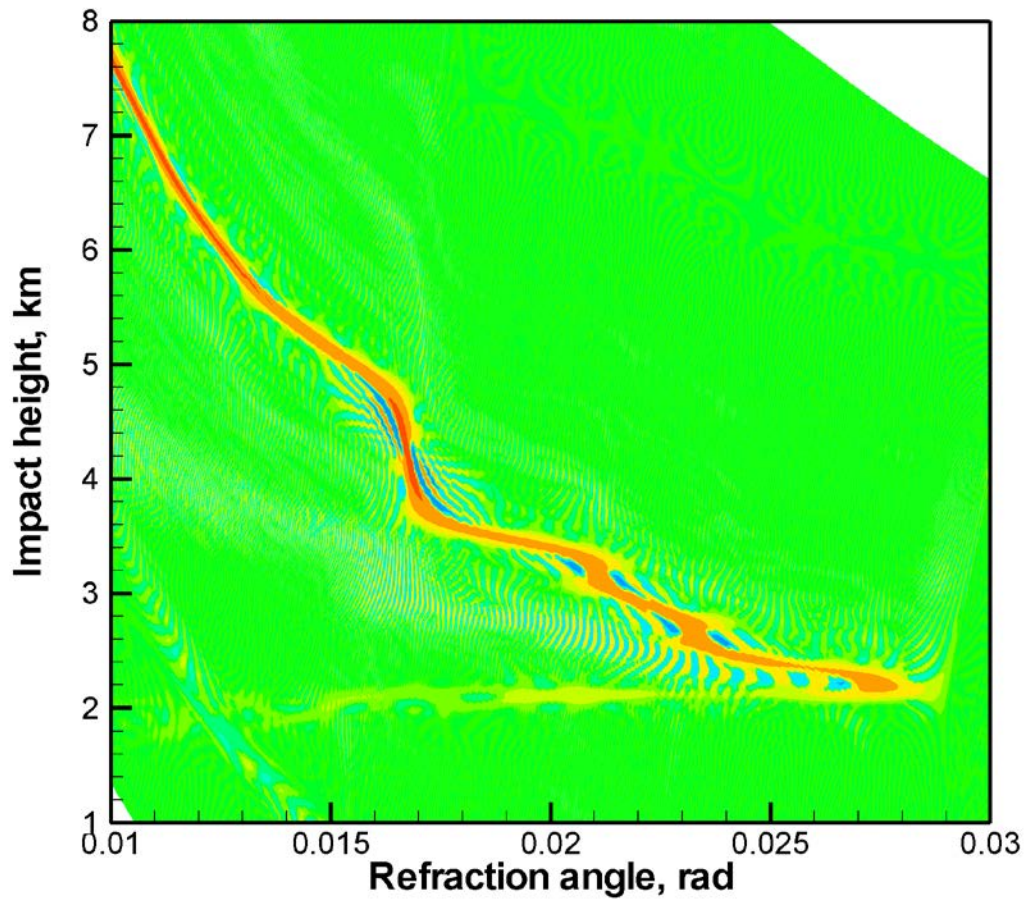
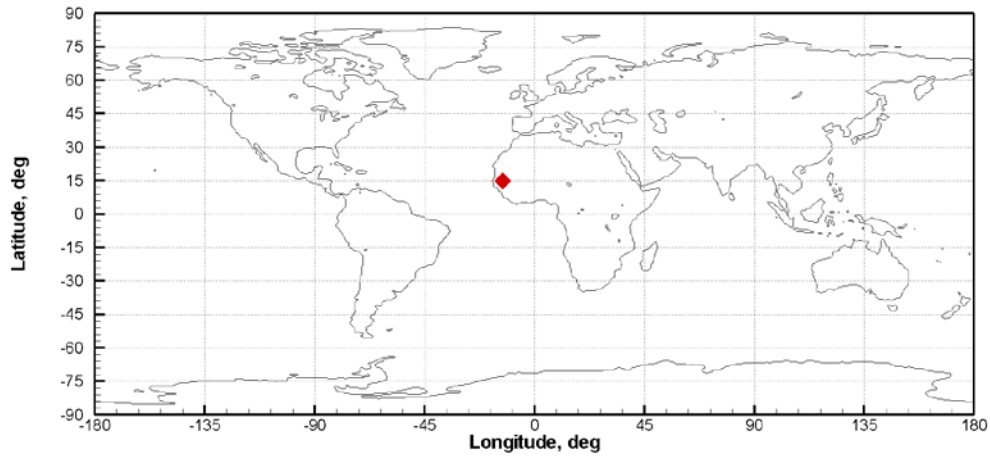


Figure 20. Simulated reflection over land.



2008/01/01; 01:25:23.000; 14.76N 13.13W

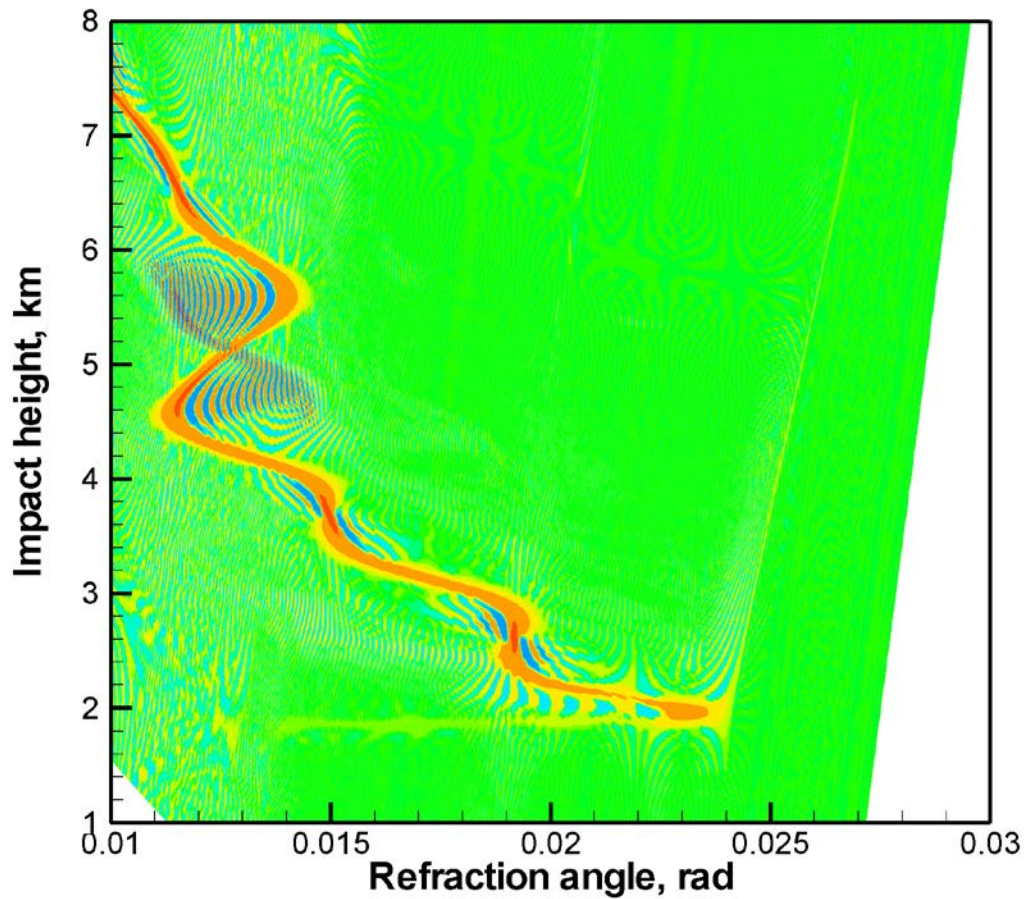
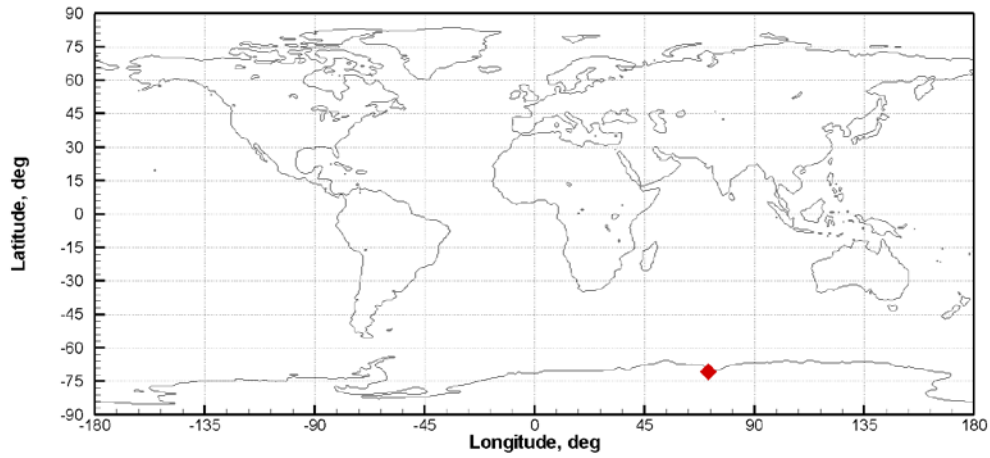


Figure 21. Simulated reflection over land.



2008/01/01; 01:54:49.000; 70.85S 71.01E

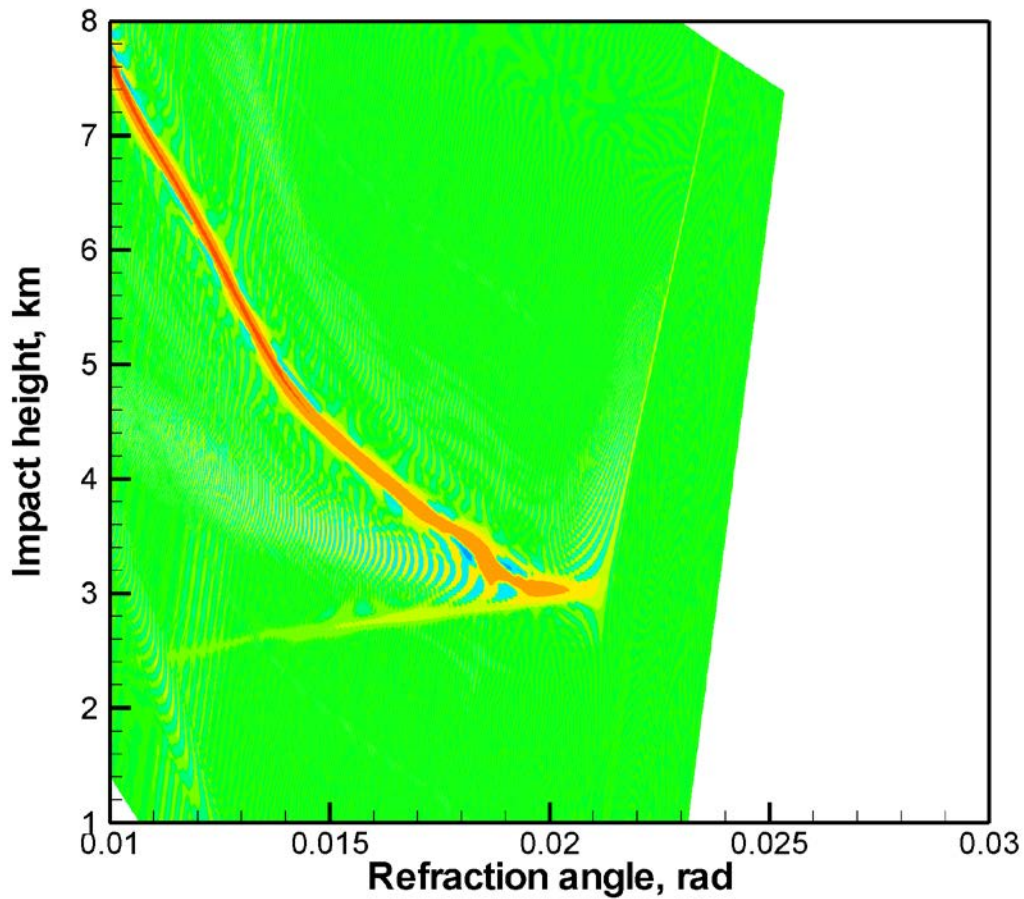
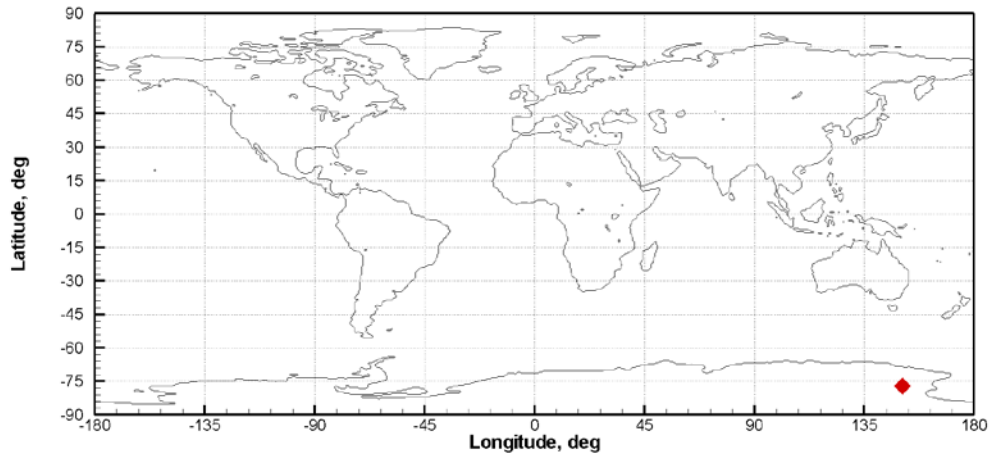


Figure 22. Simulated reflection over Antarctica.



2008/01/01; 01:58:34.000; 77.26S 150.57E

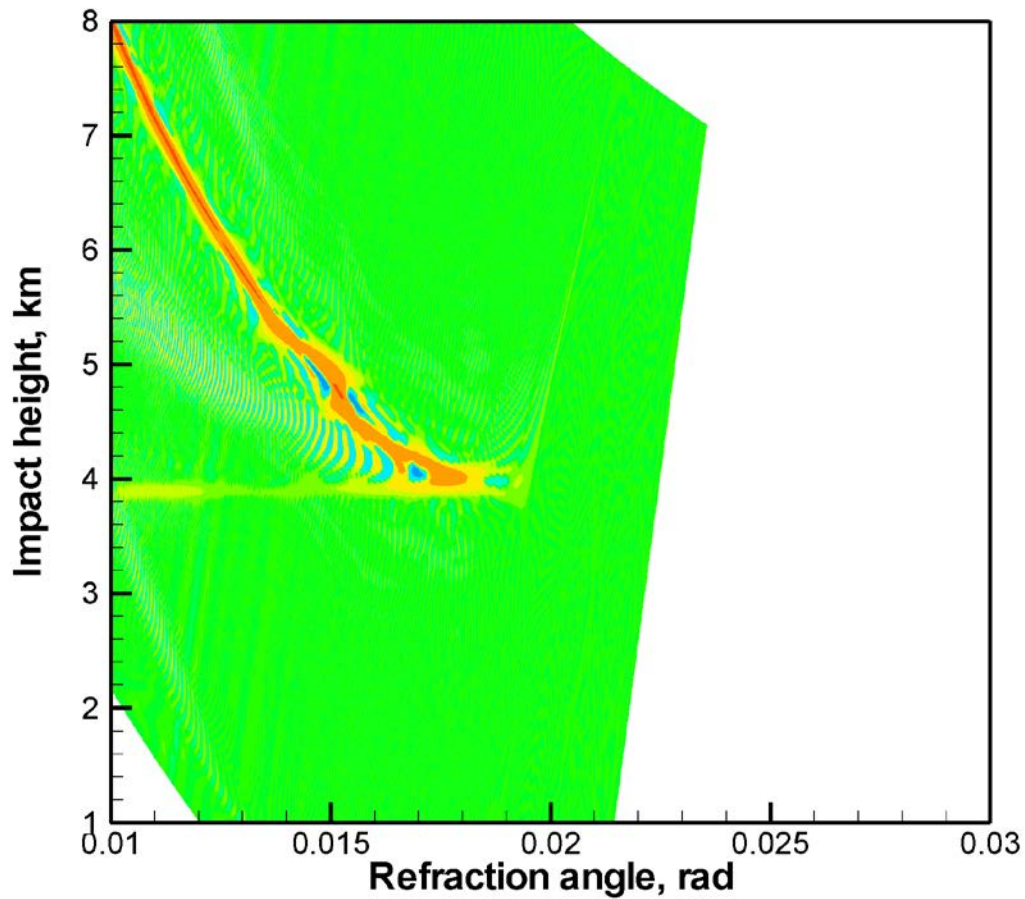
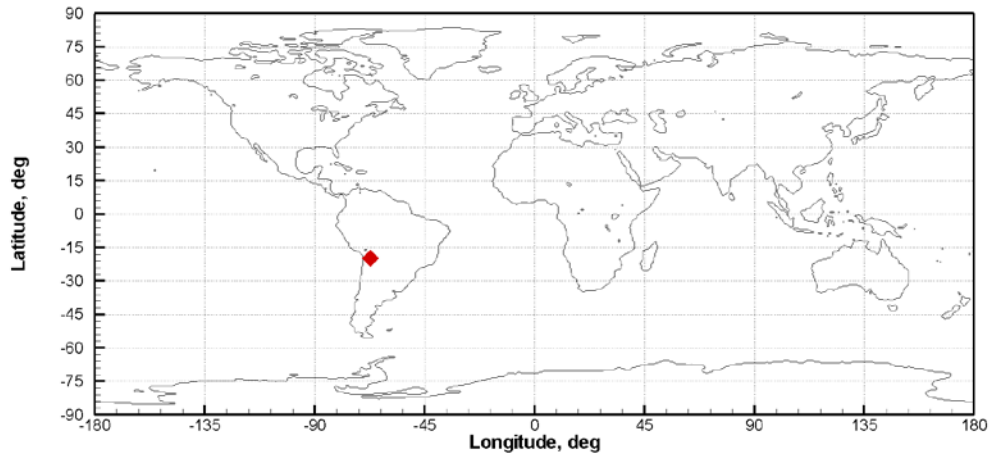


Figure 23. Simulated reflection over Antarctica.



2008/01/01; 01:00:04.990; 19.96S 67.12W

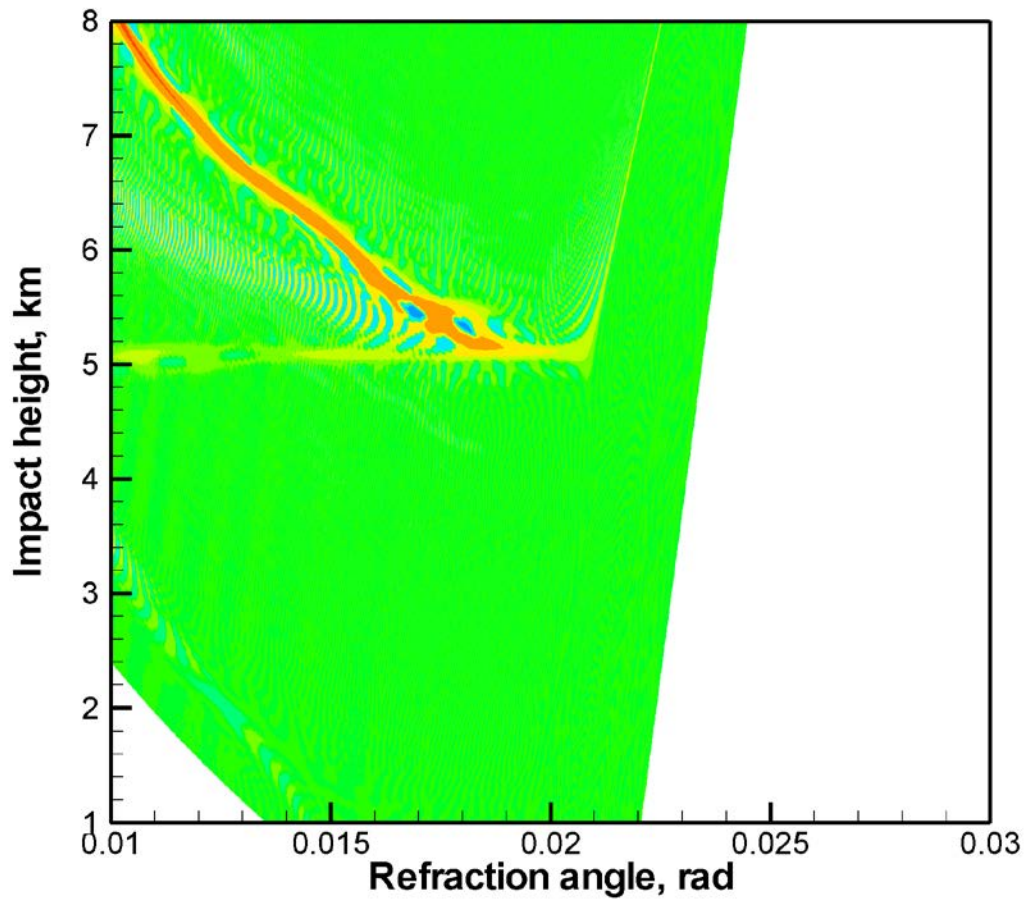
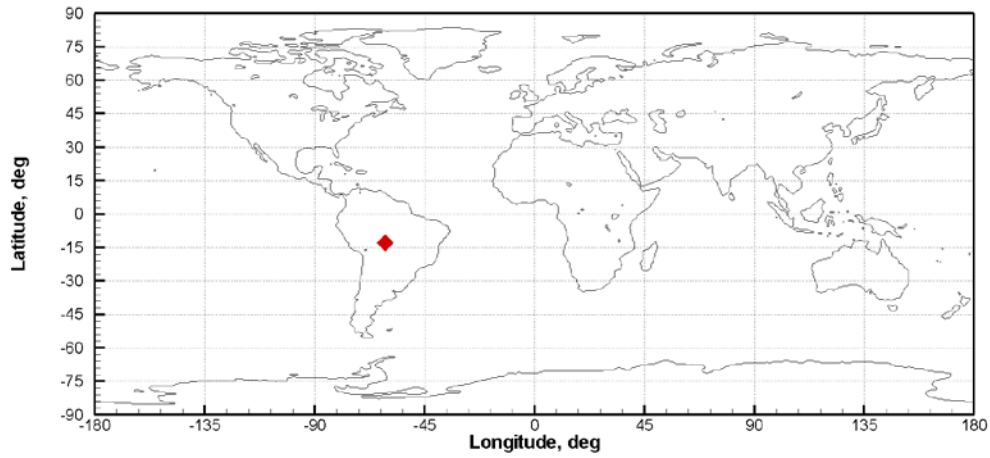


Figure 24. Simulated reflection over mountains.



2008/01/01; 01:02:27.000; 13.04S 61.08W

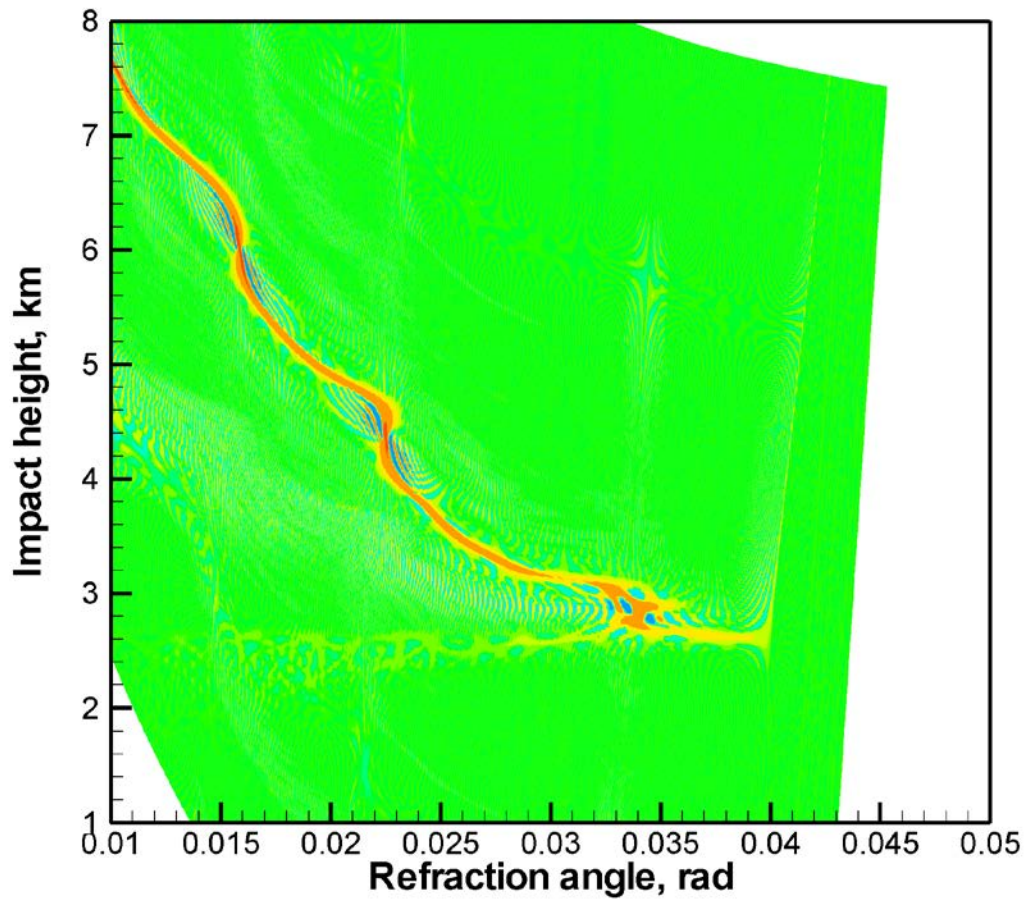


Figure 25. Simulated reflection over mountains.

3.7 Discussion

The above examples of observed and simulated reflections allow for the following conclusion. The simple reflection model implemented in WOP allows for a realistic modelling of reflections not taking into account the reflective properties of the Earth's surface. Both observed and simulated reflections indicate a very rapid increase of the bending angle of reflected rays, ε_R as a function of impact parameter p . Dependence $\varepsilon_R(p)$ is mostly confined in a narrow impact parameter interval of about 100 m. Often $\varepsilon_R(p)$ is a multi-valued function. This indicates the method of choice should be the time domain retrieval preceded by the extraction of the reflected signal by using the filtering in the impact parameter space, as described in Section 3.2. Below we will describe the implementation of this approach and its results.

4. Reflection Retrieval Implementation

4.1 Phase Model for Reflected RO Signals

The phase model will play an important role in our further discussion. Here we describe the algorithm for the evaluation of the phase model for reflected RO signals. Given a spherically symmetric model of the neutral atmosphere $n_M(r)$, where r is the distance from the Earth's curvature center, the corresponding bending angle profile for reflected rays is expressed as follows [19]:

$$\varepsilon_{MR}(p) = -2p \int_{p_E}^{\infty} \frac{d \ln n_M}{dx} \frac{dx}{\sqrt{x^2 - p^2}} - 2 \arccos\left(\frac{p}{p_E}\right), \quad (37)$$

where $x(r) = rn_M(r)$ is the refractive radius, the first $\sqrt{\quad}$ term staying for the refraction due refractivity gradient, and the second term describing the ray bending due to the reflection at the surface, $p_E = r_E n_M(r_E)$, and r_E is the Earth's curvature radius with the account of the surface height above the reference ellipsoid. Our neutral atmospheric model $n_M(r)$ is based on the MSIS-90 model complemented with 80% relative humidity below 15 km as described in [20].

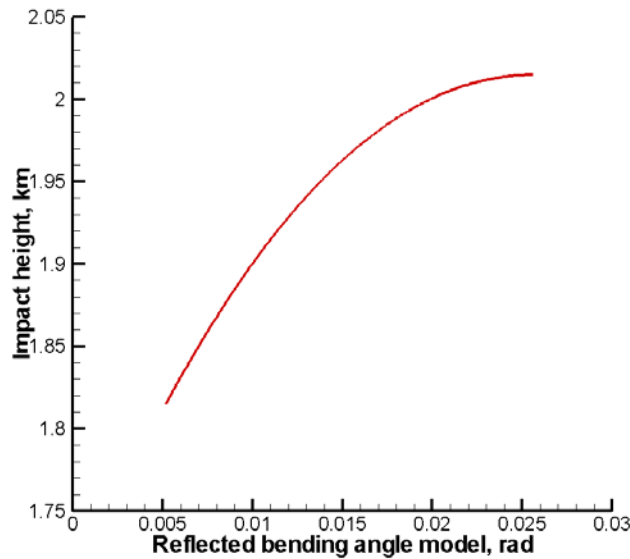


Figure 26. Reflected bending angle model for occultation event 2008/01/01, UTC 01:02:23, 70.28°N 121.87°W.

An example of reflected bending angle model $\varepsilon_{MR}(p)$ is shown in Figure 26.

Together with the satellite orbit data, the model bending angle profile $\varepsilon_{MR}(p)$ allows for the determination of the phase excess for the reflected rays. To this end, we have first to numerically solve the following equation:

$$\theta(t) = \varepsilon_{MR}(p) + \arccos \frac{p}{r_{Tx}(t)} + \arccos \frac{p}{r_{Rx}(t)}, \quad (38)$$

where $\theta(t)$ is the satellite-to-satellite angle with respect to the local curvature center, $r_{Tx,Rx}(t)$ are the radial coordinates of the satellites, hereinafter index Tx staying for the transmitter and index Rx staying for the receiver. The equation is solved for time t for each prescribed impact parameter. This allows for the determination of impact parameters as function of time, $p_{MR}(t)$. Dependence $p_{MR}(t)$ is always single-valued for reflected rays, because reflected bending angle profiles are monotonic and do not result in multipath propagation. This is illustrated by Figure 1 and explained by eq. (37), where the derivative of the second, reflective term proves to be much stronger than that of the first, refractive term, for any possible atmospheric conditions.

Given satellite coordinates $\mathbf{x}_{Tx,Rx}(t)$, the ray directions at the satellites, unit vectors $\mathbf{u}_{Tx,Rx}(t)$ are inferred from $p(t)$ using the geometrical relationships:

$$\begin{aligned} \mathbf{x}_{Rx}(t) \times \mathbf{u}_{Rx}(t) &= \mathbf{x}_{Tx}(t) \times \mathbf{u}_{Tx}(t), \\ |\mathbf{x}_{Rx}(t) \times \mathbf{u}_{Rx}(t)| &= |\mathbf{x}_{Tx}(t) \times \mathbf{u}_{Tx}(t)| = p, \end{aligned} \quad (39)$$

which expresses the fact that rays lie in the vertical occultation plane, and the impact parameter has the same value at the transmitter and at the receiver.

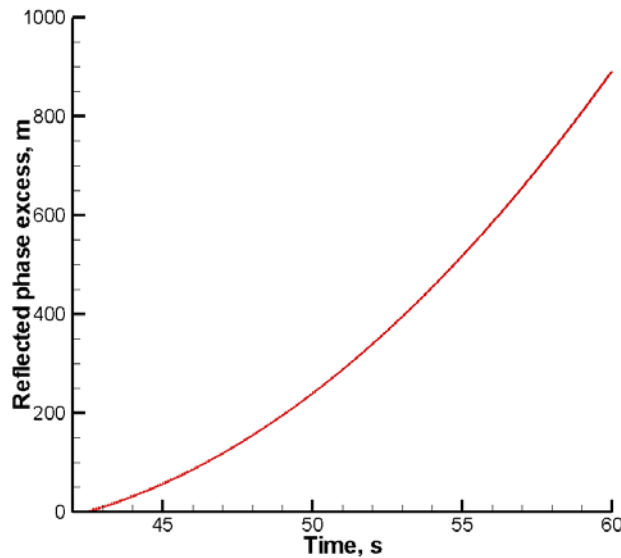


Figure 27. Reflected phase excess model for occultation event 2008/01/01, UTC 01:02:23, 70.28°N 121.87°W.

Using the satellite velocities $\mathbf{V}_{Rx,Tx}(t)$, we find the relative Doppler frequency shift

$d_{MR}(t)$

$$\frac{c - \mathbf{V}_{Rx}(t) \cdot \mathbf{u}_{Rx}(t)}{c - \mathbf{V}_{Tx}(t) \cdot \mathbf{u}_{Tx}(t)} \sqrt{\frac{c^2 - V_{Tx}^2(t)}{c^2 - V_{Rx}^2(t)}} - 1 = d_{MR}(t). \quad (40)$$

The phase excess is obtained by integrating the Doppler shift:

$$S_{MR}(t) = c \int \left(d^{(0)}(t) - d_{MR}(t) \right) dt, \quad (41)$$

where $d^{(0)}(t)$ is the vacuum Doppler shift for the direct rays, evaluated from (40), by inserting unit vector $\mathbf{u}_{Tx,Rx}^{(0)}(t)$ corresponding to satellite-to-satellite straight-line direction. An example of reflected phase excess model is shown in Figure 27.

4.2 Radio Holographic Index of Reflections

The idea of flagging radio occultation with an index of the strength of the reflected ray consists in the following. Although the amplitude of the reflected signal is weak as compared to the direct signal, the instant frequencies of the reflected signal concentrate around the instant frequencies of the model reflected signal. Therefore, we can use the model reflected signal $\exp(ikS_{MR}(r))$ as the reference signal and evaluate the radio holographic spectrum as follows:

$$\tilde{u}_R(\omega) = \int A(t) \exp\left(ik[S(t) - S_{MR}(t) - \omega]\right) dt. \quad (42)$$

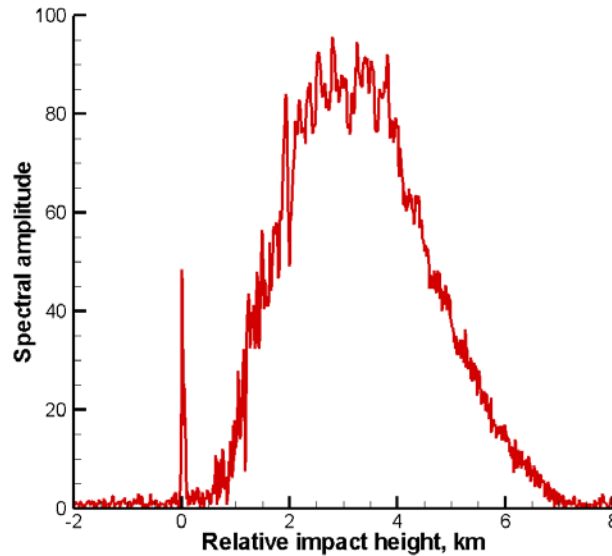


Figure 28. Radio holographic spectrum amplitude $|\tilde{u}_R(\omega)|$ for occultation event 2008/01/01, UTC 01:02:23, 70.28°N 121.87°W.

The integration here covers the time interval, for which we can evaluate the reflected phase excess model. Each frequency ω can be transformed to equivalent impact parameters using relationships (40) and (39). This allows for considering the spectrum as a function of impact parameter related to middle point t_0 of the time interval. Moreover, it is convenient to introduce the reference value p_0 of the impact parameter, corresponding to frequency

$\omega_0 = \dot{S}_{MR}(t_0)$. The spectrum can be considered as function $\tilde{u}_R(\Delta p)$ of relative impact height $\Delta p = p - p_0$.

An example of radio holographic spectrum is shown in Figure 28. The spectrum indicates a distinct spike near $\Delta p = 0$, corresponding to reflection. The presence of reflection is also confirmed by the Wigner function plot.

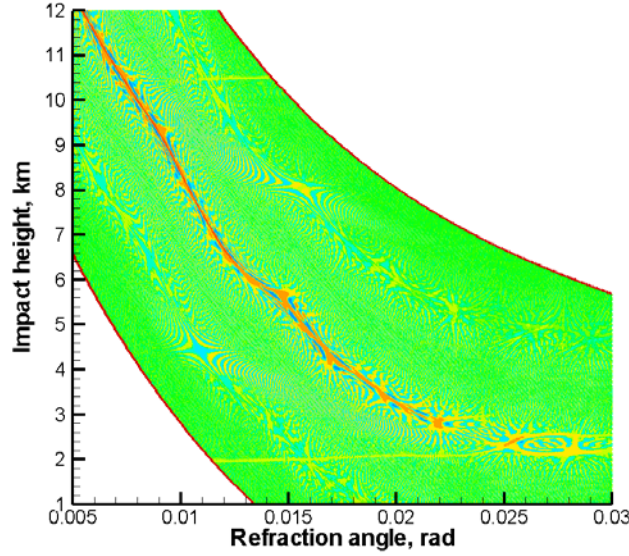


Figure 29. Wigner function for occultation event 2008/01/01, UTC 01:02:23, 70.28°N 121.87°W.

Using the radio holographic spectrum, we define the reflection index as follows:

$$\begin{aligned}
 \tilde{u}_{\max} &= \max_{[-0.3, 0.3]} |\tilde{u}(\Delta p)|^2, \\
 \tilde{u}_{\text{ave}} &= \left\langle |\tilde{u}(\Delta p)|^2 \right\rangle_{[-0.3, 0.3]}, \\
 \tilde{u}_{\text{bkg}} &= \left\langle |\tilde{u}(\Delta p)|^2 \right\rangle_{[-2.0, 1.0]}, \\
 I_R &= \frac{\tilde{u}_{\max}^2}{\tilde{u}_{\text{ave}} (\tilde{u}_{\max} + \alpha \tilde{u}_{\text{bkg}})},
 \end{aligned} \tag{43}$$

where \tilde{u}_{\max} is the maximum of the spectral density taken within the interval of $\Delta p \in [-0.3 \text{ km}, 0.3 \text{ km}]$, \tilde{u}_{ave} is the spectral density averaged over the same interval, \tilde{u}_{bkg} is the background (noise level) spectral density estimated by averaging over the interval of $\Delta p \in [-2.0 \text{ km}, -1.0 \text{ km}]$, and α is the regularization parameter, which we take to equal 3. The index characterizes the strength of the spectral spike and suppresses random spikes at noise level. The value of $I_R = 0.25$ corresponds to a flat radio holographic spectrum, i.e. a definite absence of reflection. For the illustrative event considered above, the index has a value of 17.917.

4.3 Filtering in Impact Parameter Space

In order to extract the reflected field component $u_R(t)$, we implemented the filtering in the impact parameter space. In Figure 29, we see that the reflected ray is observed both around impact height of 2 km and 10.5 km. The latter originates from aliasing, where the Doppler frequency shift of the reflected ray deviates from the direct ray phase excess model by more than a half of the receiver band width, which equals 50 Hz. The impact parameters difference Δp_{alias} between non-aliased and aliased components for typical observation geometry is about 8–10 km. The exact value Δp_{alias} for a specific event is evaluated by using GO relationship (39) and (40). To this end, we evaluate impact height from the original relative Doppler shift, and from the relative Doppler shift corresponding to the aliased frequency shifted by the sampling rate.

In order to retain the aliased component, we modify filter (31) as follows:

$$u_R(t) = \hat{\Phi}_2^{-1} \left[\hat{\Phi}_2 [u(t)] \chi(\tilde{p}) \right], \quad (44)$$

where $\chi(\tilde{p})$ is defined as follows:

$$\chi(\tilde{p}) = \begin{cases} \exp\left(-(\tilde{p}_E - \Delta p_R - \tilde{p})^2 / \delta p_R^2\right), & \tilde{p} < \tilde{p}_E - \Delta p_R; \\ 1, & \tilde{p}_E - \Delta p_R \leq \tilde{p} < \tilde{p}_E; \\ \exp\left(-(\tilde{p} - \tilde{p}_E)^2 / \delta p_R^2\right) + \\ \quad + \exp\left(-(\tilde{p}_E + \Delta p_{\text{alias}} - \Delta p_R - \tilde{p})^2 / \delta p_R^2\right), & \tilde{p}_E \leq \tilde{p} < \tilde{p}_E + \Delta p_{\text{alias}} - \Delta p_R; \\ 1, & \tilde{p}_E + \Delta p_{\text{alias}} - \Delta p_R \leq \tilde{p} < \tilde{p}_E + \Delta p_{\text{alias}}; \\ \exp\left(-(\tilde{p} - \tilde{p}_E - \Delta p_{\text{alias}})^2 / \delta p_R^2\right), & \tilde{p}_E + \Delta p_{\text{alias}} < \tilde{p}. \end{cases} \quad (45)$$

This function is equal to unity inside the impact height interval of $[\tilde{p}_E - \Delta p_R, \tilde{p}_E]$ and the corresponding aliased interval of $[\tilde{p}_E + \Delta p_{\text{alias}} - \Delta p_R, \tilde{p}_E + \Delta p_{\text{alias}}]$. The width Δp_R of these intervals is set to 1 km. Outside these intervals, we employ the Gaussian apodization with a characteristic width of $\delta p_R = 0.2$ km. Apodization allows for avoiding sharp boundaries of the filtering function, improving the filter quality.

4.4 Reflected Bending Angle Retrieval in Time Domain

Above, we have employed the CT technique to extract the reflected field component $u_R(t)$. Our previous consideration indicates that, this done, the standard GO retrieval in the time domain has a clear advantage over other approaches. This is explained by the following. Typical bending angle profiles for reflection indicate a very steep increase with

the impact parameter. Often, this profile is a multi-valued function of impact height p . On the other hand, reflected rays never interfere in the time domain.

The wave field $u_R(t)$ can be represented as $A_R(t) \exp(\exp i\varphi_R(t))$. We only use the phase samples $\varphi_R(t_i)$. First, we recover the original, not distorted by aliasing phase variation by using the phase model $S_R(t)$. To this end, we evaluate the phase deviation from the model:

$$\Delta\varphi_R(t_i) = [\varphi_R(t_i) - kS_{MR}(t_i)] \bmod 2\pi. \quad (46)$$

We re-accumulate (connect) the phase samples by adding a full number of cycle to each one:

$$\Delta\tilde{\varphi}_R(t_i) = \Delta\varphi_R(t_i) + 2\pi N_i, \quad (47)$$

so as to minimize the variations of $\Delta\tilde{\varphi}_R(t_i)$ between samples. Finally, the phase excess of the reflected rays is evaluated as follows:

$$S_R(t_i) = S_{MR}(t_i) + \frac{\Delta\tilde{\varphi}_R(t_i)}{k}. \quad (48)$$

The phase excess evaluated, we infer the bending angles $\varepsilon_R(t_i)$ and impact parameters $p(t_i)$ by inverting the GO relationships (38), (39), (40), and (41), used for the evaluation of the model phase excess $S_{MR}(t)$ from the bending angle profile $\varepsilon_{MR}(p)$.

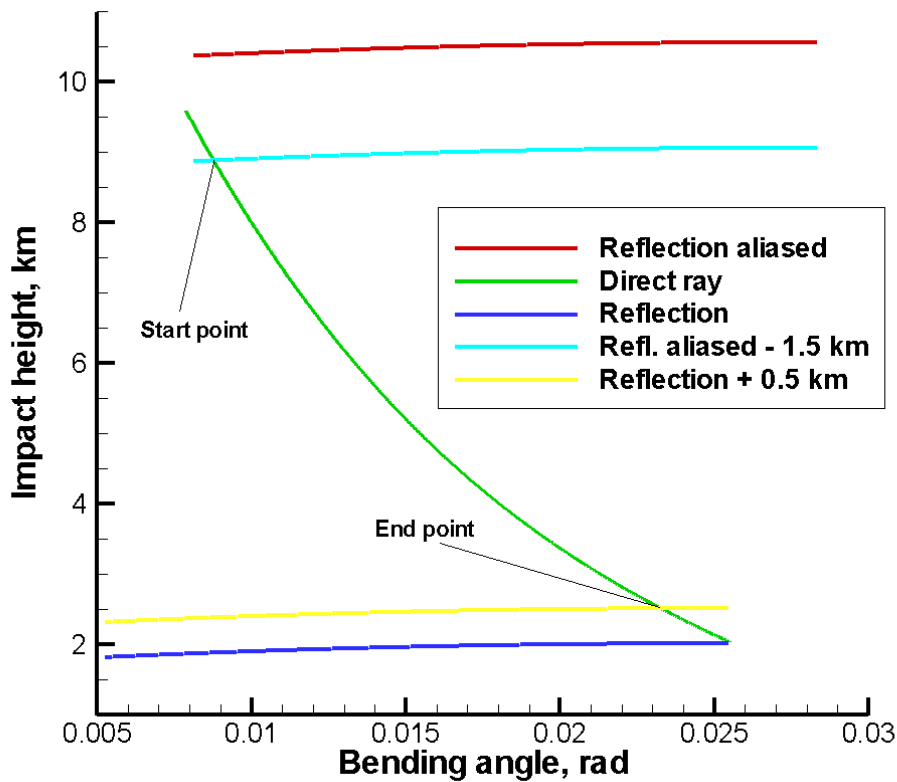


Figure 30. Determination of the safe time interval for the reflection retrieval.

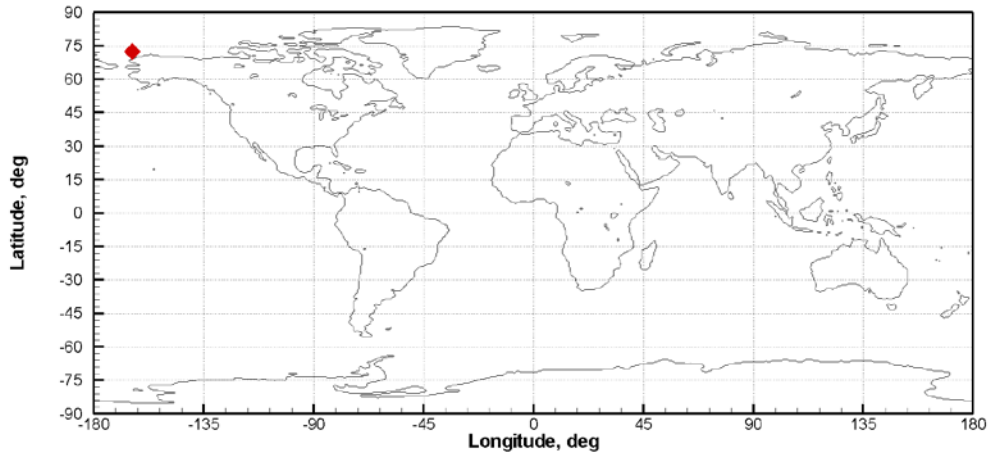
The reflected bending angle profile consists of two parts: initially non-aliased and the de-aliased one. Both branches intersect with the direct ray bending angle profile. Therefore, we need to choose the reflected profile part between the two intersection points. This is illustrated in Figure 30. For a safe estimate of the time interval for the reflection retrieval we use bending angle models for the reflected, aliased reflected, and direct ray. The time interval is defined as that between the intersections of the direct ray profile with aliased reflected profile with subtraction of safety border of 1.5 km, and the non-aliased reflection profile with the addition of safety border of 0.5 km.

In order to obtain the error bars, we apply the radio holographic estimate [16] of the impact parameter spectral width. The example, which we present in the next Sections, indicate that the error bar, by themselves, have a larger width as compared to the radio holographic spectra. This is explained by the fact that the reflection index uses the long-term radio holographic spectrum, while the error bars are inferred from the widths of short-term, sliding radio holographic spectra. Still, the relative value of the error bars provides a good measure of the reliability of the reflection retrieval.

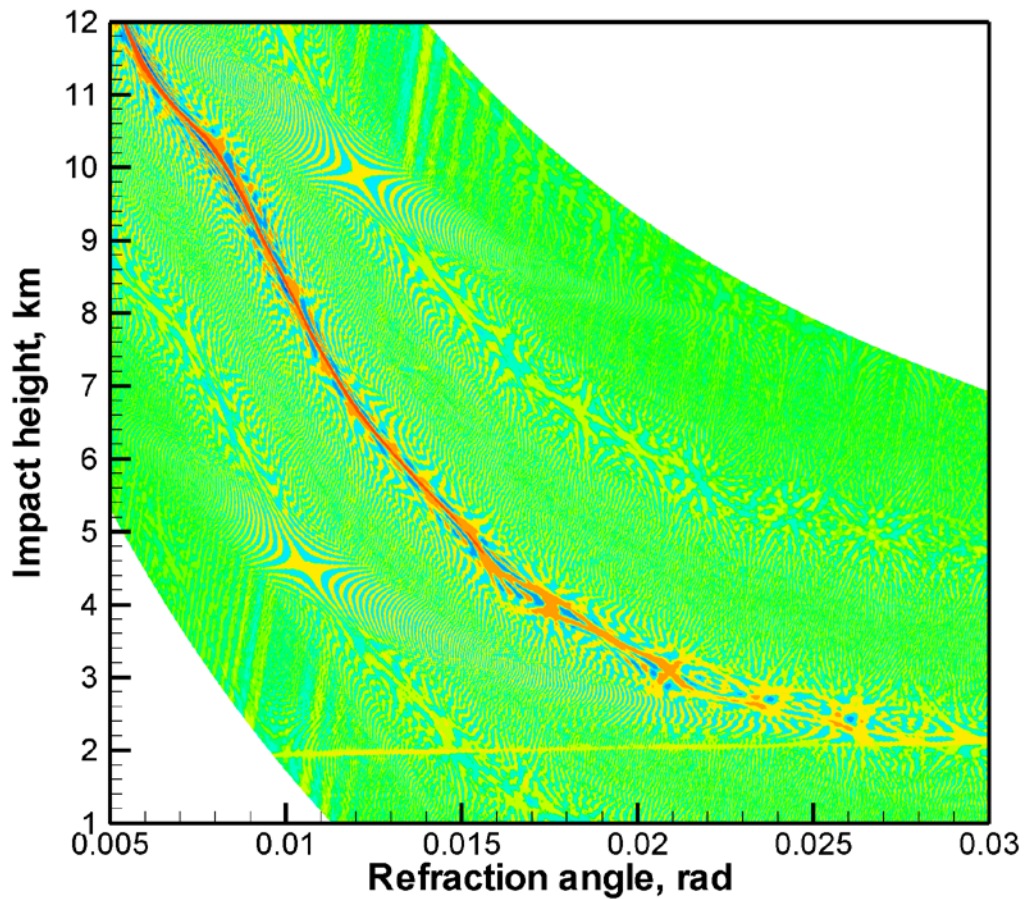
5. Examples of Processing COSMIC data

(1)

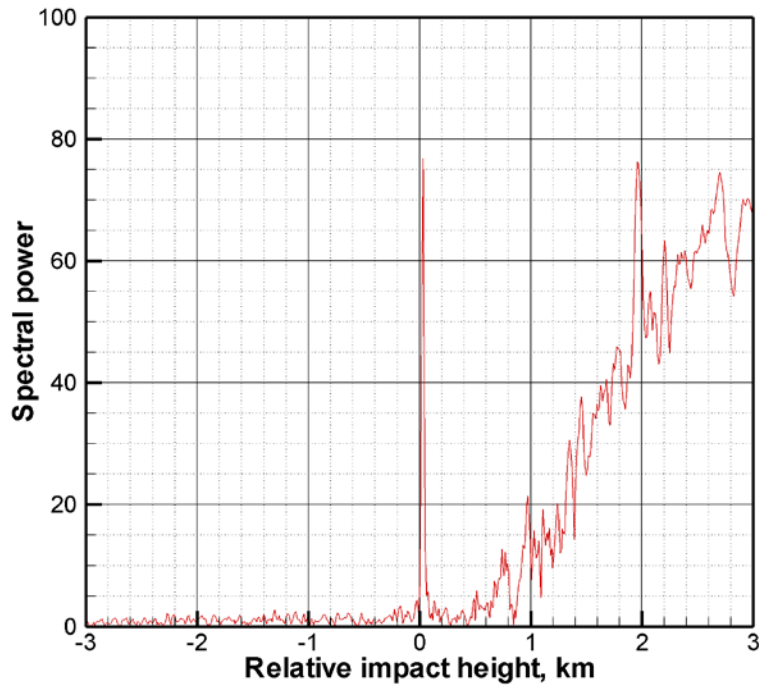
2008/01/01; 14:59:50.000; 72.34N 164.30W; 30.466



(2)



(3)



(4)

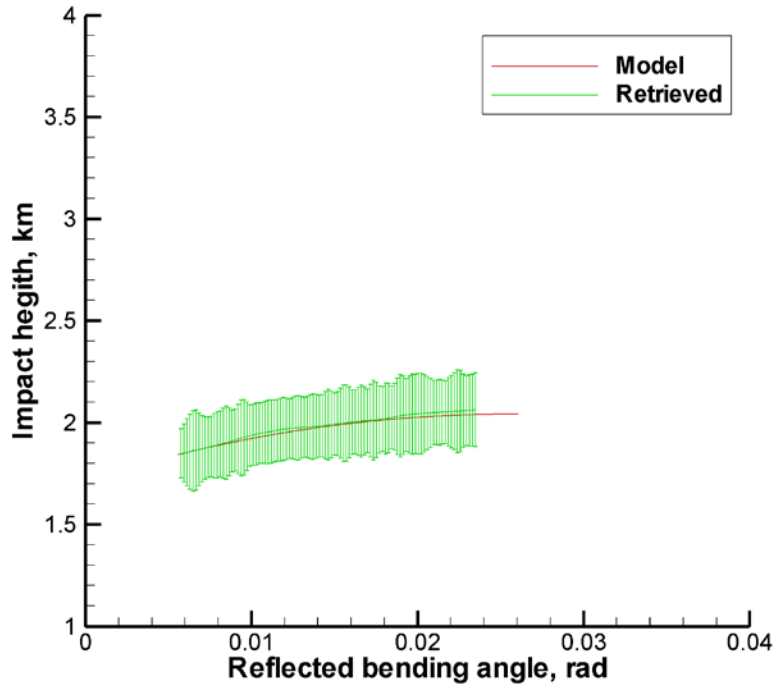
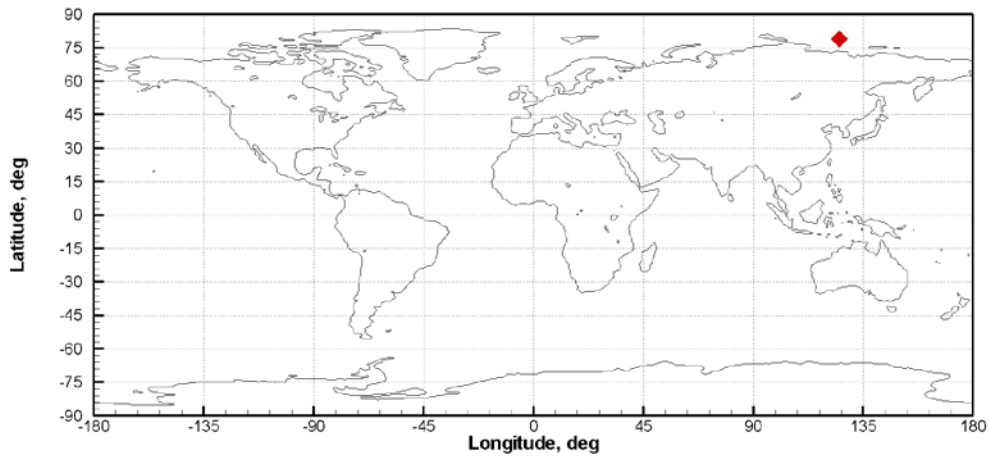


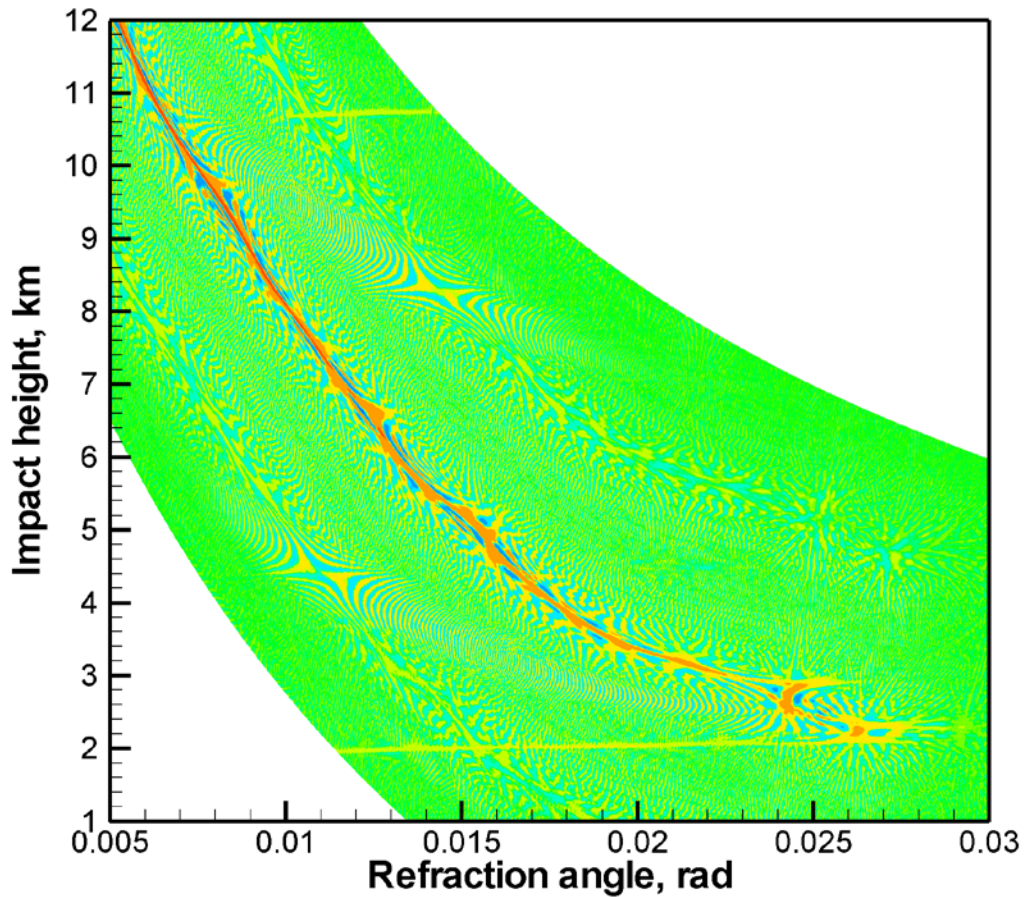
Figure 31. Occultation event with reflection. Reflection index 30.466. Panels from top to bottom: (1) location map, (2) WDF, (3) radio holographic spectrum, and (4) model and retrieved reflected bending angles with radio holographic error estimates.

(1)

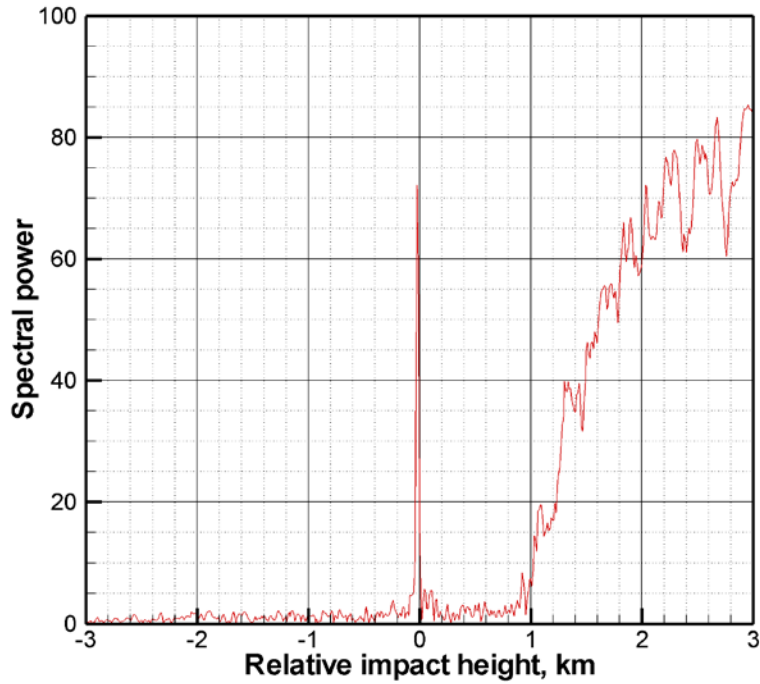
2008/01/01; 09:29:04.000; 78.92N 125.36E; 28.115



(2)



(3)



(4)

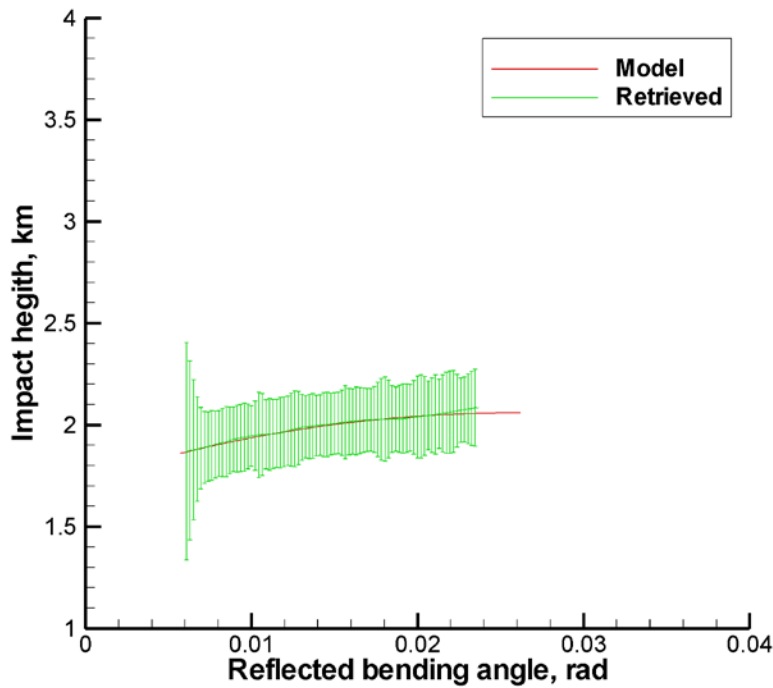
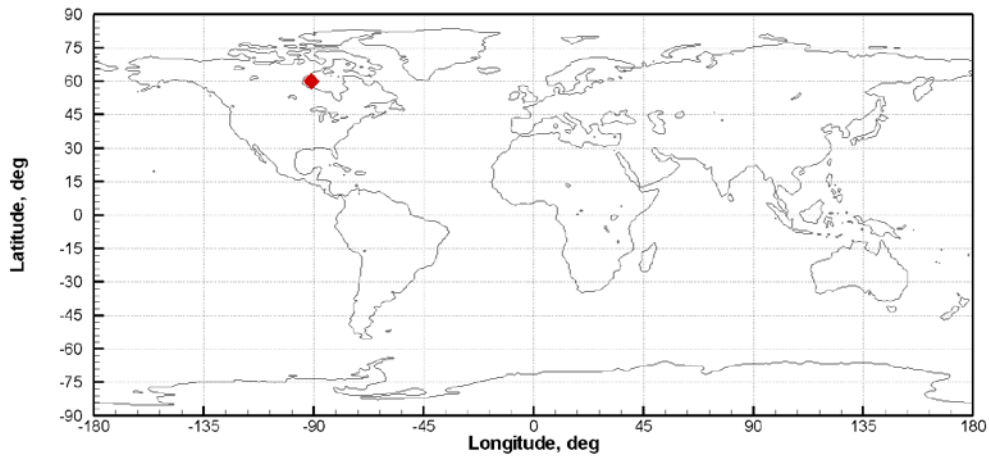


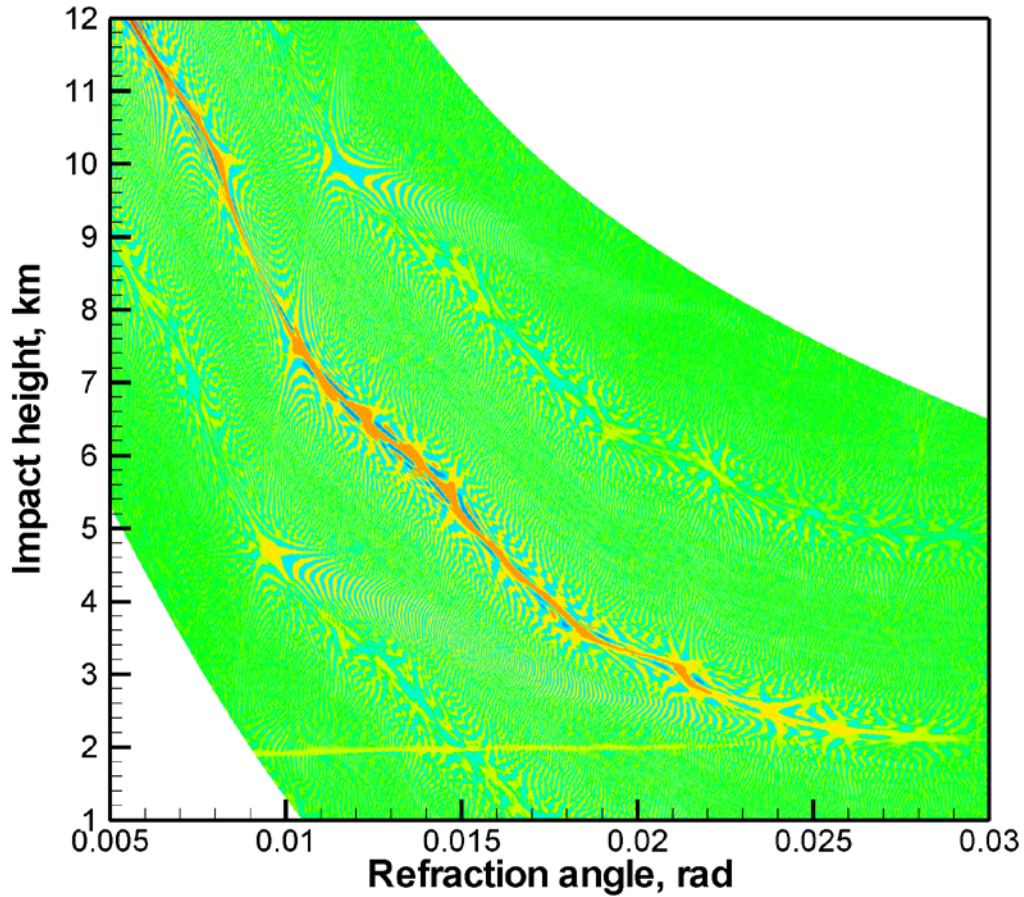
Figure 32. Occultation event with reflection. Reflection index 28.115. Panels from top to bottom: (1) location map, (2) WDF, (3) radio holographic spectrum, and (4) model and retrieved reflected bending angles with radio holographic error estimates.

(1)

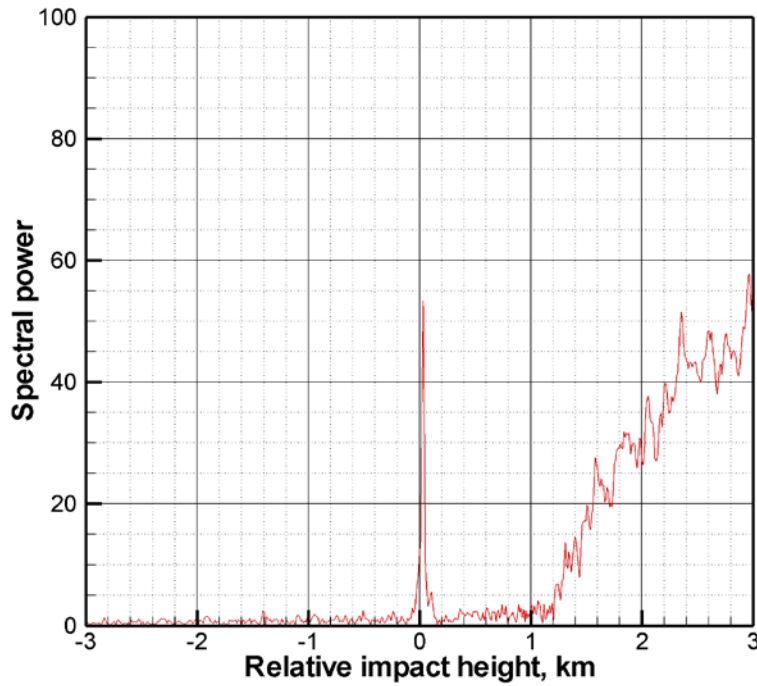
2008/01/01; 04:33:31.000; 60.00N 91.02W; 26.163



(2)



(3)



(4)

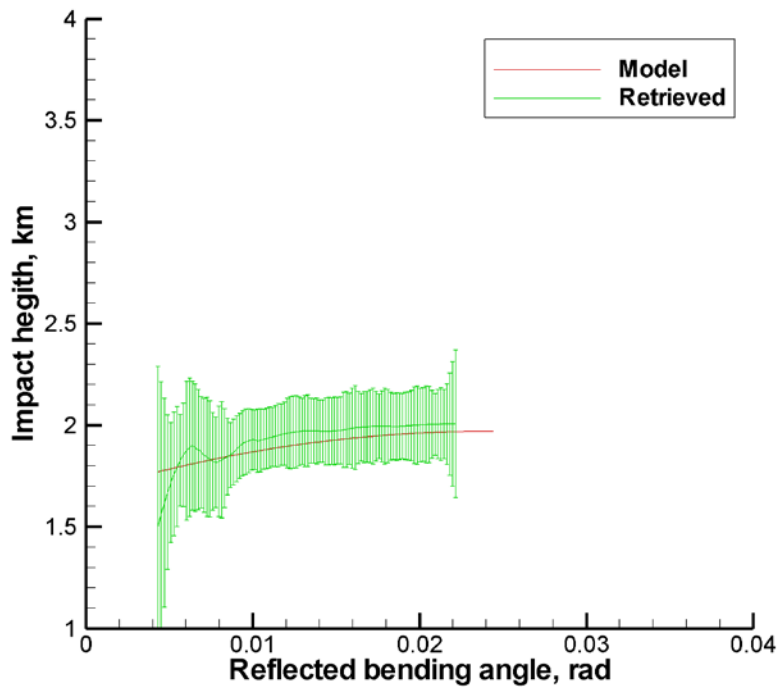
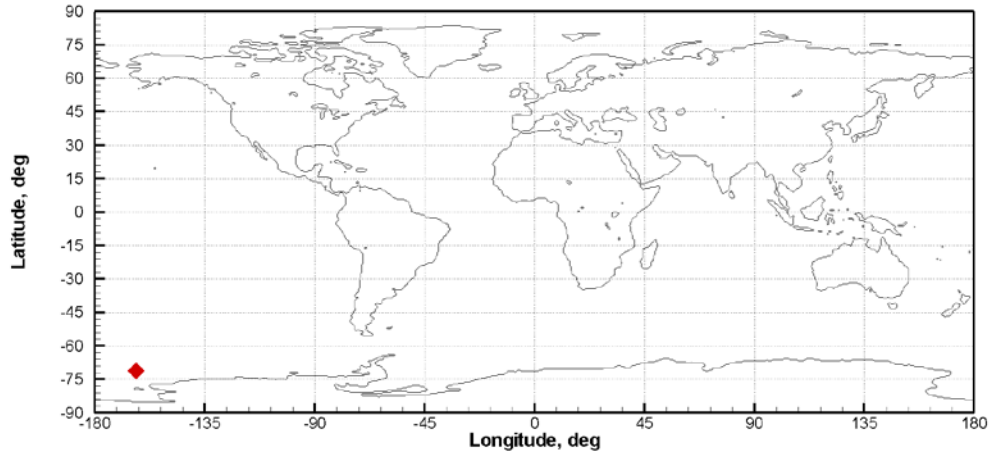


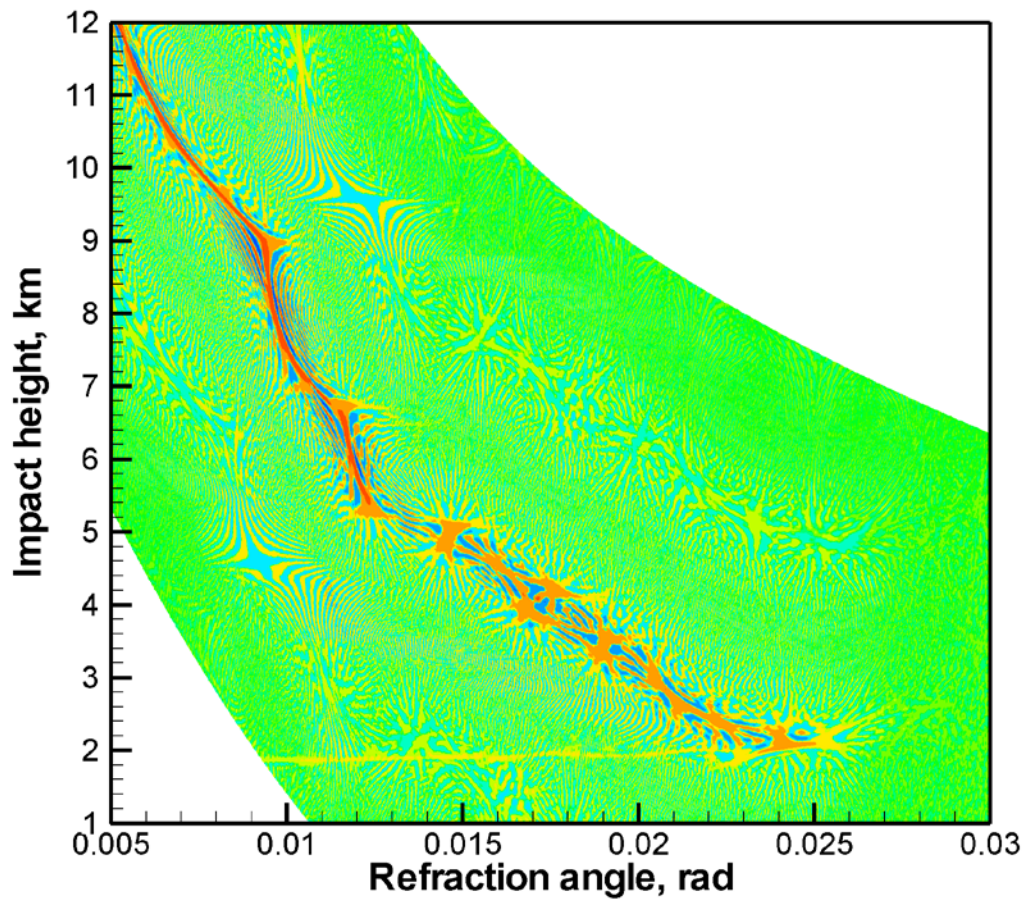
Figure 33. Occultation event with reflection. Reflection index 26.163. Panels from top to bottom: (1) location map, (2) WDF, (3) radio holographic spectrum, and (4) model and retrieved reflected bending angles with radio holographic error estimates.

(1)

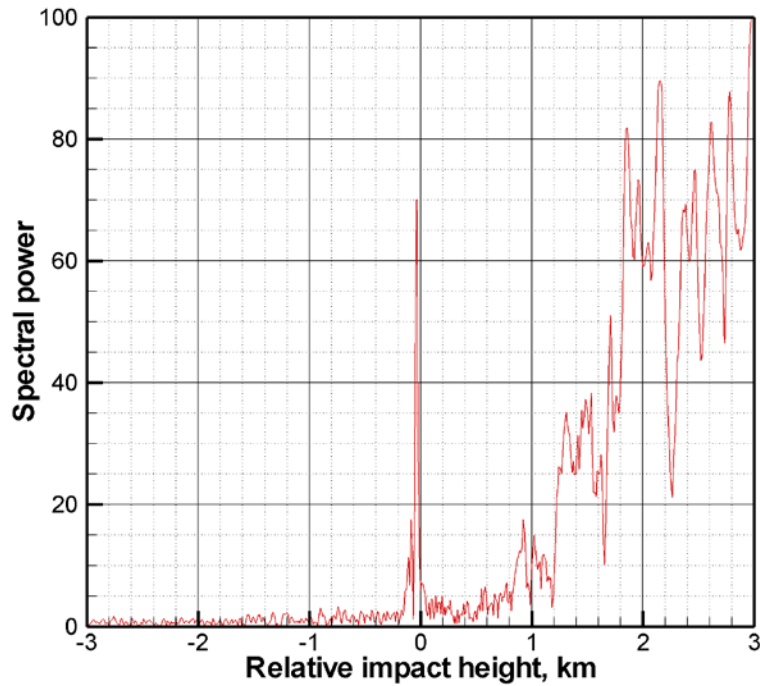
2008/01/01; 02:38:12.000; 71.32S 163.05W; 24.979



(2)



(3)



(4)

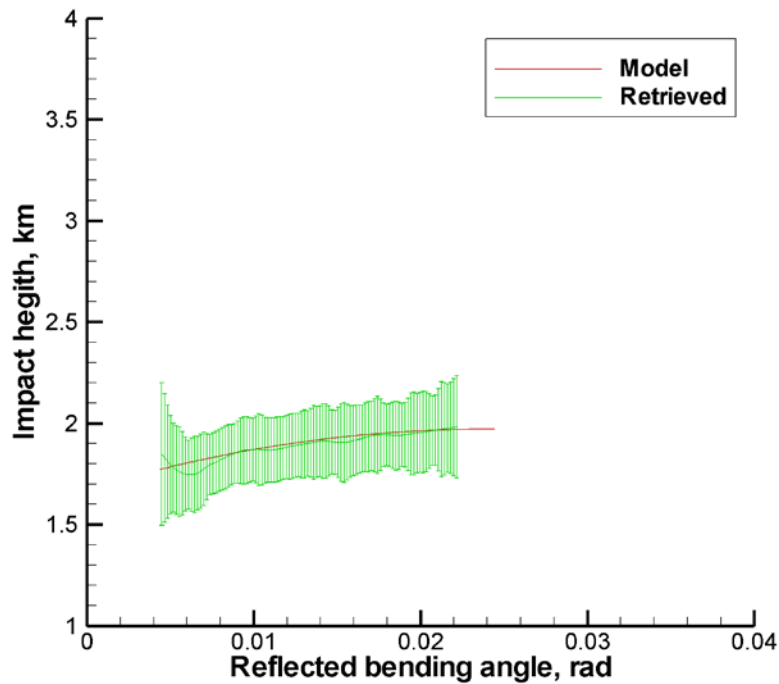
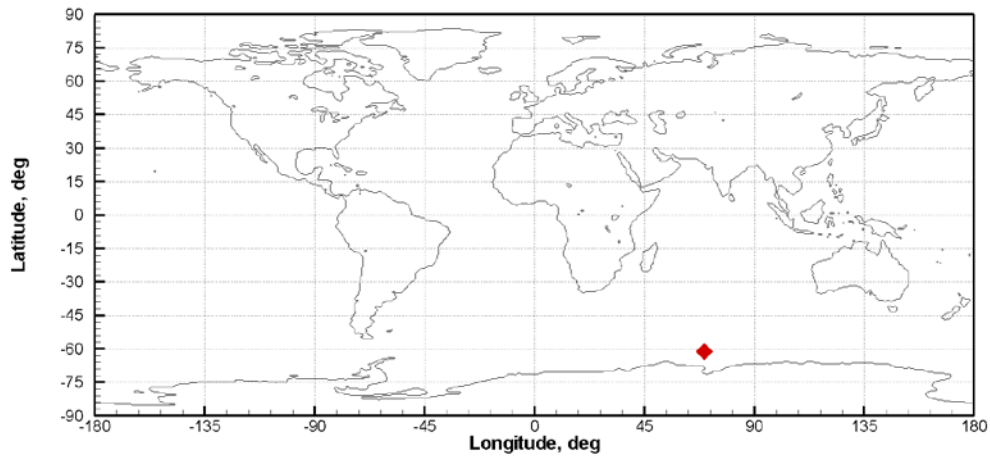


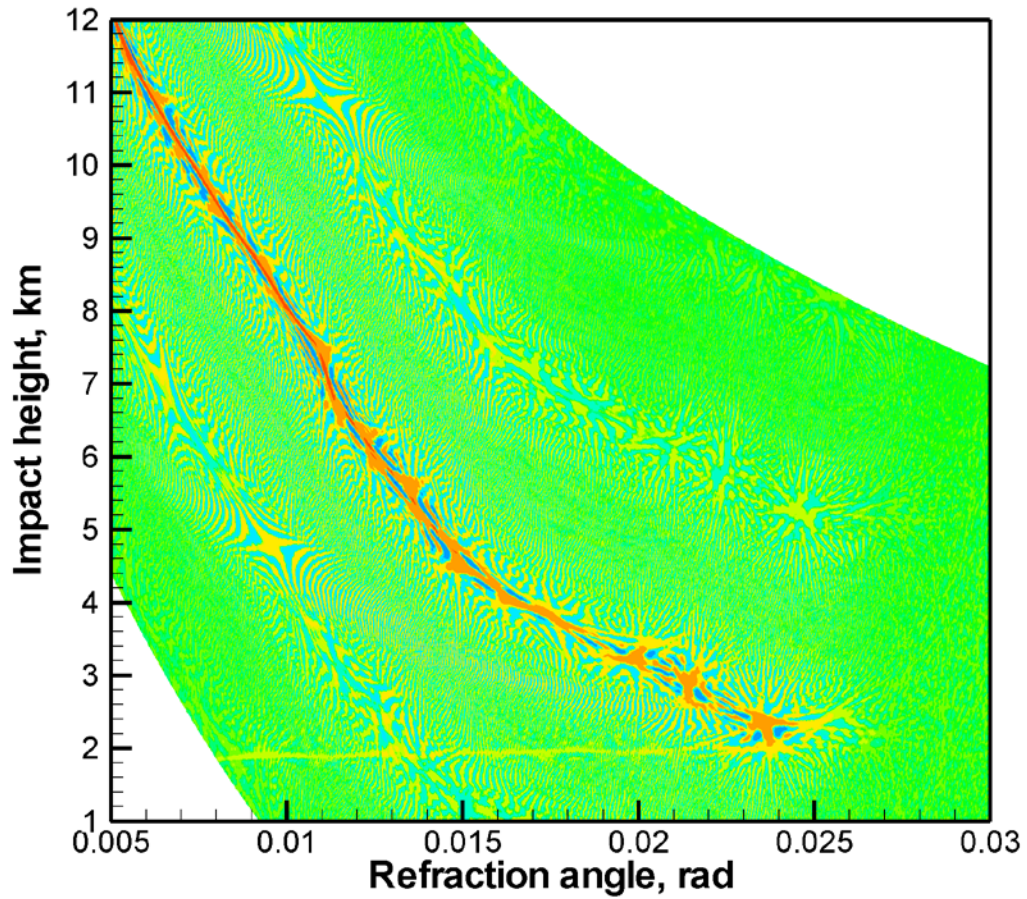
Figure 34. Occultation event with reflection. Reflection index 24.979. Panels from top to bottom: (1) location map, (2) WDF, (3) radio holographic spectrum, and (4) model and retrieved reflected bending angles with radio holographic error estimates.

(1)

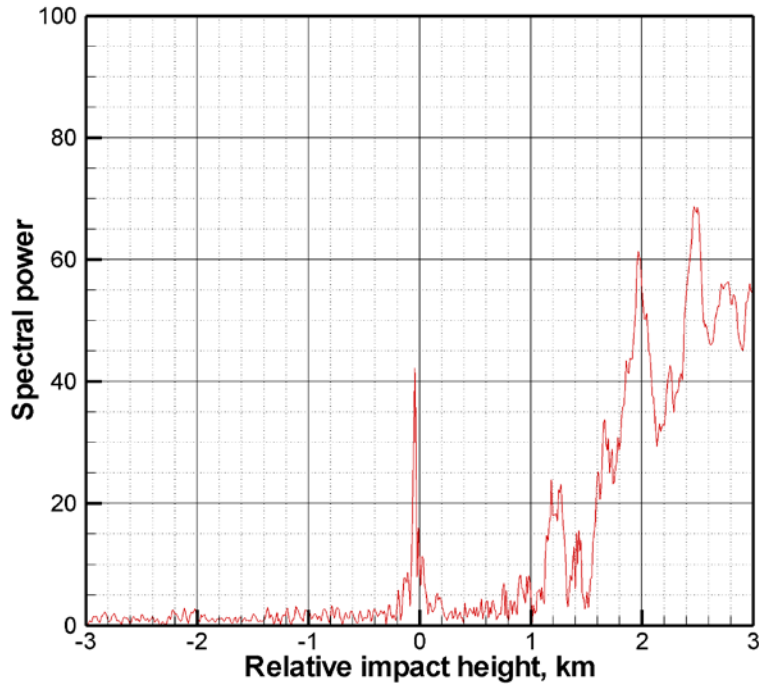
2008/01/01; 08:46:37.000; 61.38S 69.50E; 20.060



(2)



(3)



(4)

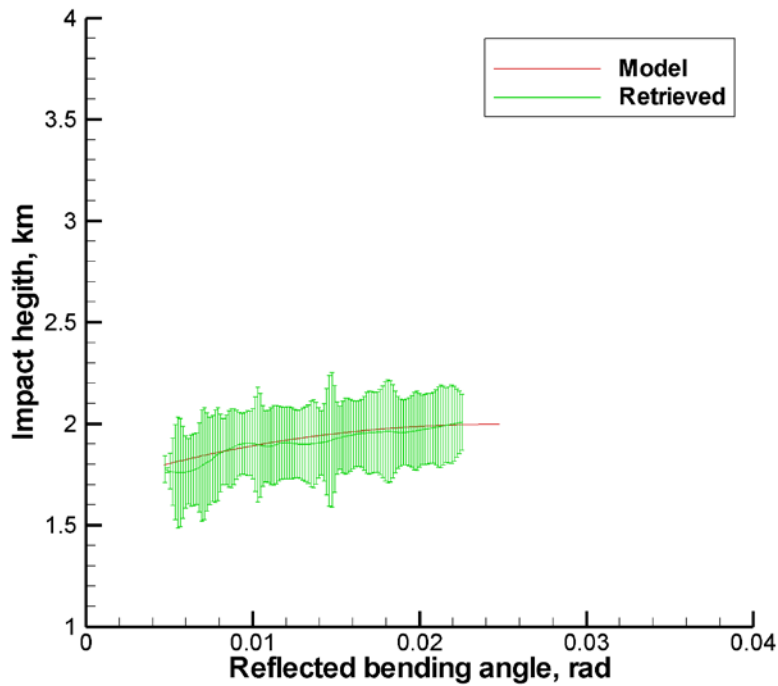
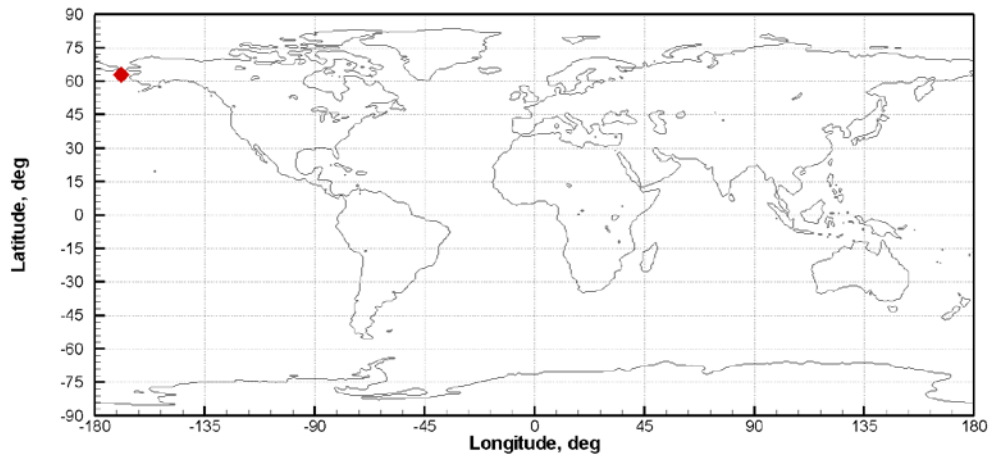


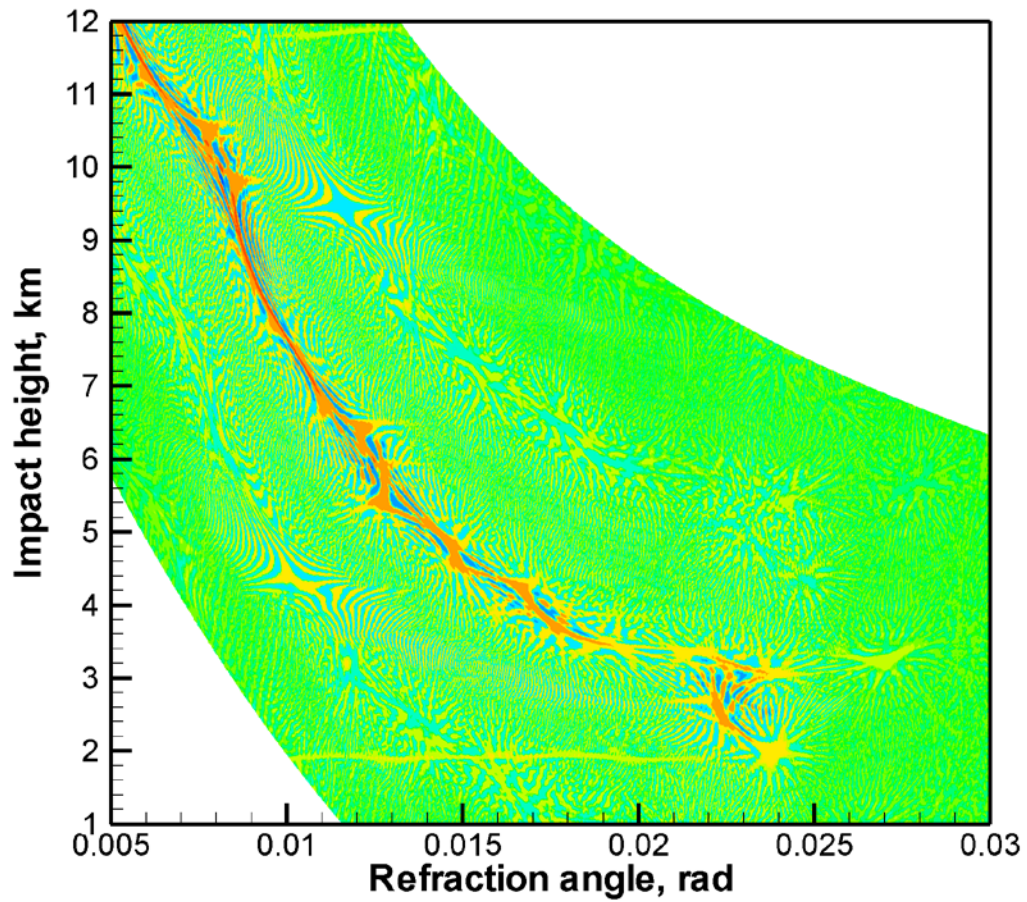
Figure 35. Occultation event with reflection. Reflection index 20.060. Panels from top to bottom: (1) location map, (2) WDF, (3) radio holographic spectrum, and (4) model and retrieved reflected bending angles with radio holographic error estimates.

(1)

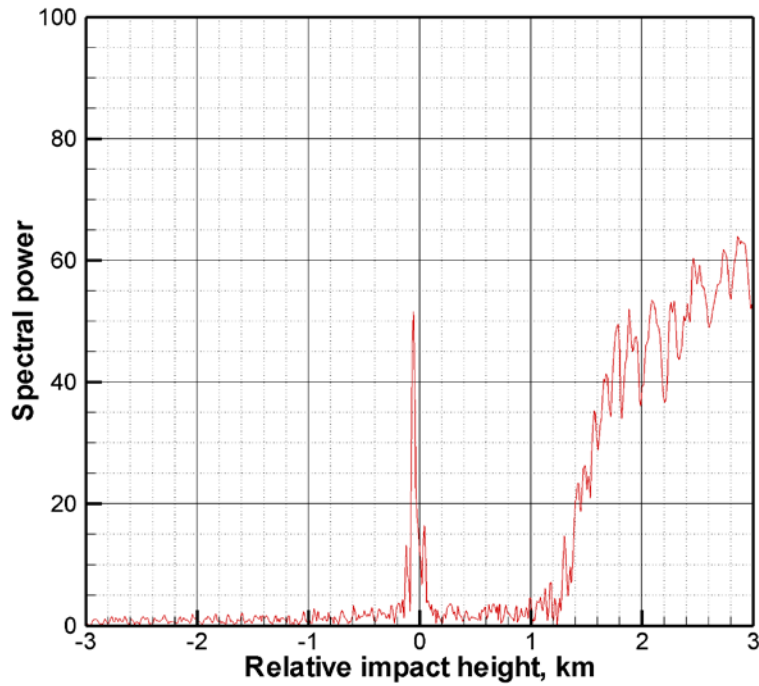
2008/01/01; 20:23:59.000; 62.96N 169.35W; 15.697



(2)



(3)



(4)

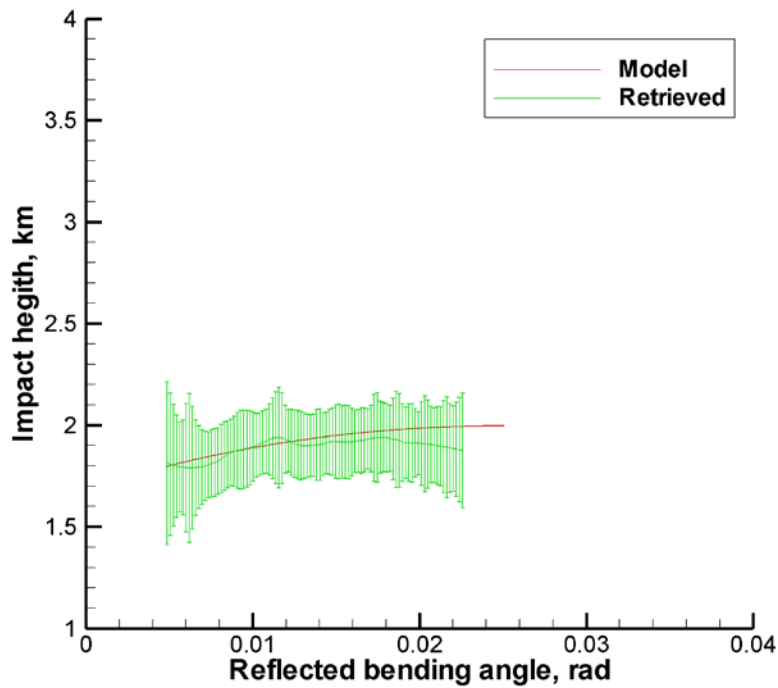
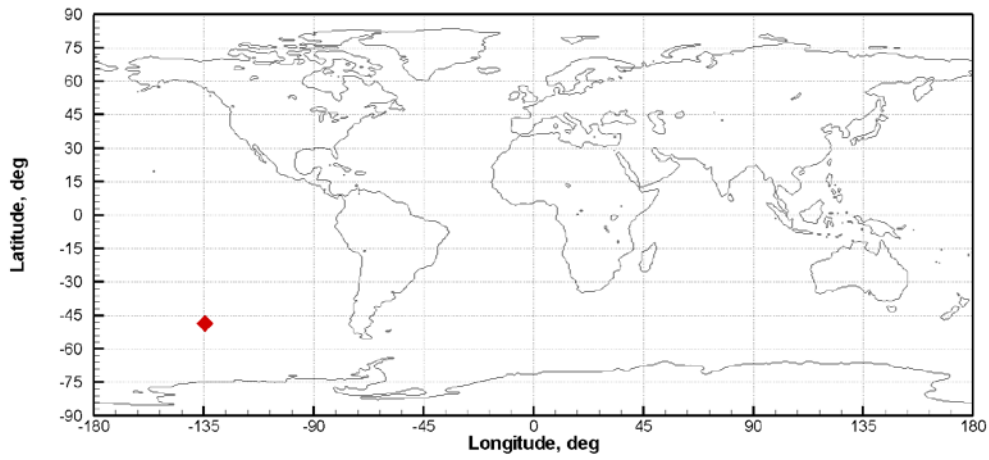


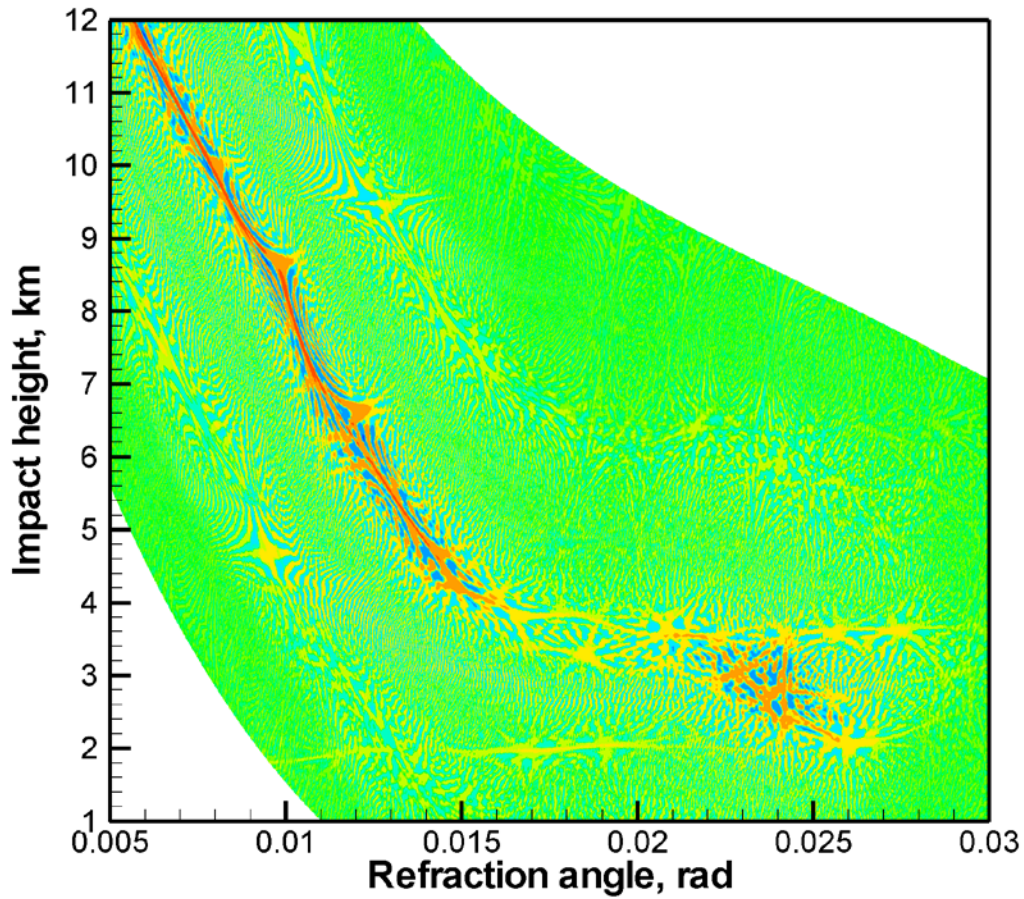
Figure 36. Occultation event with reflection. Reflection index 15.697. Panels from top to bottom: (1) location map, (2) WDF, (3) radio holographic spectrum, and (4) model and retrieved reflected bending angles with radio holographic error estimates.

(1)

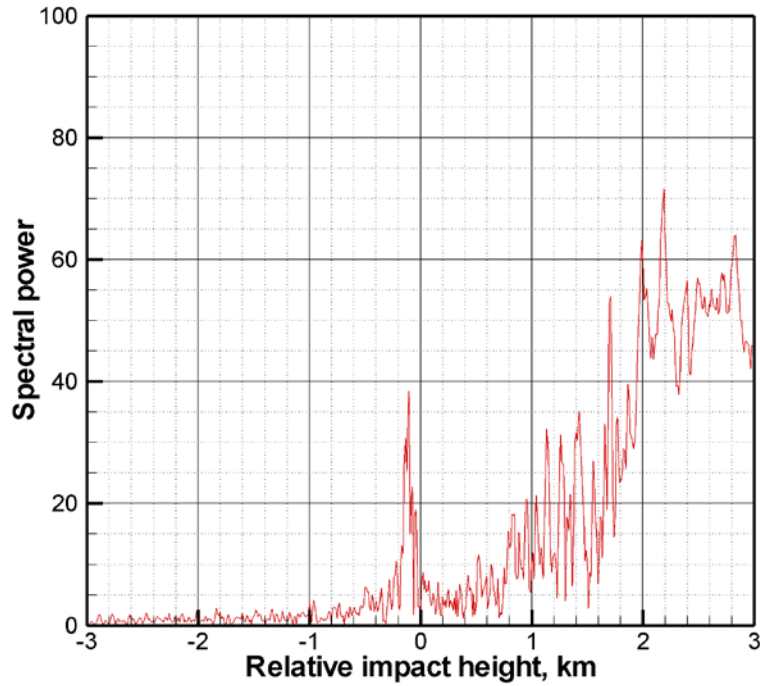
2008/01/01; 10:07:11.000; 48.68S 134.46W; 10.145



(2)



(3)



(4)

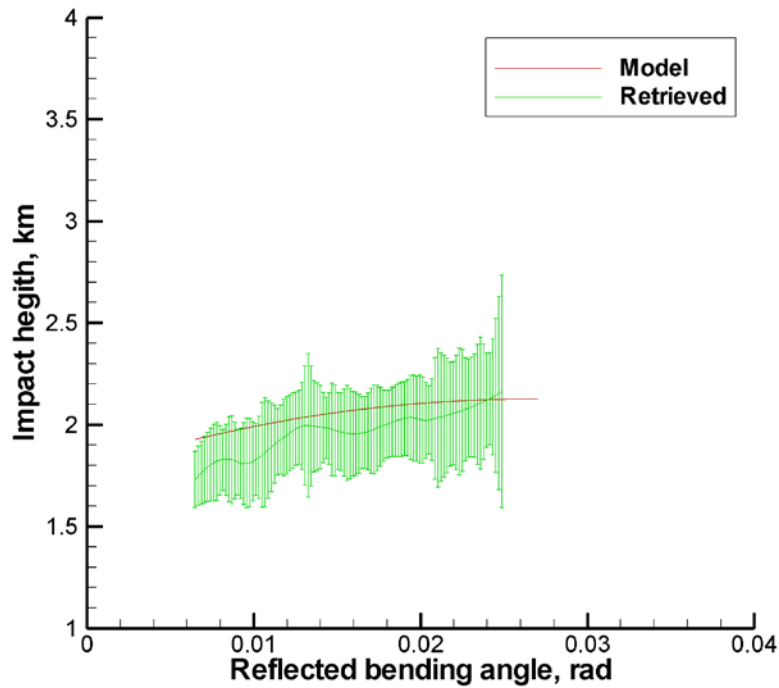
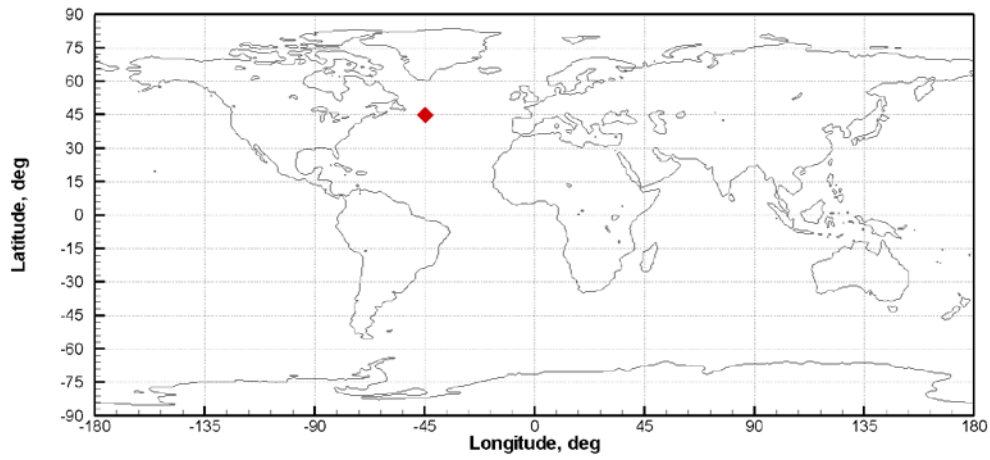


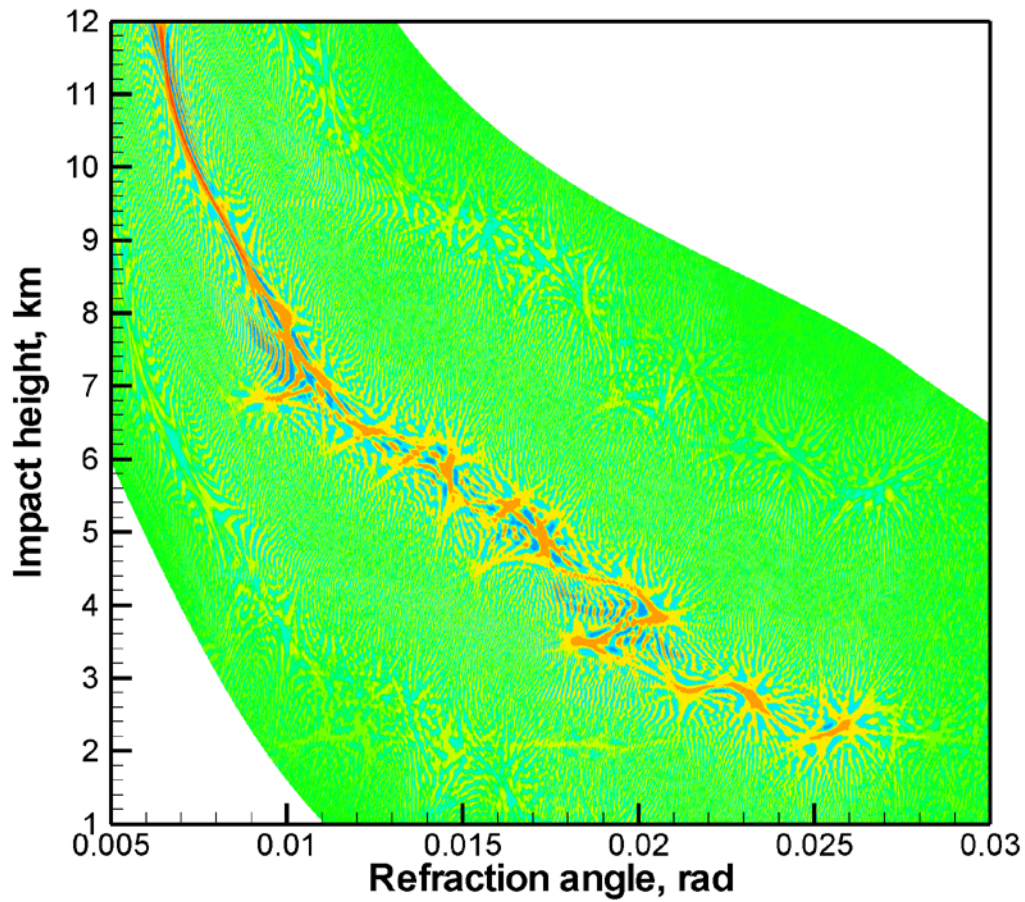
Figure 37. Occultation event with reflection. Reflection index 10.145. Panels from top to bottom: (1) location map, (2) WDF, (3) radio holographic spectrum, and (4) model and retrieved reflected bending angles with radio holographic error estimates.

(1)

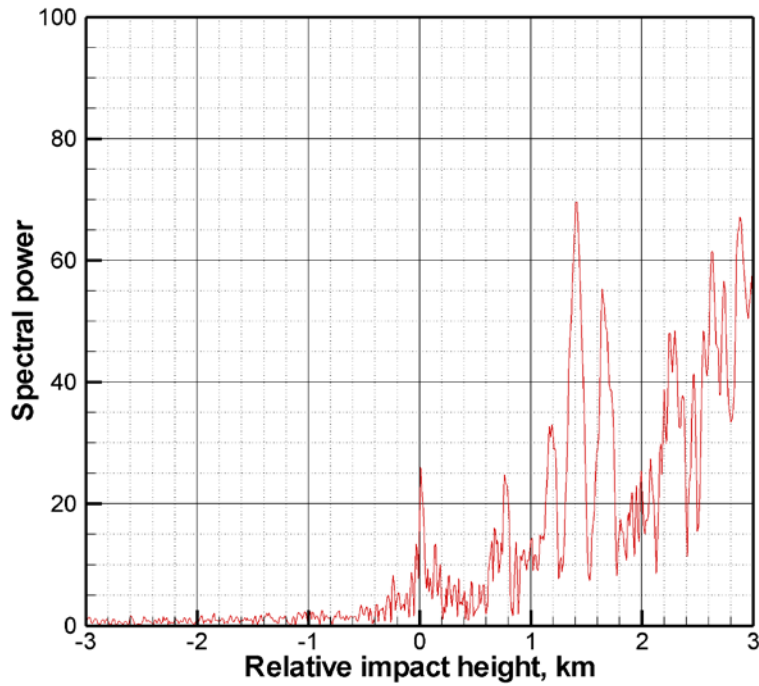
2008/01/01; 04:39:47.000; 44.78N 44.75W; 8.943



(2)



(3)



(4)

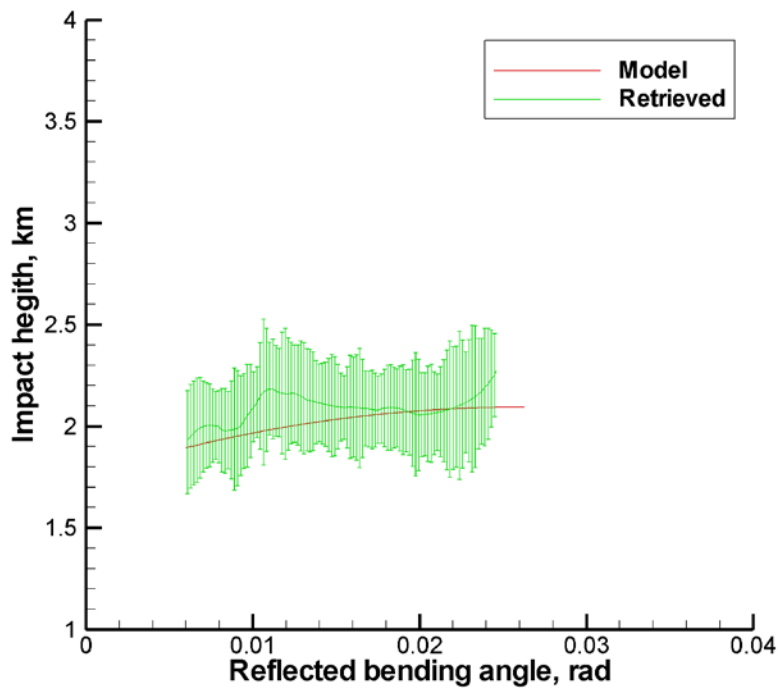
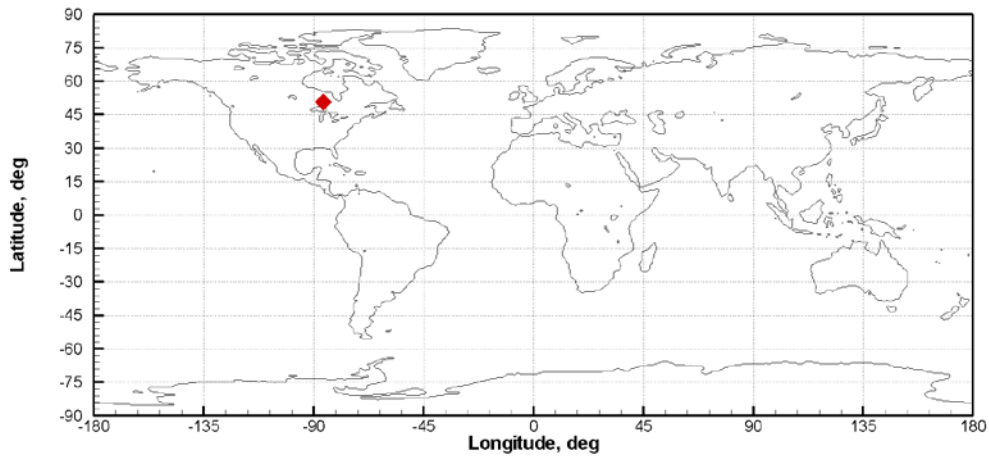


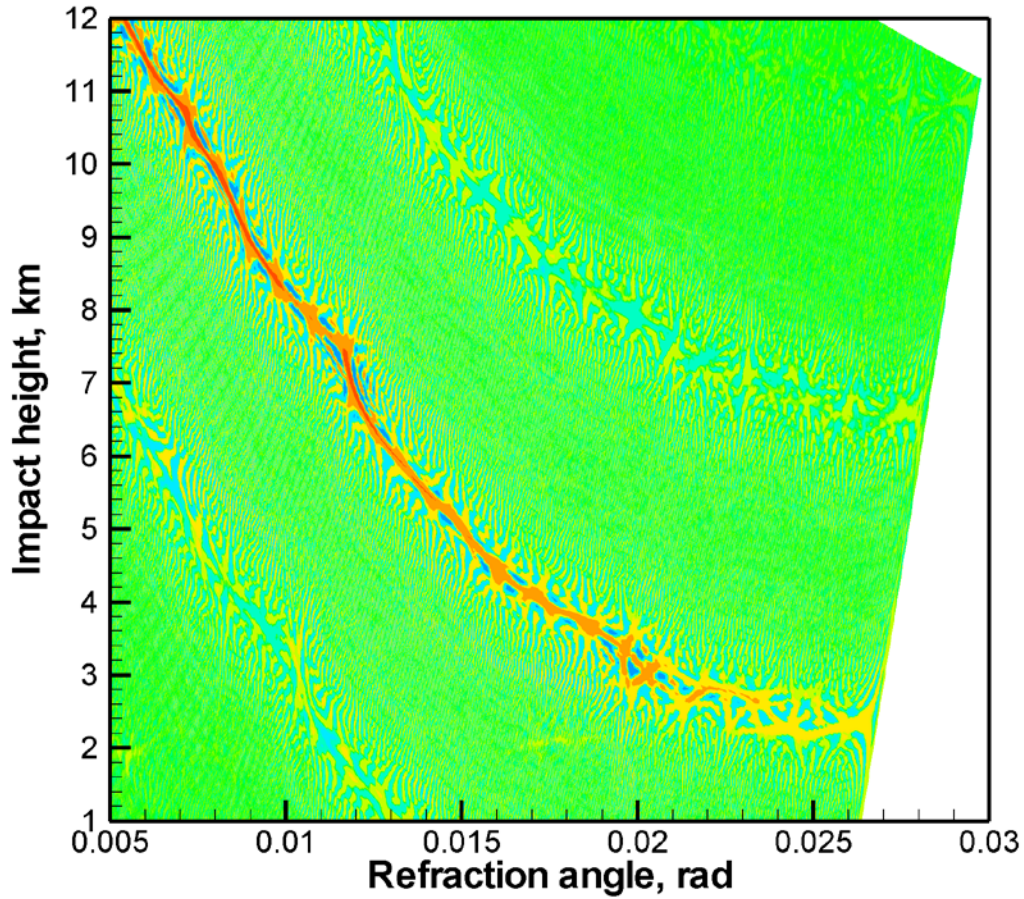
Figure 38. Occultation event with reflection. Reflection index 8.943. Panels from top to bottom: (1) location map, (2) WDF, (3) radio holographic spectrum, and (4) model and retrieved reflected bending angles with radio holographic error estimates.

(1)

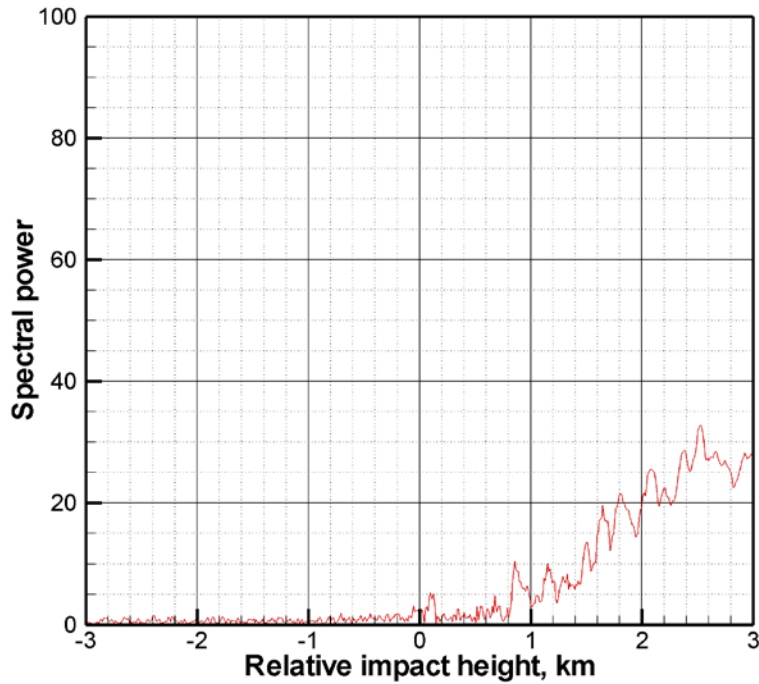
2008/01/01; 01:01:50.000; 50.66N 86.02W; 6.495



(2)



(3)



(4)

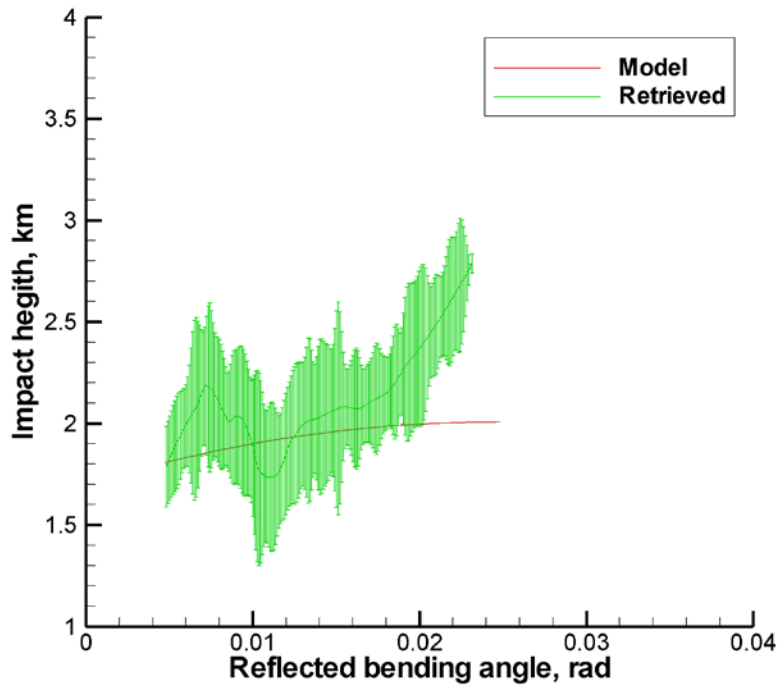
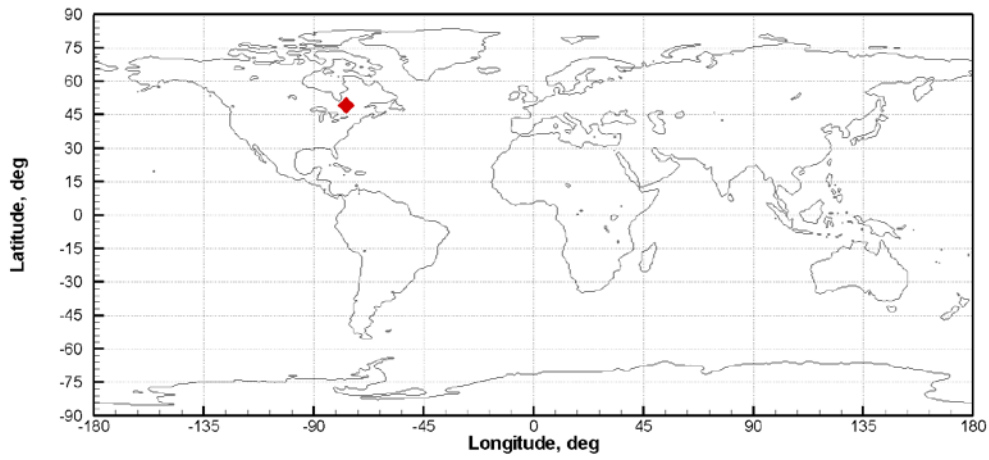


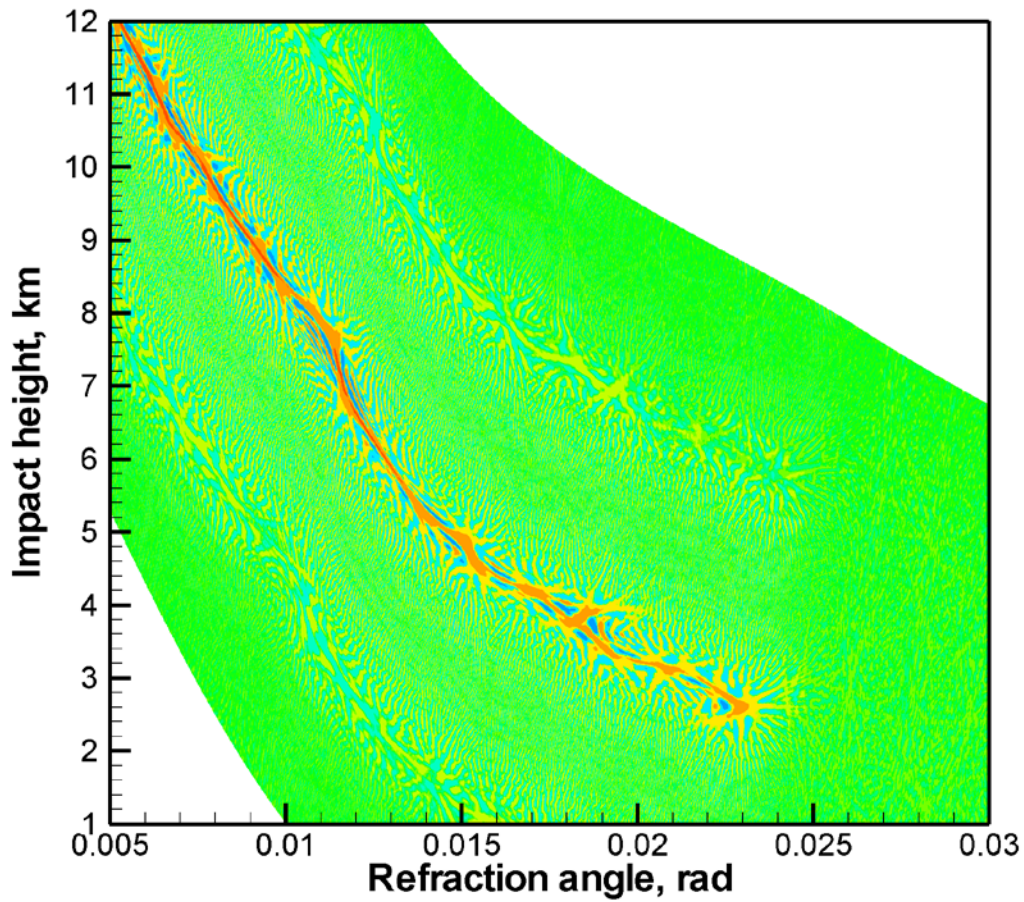
Figure 39. Occultation event with unlikely reflection. Reflection index 6.495. Panels from top to bottom: (1) location map, (2) WDF, (3) radio holographic spectrum, and (4) model and retrieved reflected bending angles with radio holographic error estimates.

(1)

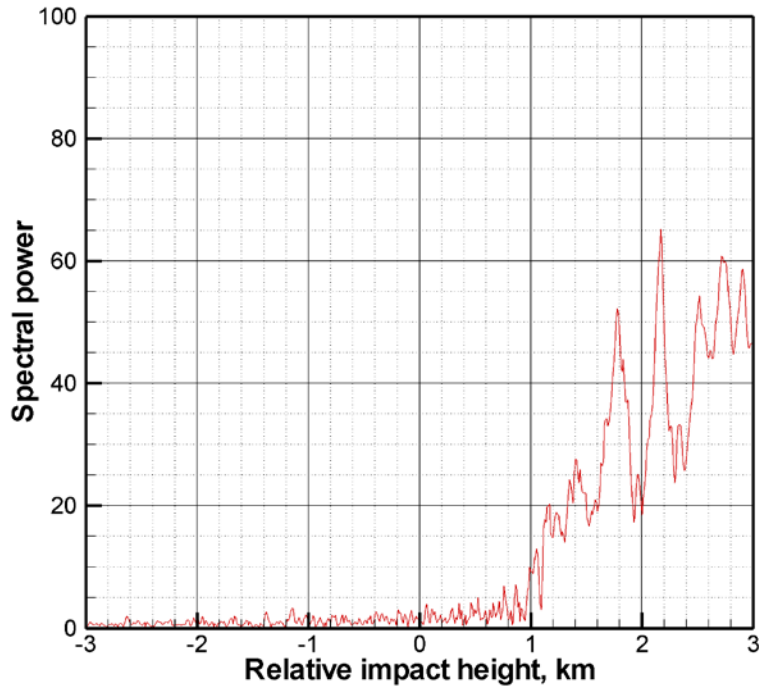
2008/01/01; 02:51:36.000; 49.16N 76.55W; 4.356



(2)



(3)



(4)

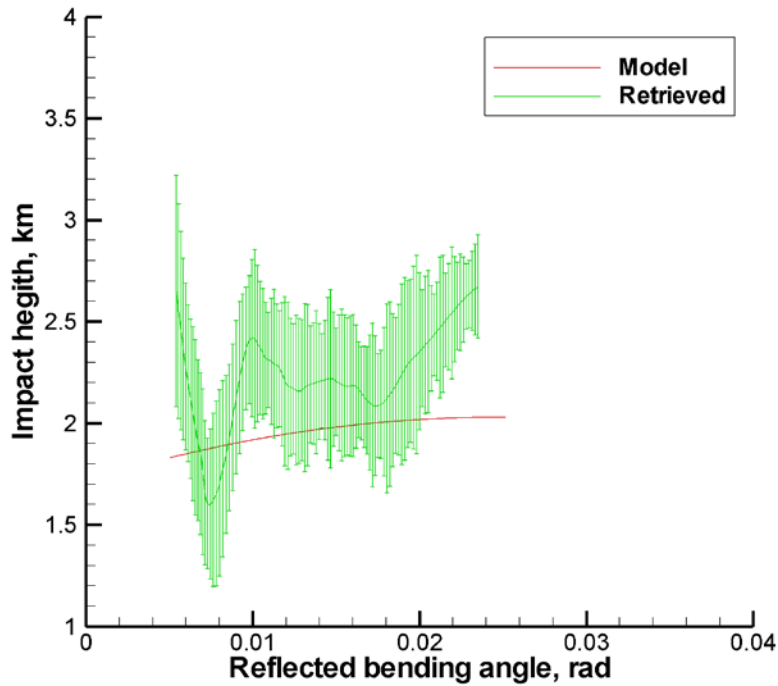
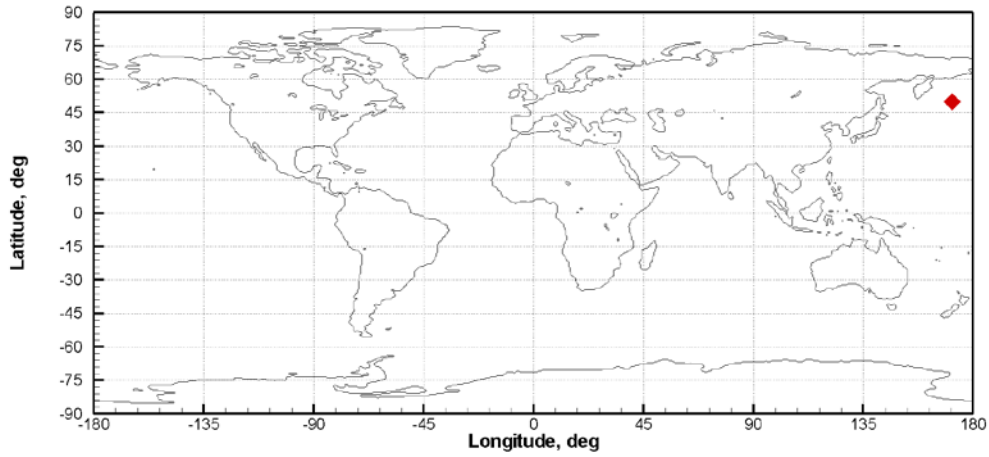


Figure 40. Occultation event without reflection. Reflection index 4.356. Panels from top to bottom: (1) location map, (2) WDF, (3) radio holographic spectrum, and (4) model and retrieved reflected bending angles with radio holographic error estimates.

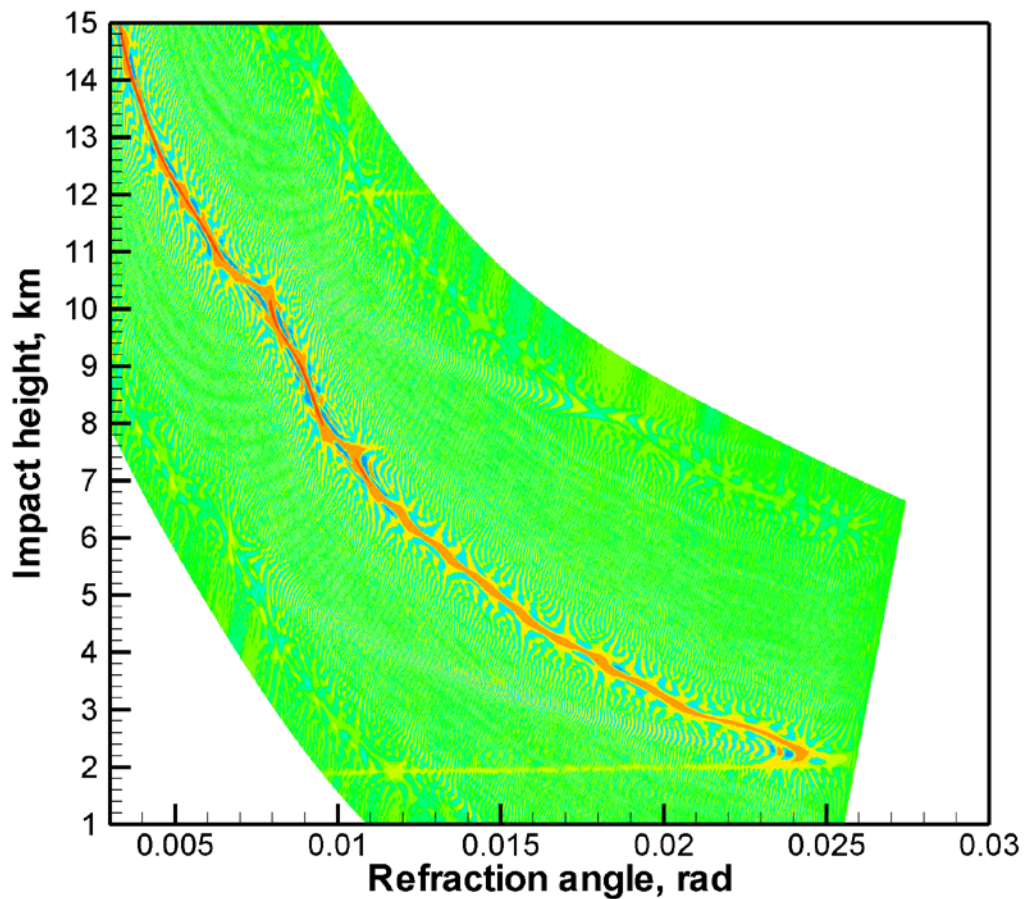
6. Examples of Processing METOP data

(1)

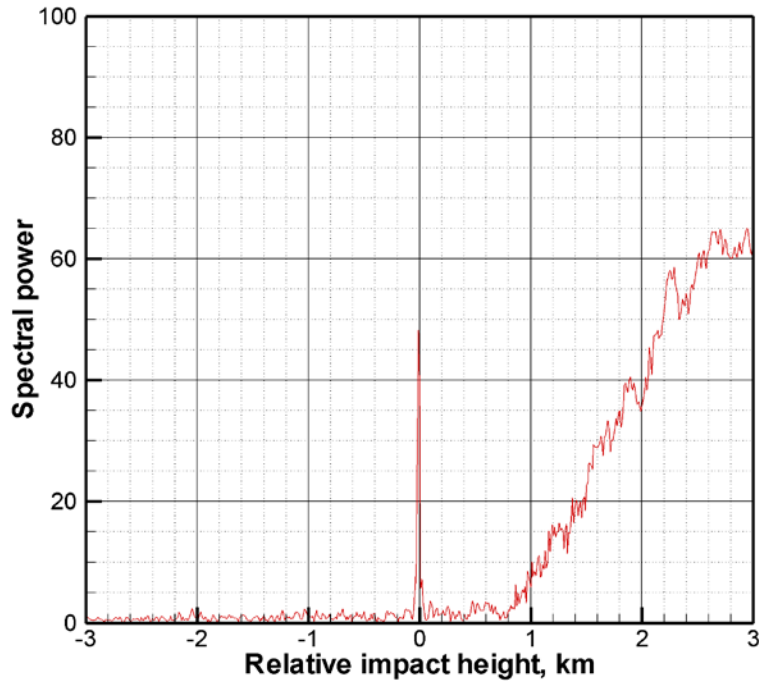
2014/03/05; 09:16:08.000; 50.11N 171.43E; 28.014



(2)



(3)



(4)

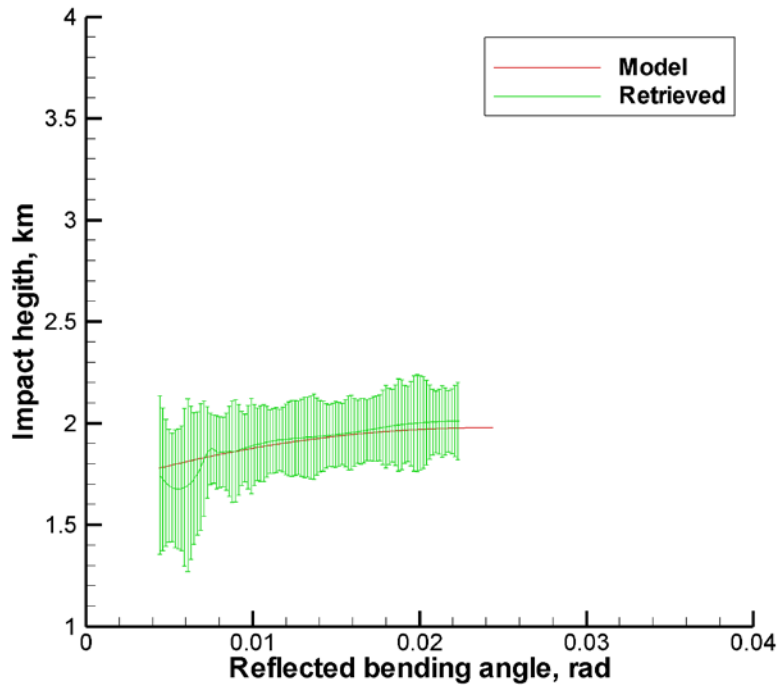
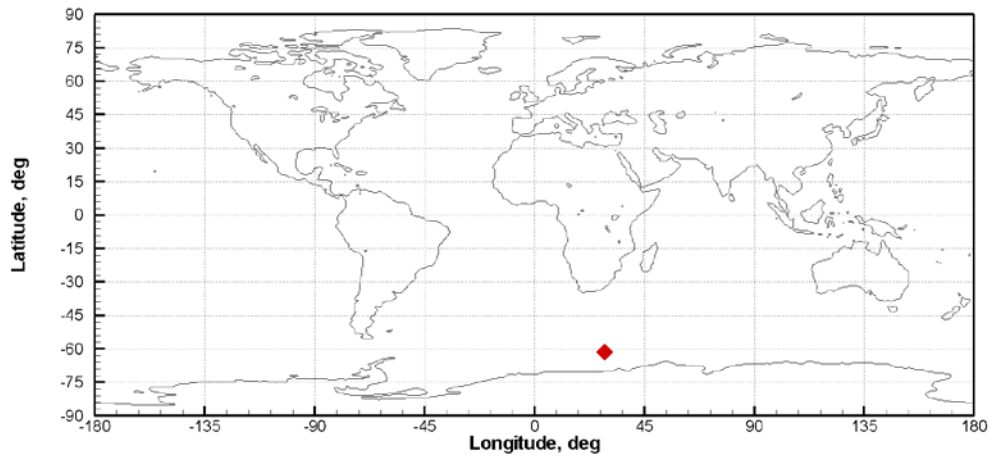


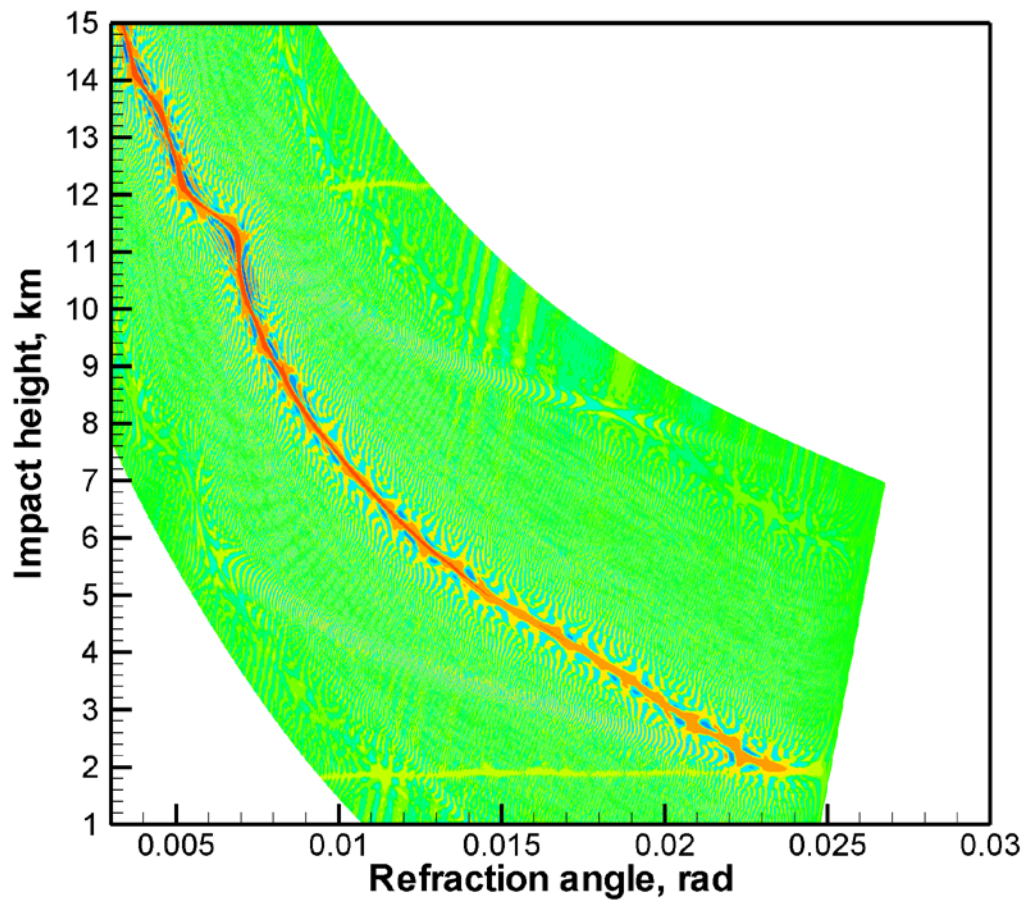
Figure 41. Occultation event with reflection. Reflection index 28.014. Panels from top to bottom: (1) location map, (2) WDF, (3) radio holographic spectrum, and (4) model and retrieved reflected bending angles with radio holographic error estimates.

(1)

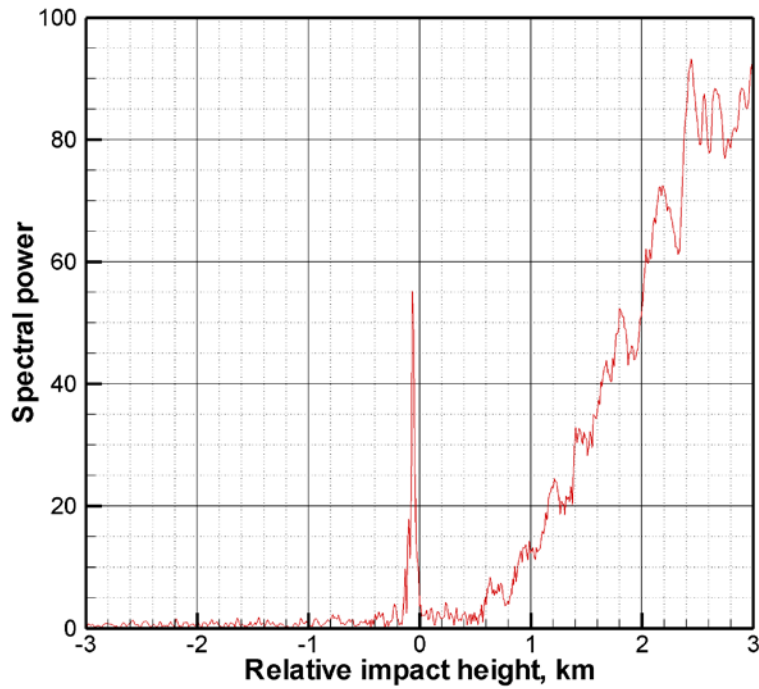
2014/03/05; 00:10:53.000; 61.43S 28.70E; 20.388



(2)



(3)



(4)

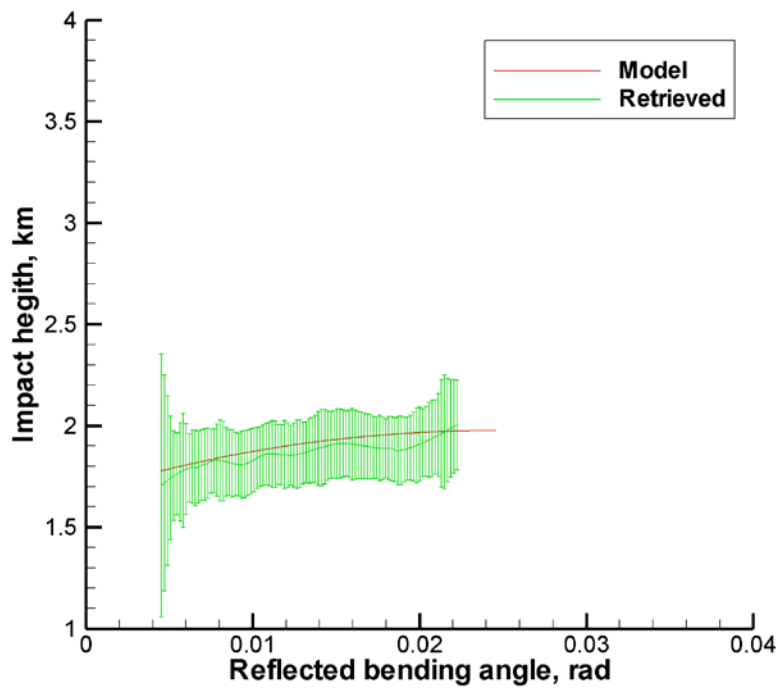
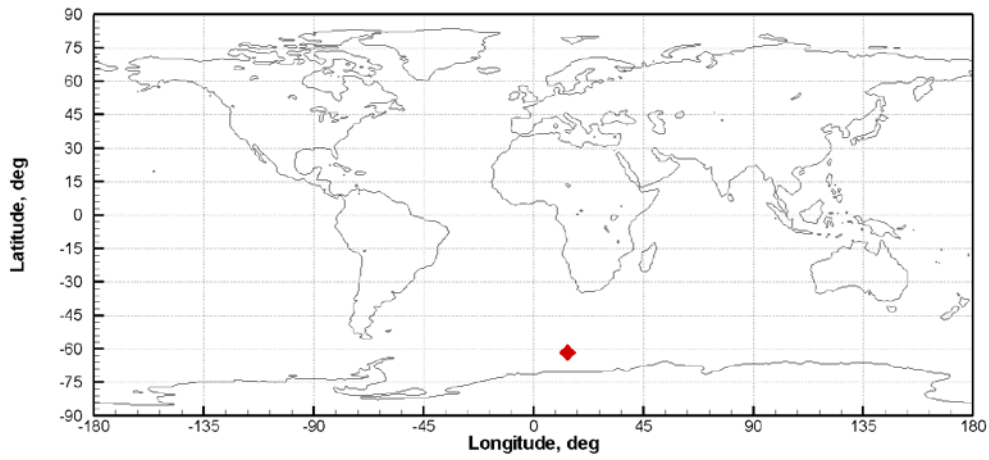


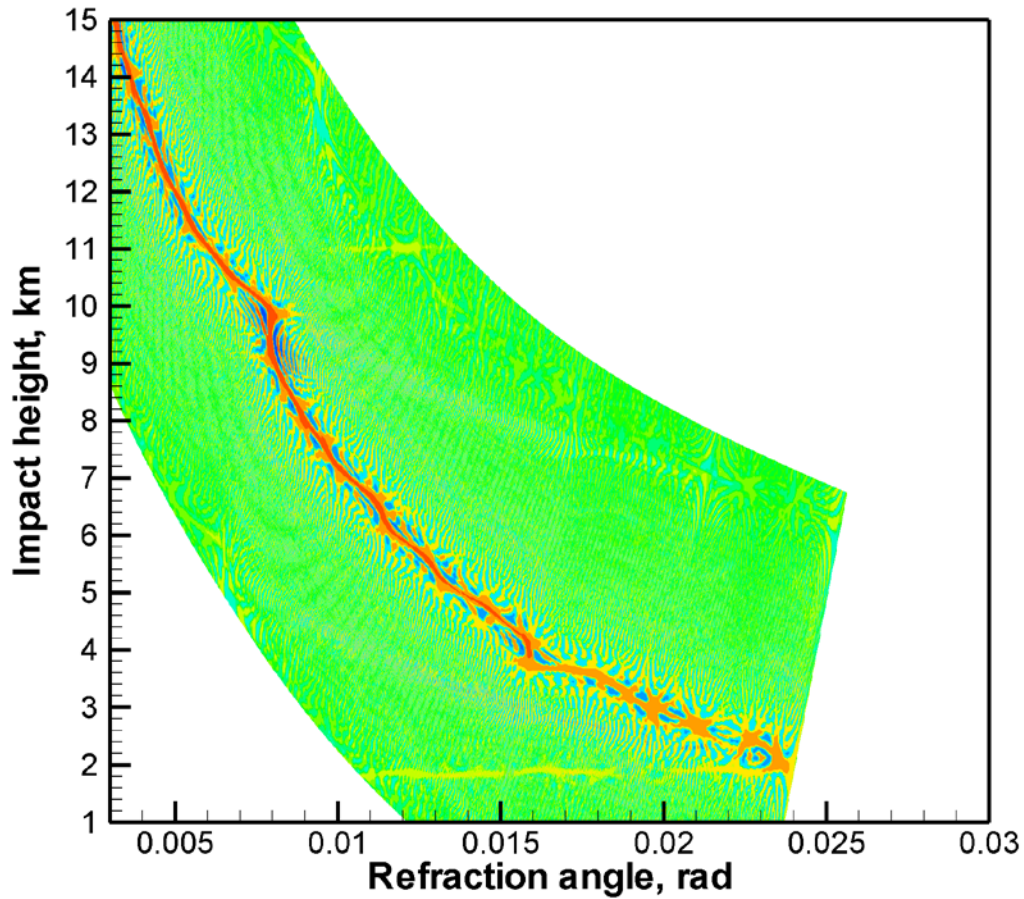
Figure 42. Occultation event with reflection. Reflection index 20.388. Panels from top to bottom: (1) location map, (2) WDF, (3) radio holographic spectrum, and (4) model and retrieved reflected bending angles with radio holographic error estimates.

(1)

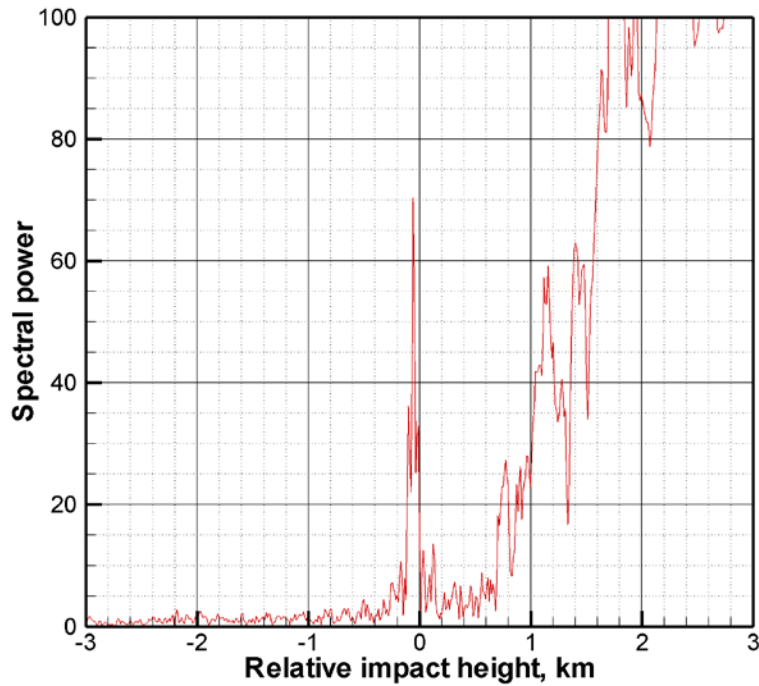
2014/03/05; 04:54:36.000; 61.89S 13.81E; 15.020



(2)



(3)



(3)

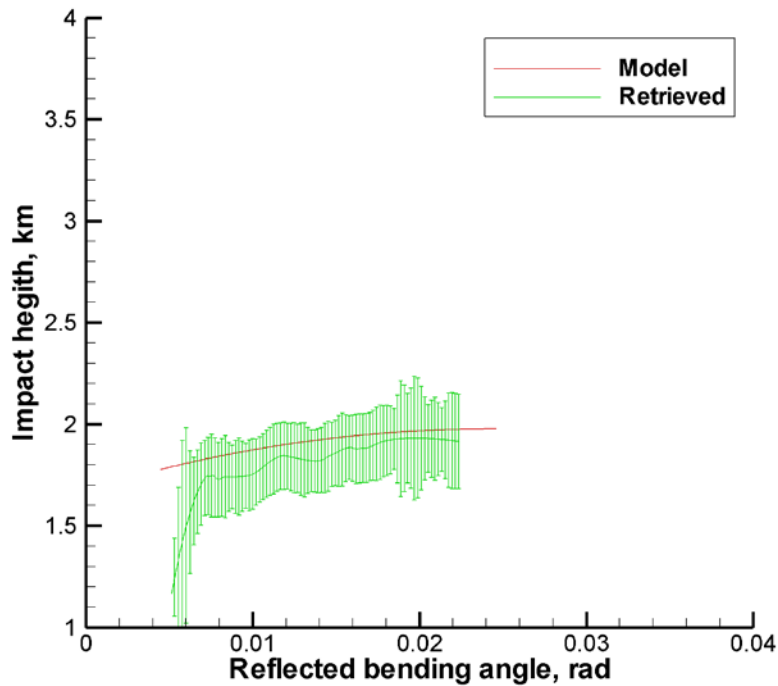
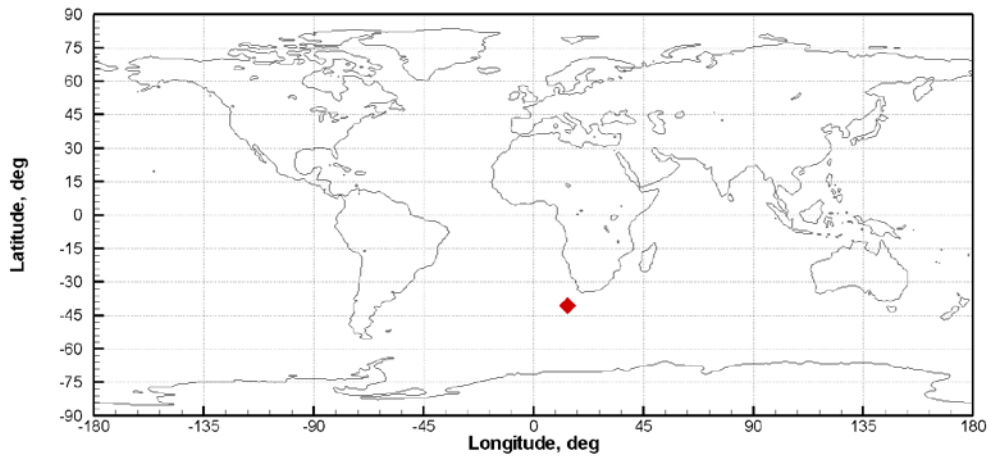


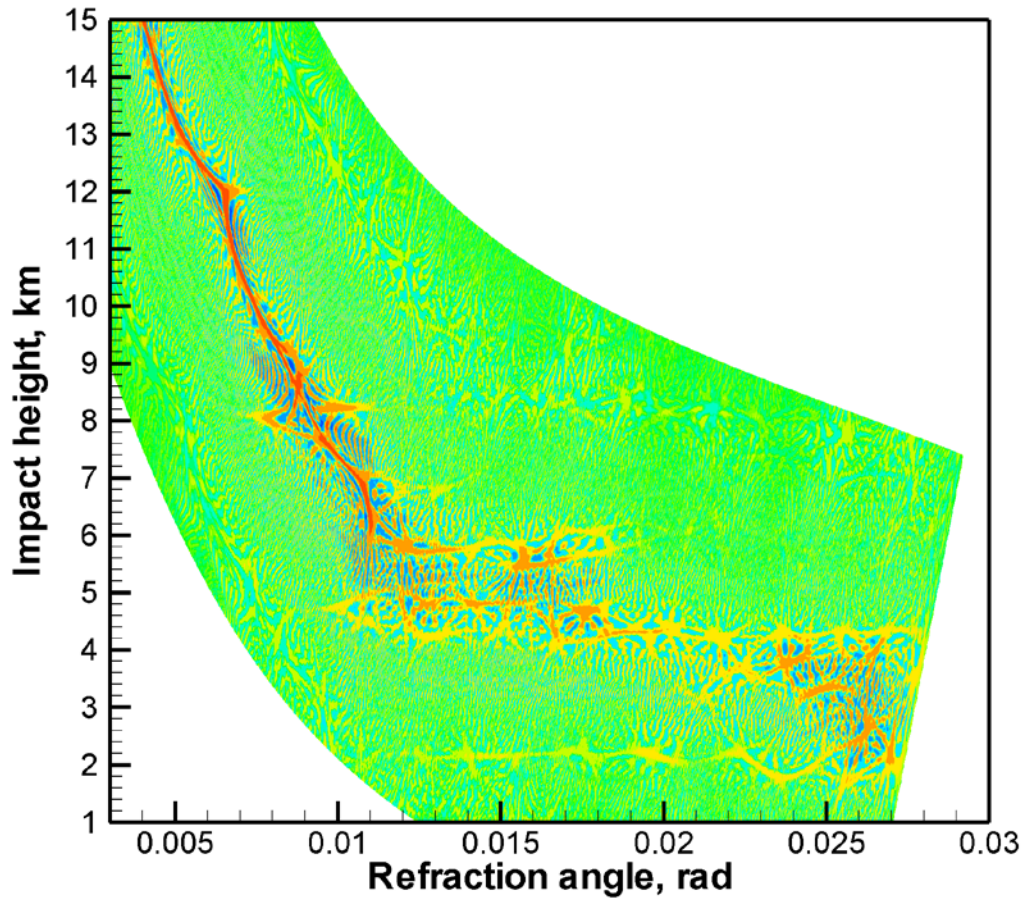
Figure 43. Occultation event with reflection. Reflection index 15.020. Panels from top to bottom: (1) location map, (2) WDF, (3) radio holographic spectrum, and (4) model and retrieved reflected bending angles with radio holographic error estimates.

(1)

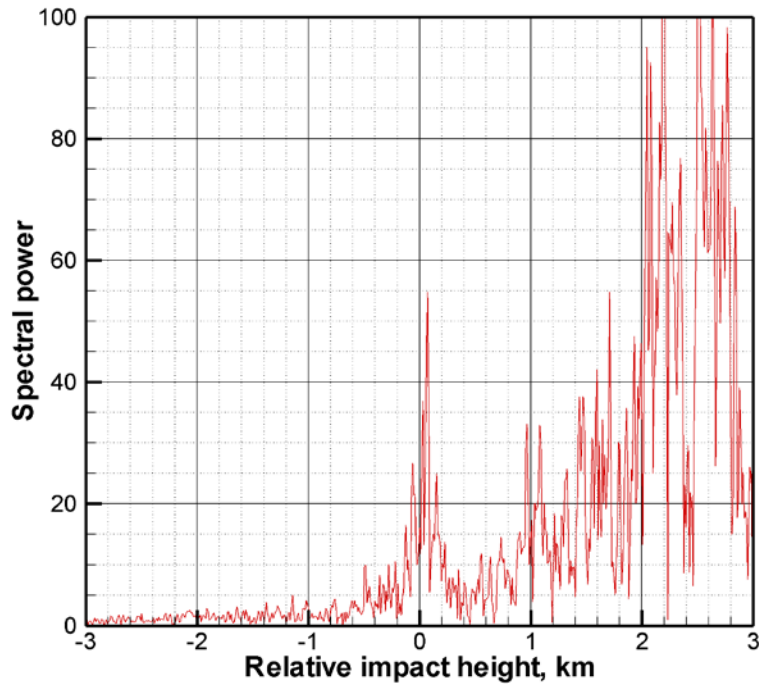
2014/03/05; 06:28:55.000; 40.76S 13.84E; 10.579



(2)



(3)



(4)

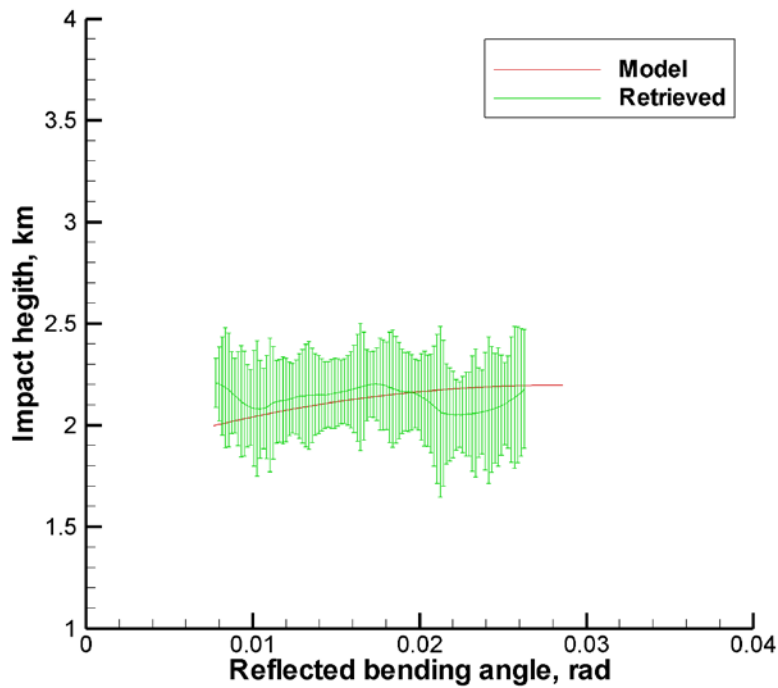
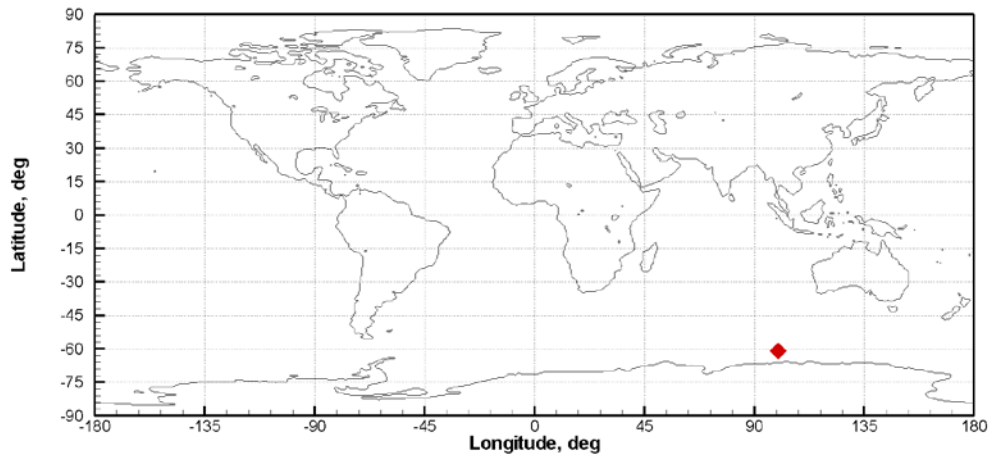


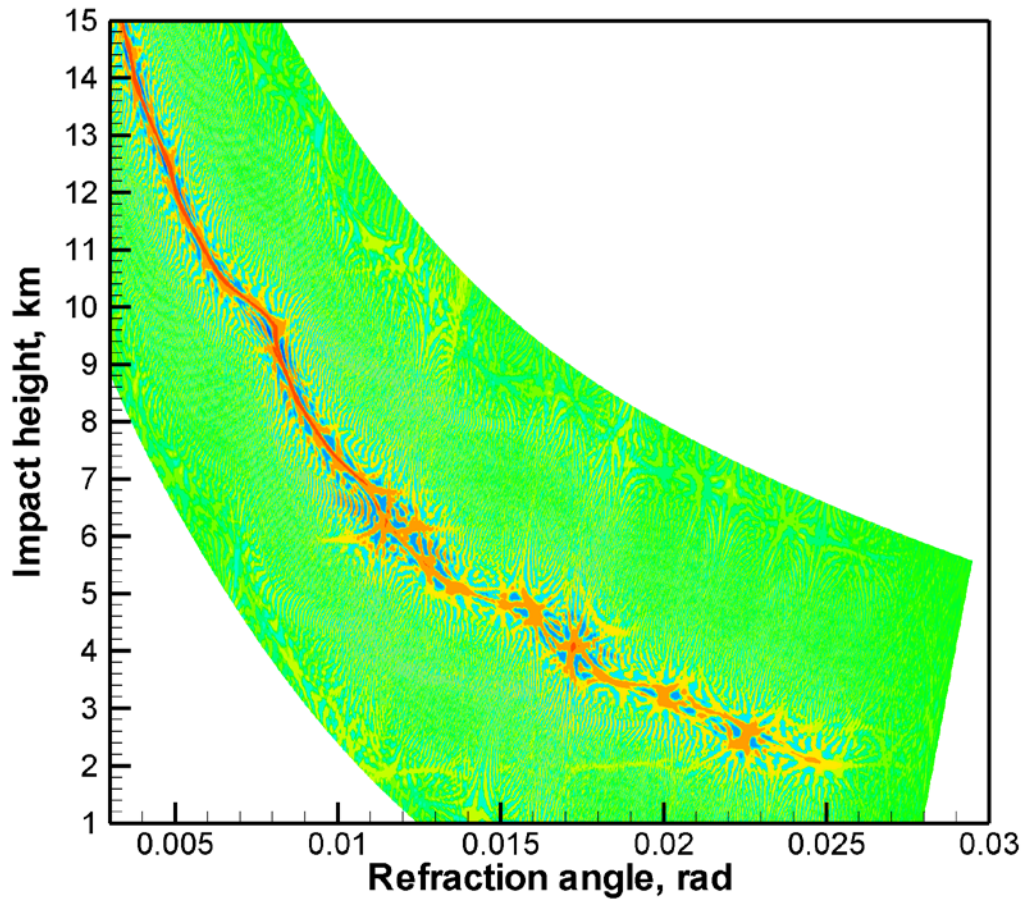
Figure 44. Occultation event with reflection. Reflection index 10.579. Panels from top to bottom: (1) location map, (2) WDF, (3) radio holographic spectrum, and (4) model and retrieved reflected bending angles with radio holographic error estimates.

(1)

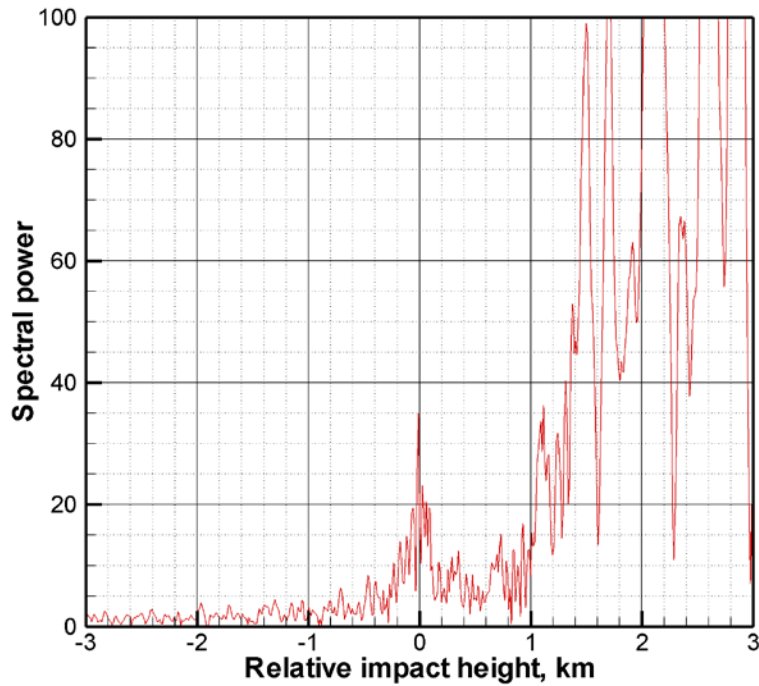
2014/03/05; 00:03:08.000; 61.00S 99.63E; 7.350



(2)



(3)



(4)

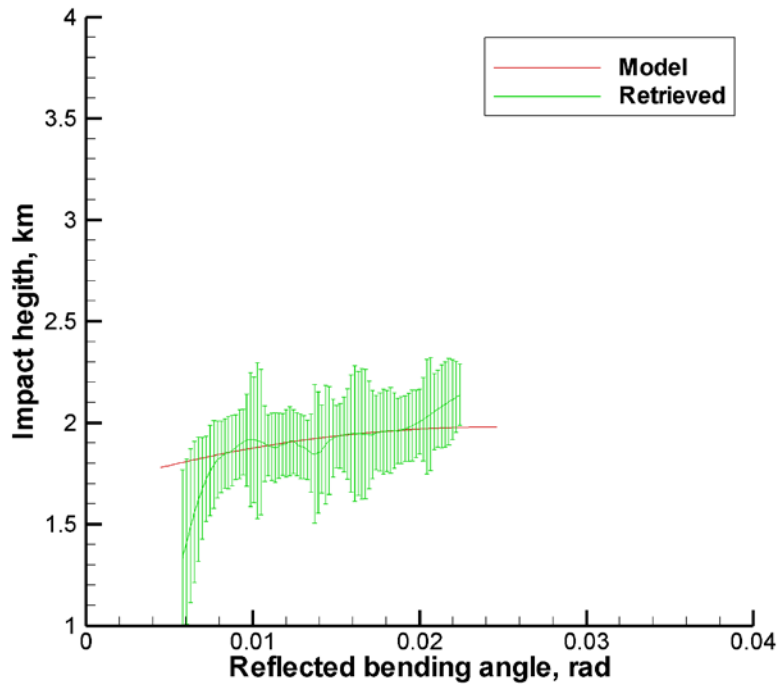
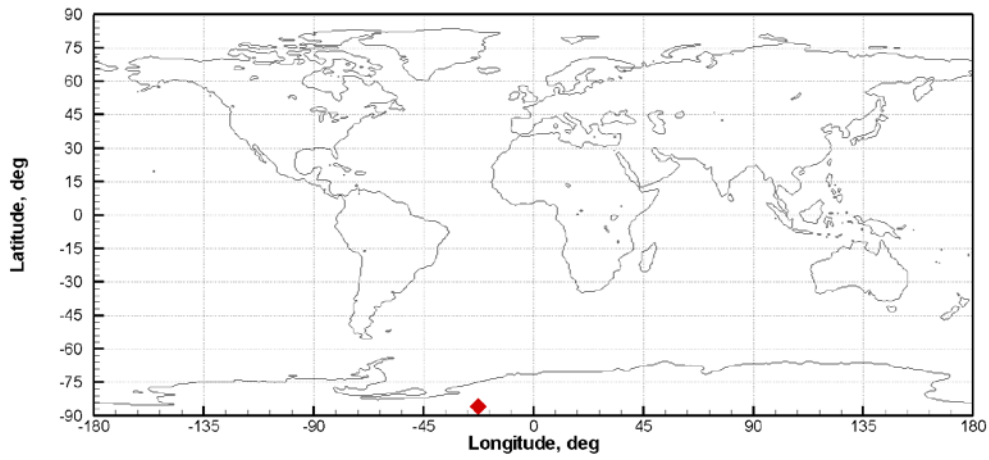


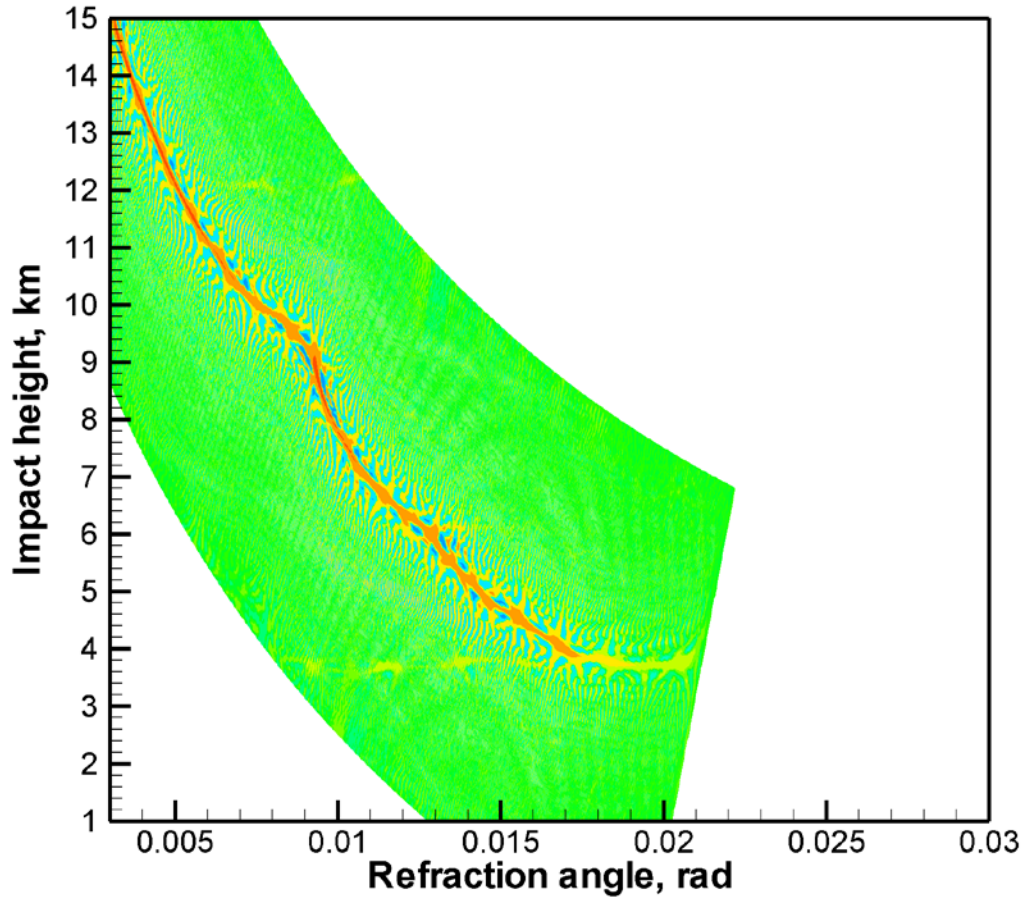
Figure 45. Occultation event with likely reflection. Reflection index 7.350. Panels from top to bottom: (1) location map, (2) WDF, (3) radio holographic spectrum, and (4) model and retrieved reflected bending angles with radio holographic error estimates.

(1)

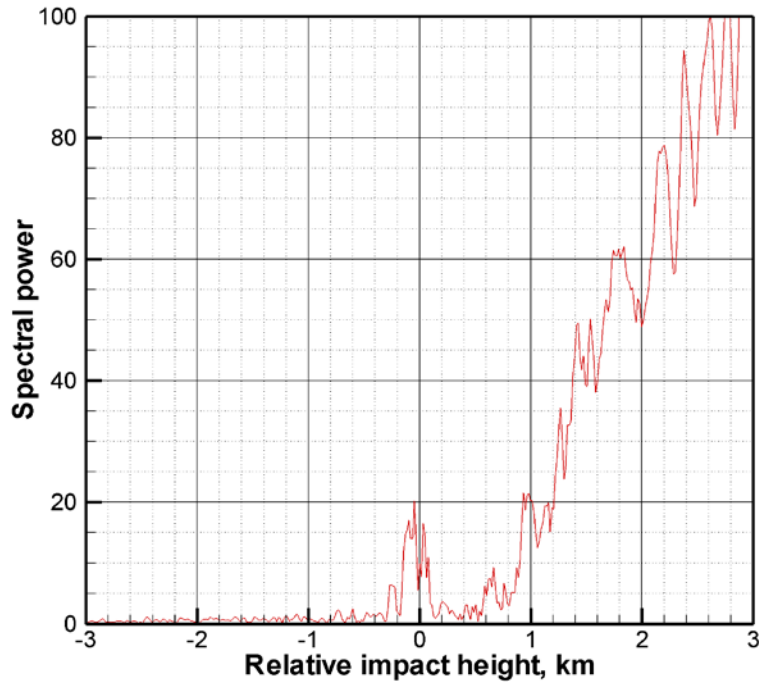
2014/03/05; 01:51:56.000; 86.03S 22.80W; 5.029



(2)



(3)



(4)

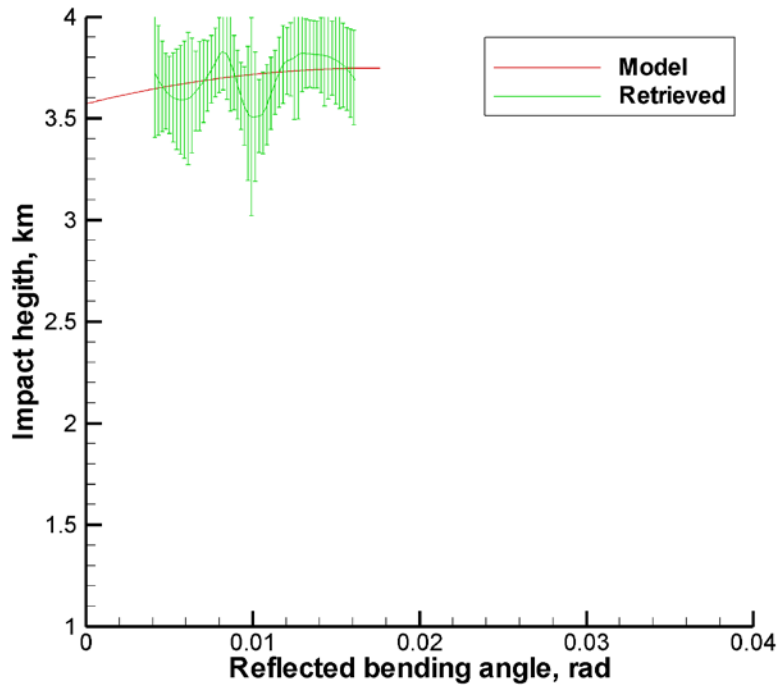
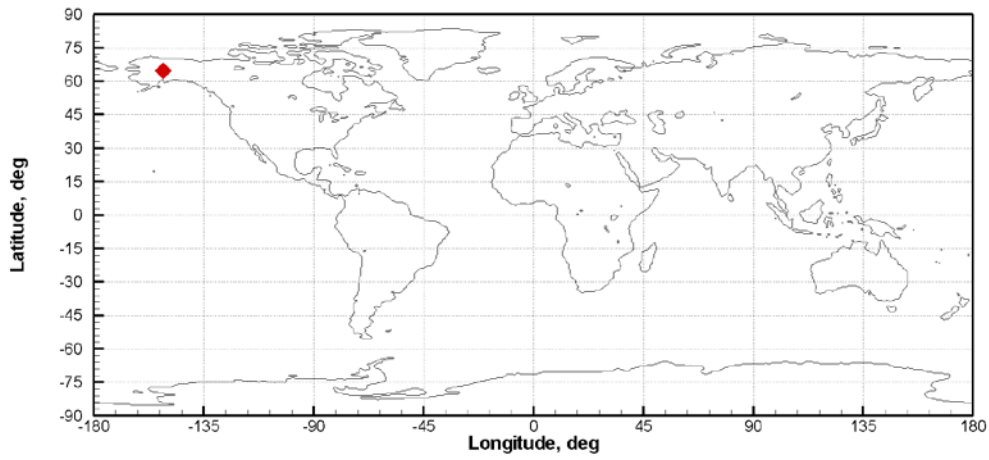


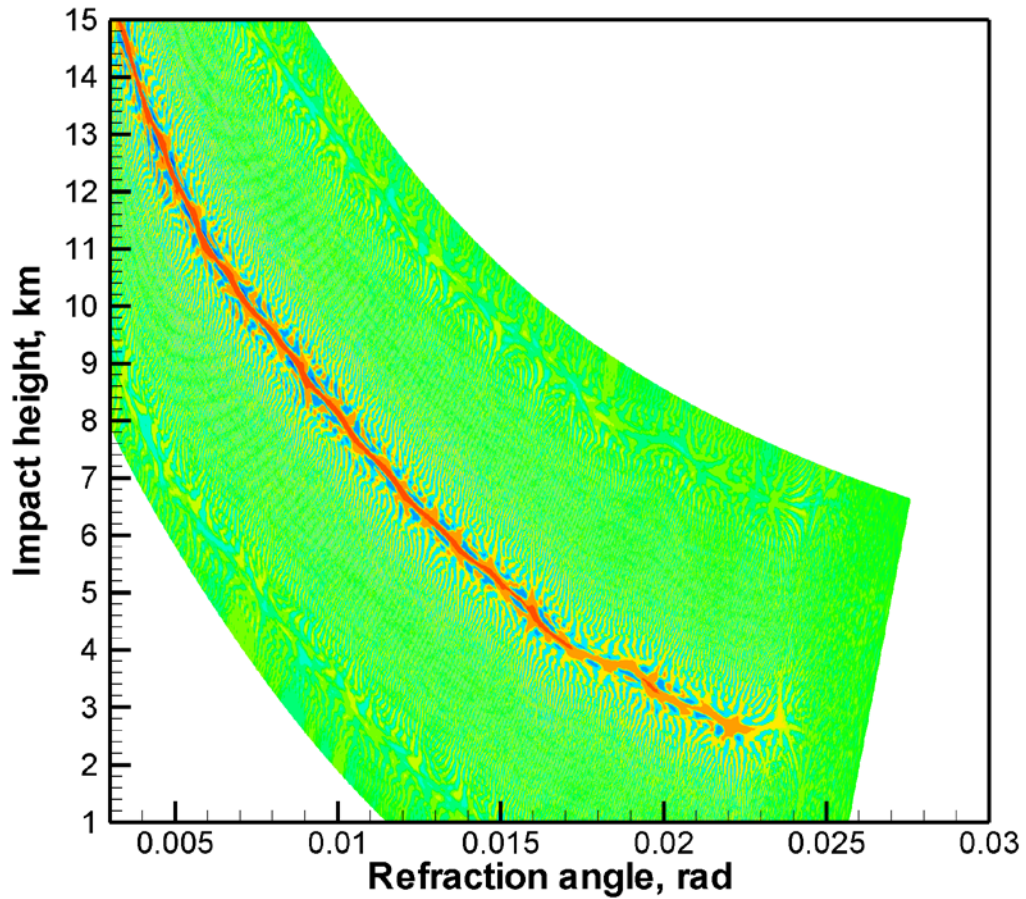
Figure 46. Occultation event with likely reflection. Reflection index 5.029. Panels from top to bottom: (1) location map, (2) WDF, (3) radio holographic spectrum, and (4) model and retrieved reflected bending angles with radio holographic error estimates.

(1)

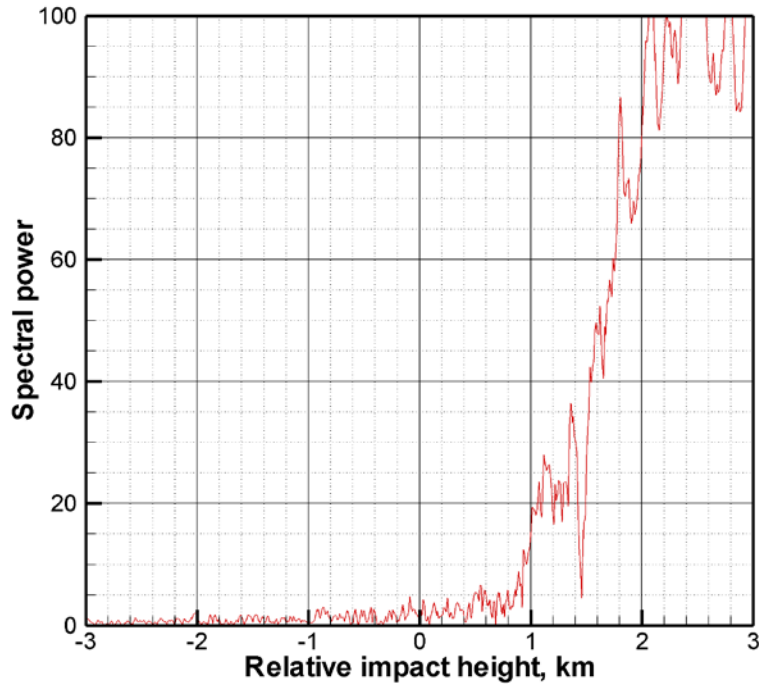
2014/03/05; 01:00:00.000; 64.57N 151.59W; 4.015



(2)



(3)



(4)

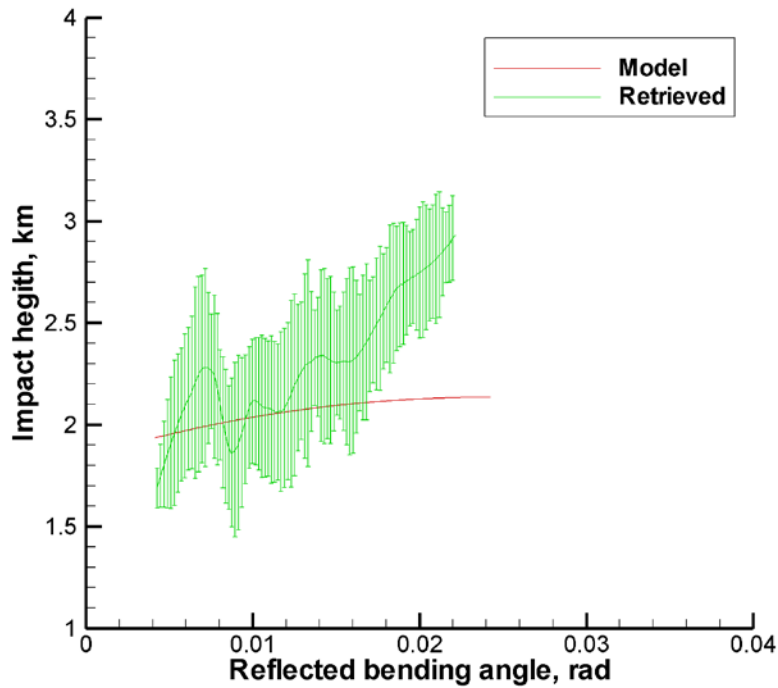


Figure 47. Occultation event without reflection. Reflection index 4.015. Panels from top to bottom: (1) location map, (2) WDF, (3) radio holographic spectrum, and (4) model and retrieved reflected bending angles with radio holographic error estimates.

7. Comparison with the ROM SAF Database

In this Chapter, we present a comparison of our retrievals with the ROM SAF database. The database contains occultation events classified into three categories: 1) no reflection, 2) reflection, and 3) unclear. The events are accompanied by the SVM (Supporting Vector Machine) index [5, 6] based on the radio holographic analysis and supervised learning method.

Here, we use a modified definition of the reflection index. The radio holographic spectrum is defined as follows:

$$\tilde{u}_R(\omega) = \int A(t) \exp\left(ik \left[S(t) - \overline{S}_R(t) - \omega \right]\right) dt. \quad (49)$$

Here, unlike the previous definition (42), we use the smoothed reflected signal phase excess $\overline{S}_R(t)$ rather than the model $S_{MR}(t)$. This modification makes the radio holographic spectrum sharper, while its maximum is located closer to the zero frequency.

$$\begin{aligned} \tilde{u}_{\max} &= \max_{[-0.1, 0.1]} |\tilde{u}(\Delta p)|^2, \\ \tilde{u}_{\text{ave}} &= \left\langle |\tilde{u}(\Delta p)|^2 \right\rangle_{[p_{\max} - 0.3, p_{\max} + 0.3]}, \\ \tilde{u}_{\text{bkg}} &= \left\langle |\tilde{u}(\Delta p)|^2 \right\rangle_{[1.0, 2.0]}, \\ I'_R &= \frac{\tilde{u}_{\max}^2}{\tilde{u}_{\text{ave}} (\tilde{u}_{\max} + \alpha \tilde{u}_{\text{bkg}})} \left\langle \exp \left(- \left[\frac{p(t) - p_M(t)}{2\delta p(t)} \right]^2 \right) \right\rangle, \end{aligned} \quad (50)$$

where p_{\max} is the location of the spectral maximum, $\alpha = 0.2$ is the regularization parameter, $p_M(t)$ is the dependence of the impact parameter of the model reflected signal versus time, and $\delta p(t)$ is the radio holographic error estimate of the impact parameter. It is better to estimate the background spectrum density \tilde{u}_{bkg} from the impact parameter interval of $[1.0, 2.0]$ km, where a signal from direct ray is present: this allows for suppressing random maxima that are weak with respect to the direct ray. The additional exponential factor in the definition of I'_R penalizes profiles deviating too much from the model. The averaging in this factor is spread over the whole domain, where the reflected bending angle profile is evaluated.

This reflection index definition is simple to implement and not computationally expensive. On the other hand, such an index is a functional of a process containing a random component (noise, turbulence effects etc.) and deterministic regular structures (direct and reflected ray). The index characterizes the intensity and the sharpness of the reflected ray. Being a functional of a random process, the index is itself a random quantity with its own distribution. None index, under these conditions, can exactly characterize the regular structure in 100% cases. Instead, it characterizes the probability of reflection occurrence. Practically, the use of the index is accompanied by setting a threshold. The events with the index below the threshold are rejected, the remaining events are treated as those containing reflection. The higher the threshold is chosen, the higher is the probability, and the less

events will pass the threshold. Practically the threshold is chosen from the comparison of the index with the visual investigation of an ensemble of events that is large enough for providing statistically significant results.

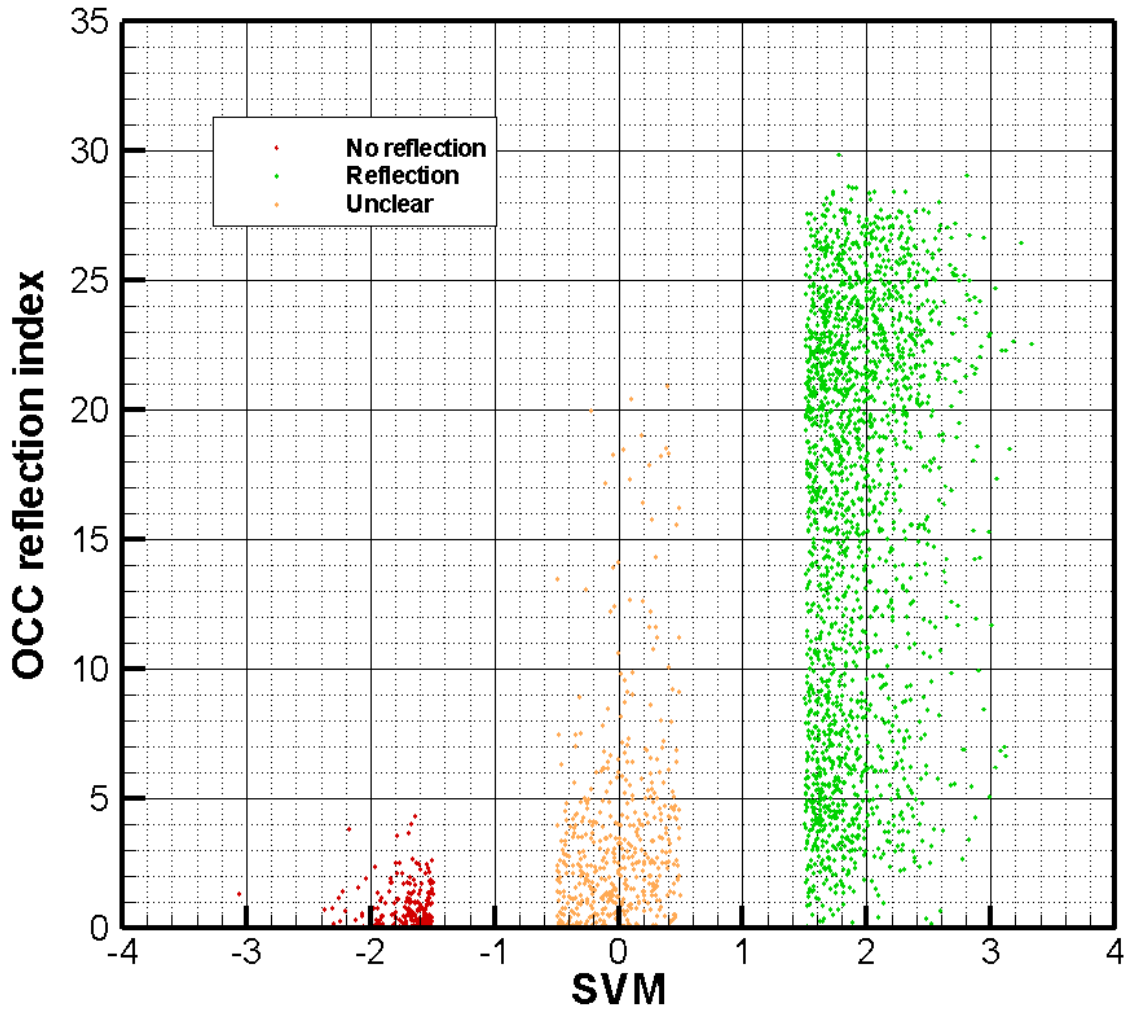


Figure 48. The scatter plot of reflection index SVM versus I'_R for the three categories of events: red – no reflection; green – reflection; orange – unclear.

Figure 48 shows the scatter plot of reflection index SVM versus I'_R for the three categories of events. The lowest values of I'_R correspond to no-reflection cases, while the highest ones correspond to reflection cases.

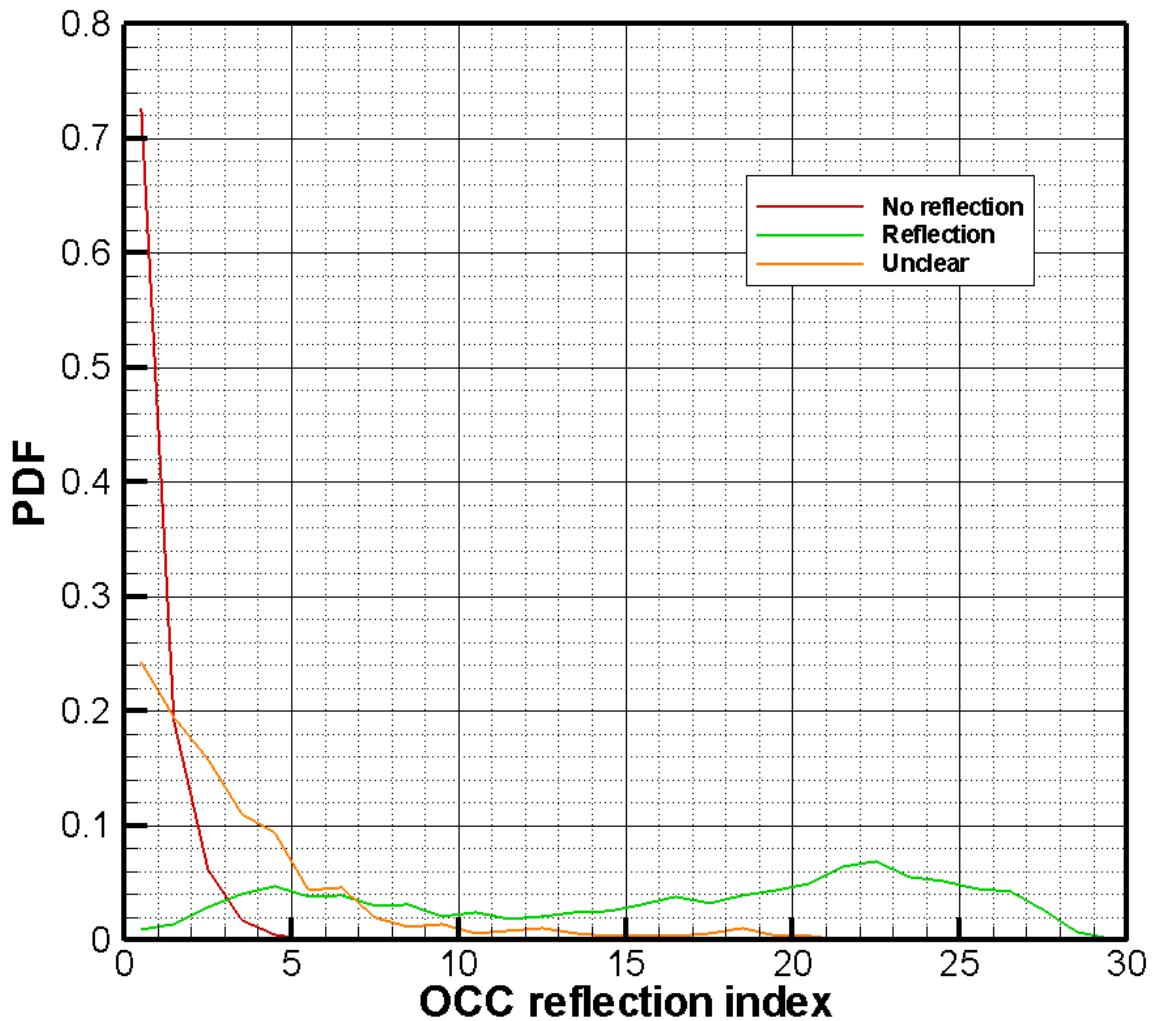


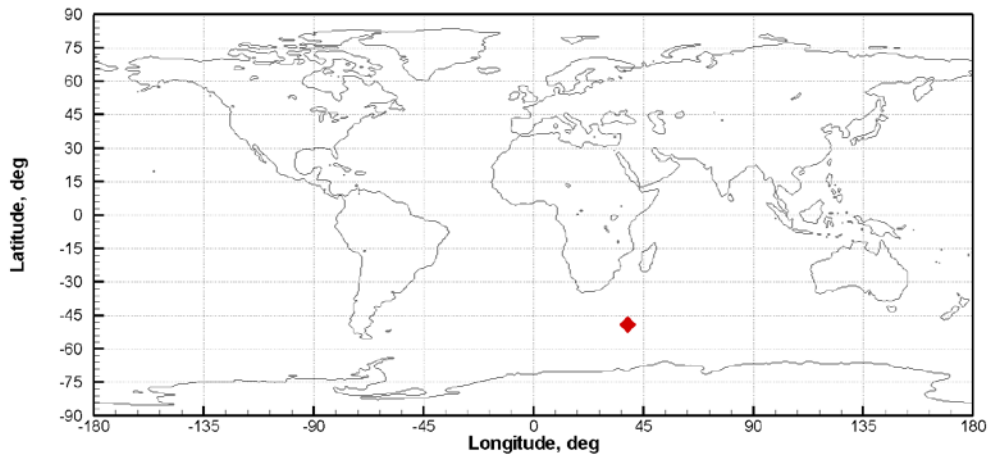
Figure 49. Probability distribution function of I'_R for the three categories of events (same as in Figure 48).

Figure 49 shows the probability distribution function (PDF) of the reflection index I'_R for the three categories of events. For the no-reflection category, the PDF has a strong maximum for events with the index below 1. For the reflection cases, the PDF has a tail for indexes below 3. At $I'_R = 3$, the PDFs for no-reflection and reflection cases have an equal magnitude. This allows for taking the value of 3 as a lowest threshold. About 5% of events classified as clear reflection will be rejected by this threshold. At $I'_R = 5$, the PDF of no-reflection cases reaches 0. This allows for taking the value of 5 as the highest (safe) threshold. About 10% of events classified as clear reflection will be rejected by this threshold.

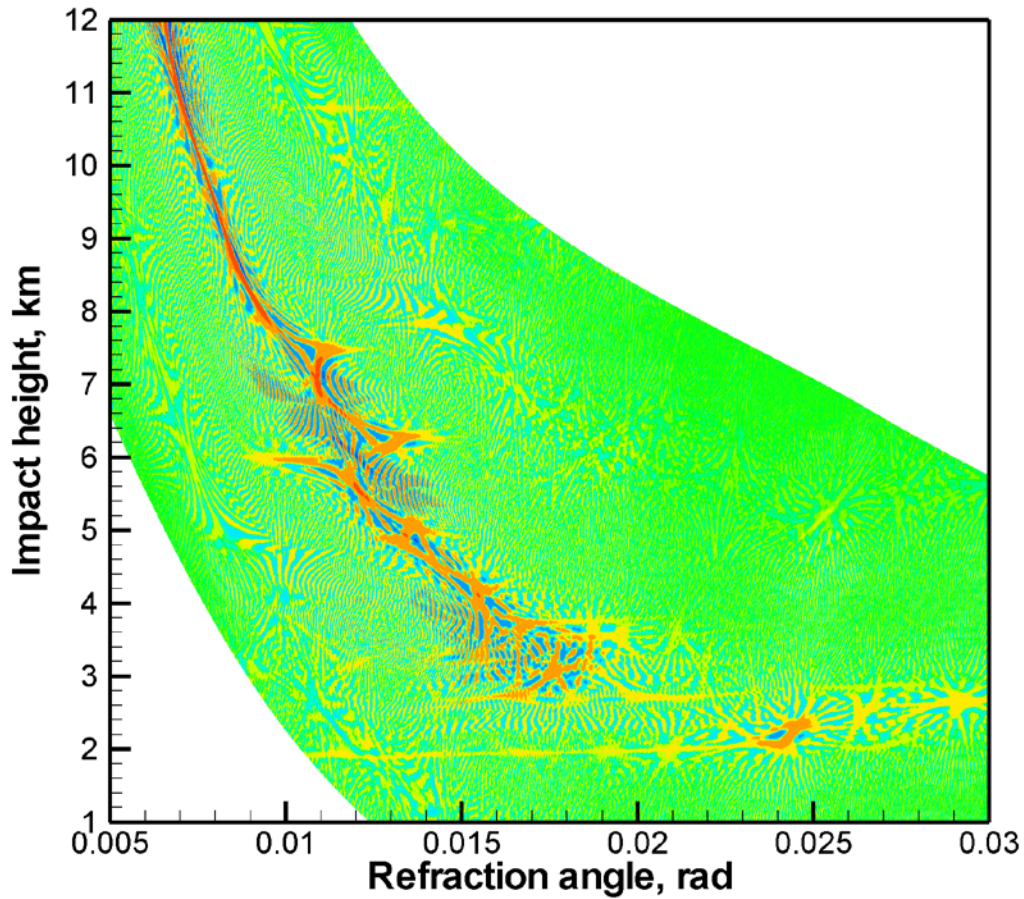
Below, we will consider a few anomalous cases corresponding to the distribution tails.

(1)

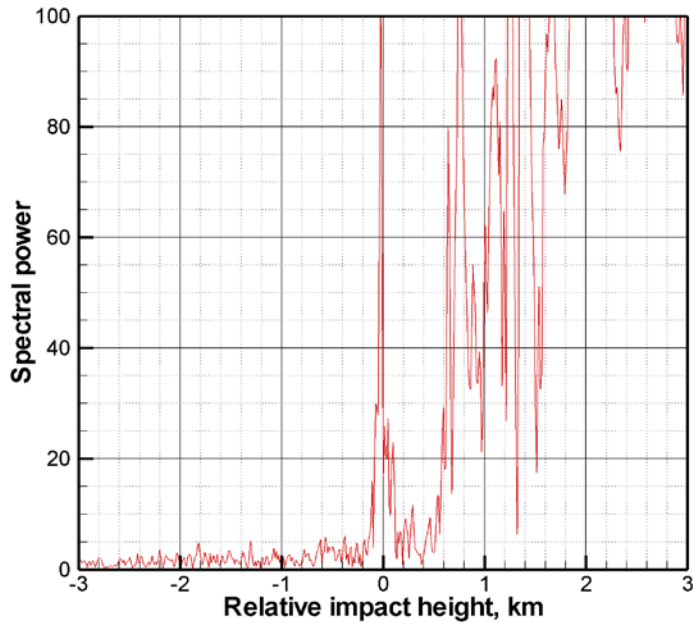
2008/11/01; 23:23:48.000; 49.29S 38.51E; 18.224



(2)



(3)



(4)

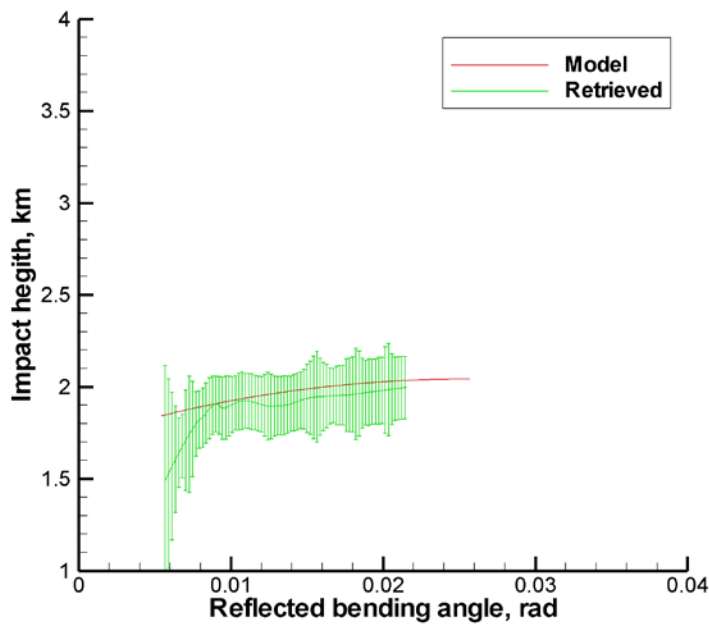
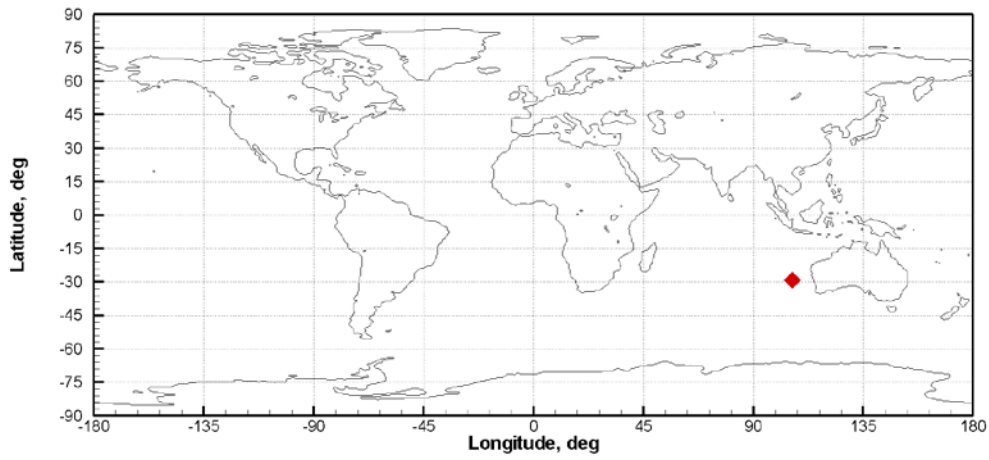


Figure 50. Occultation event with reflection classified as unclear. Reflection index 18.224. Panels from top to bottom: (1) location map, (2) WDF, (3) radio holographic spectrum, and (4) model and retrieved reflected bending angles with radio holographic error estimates.

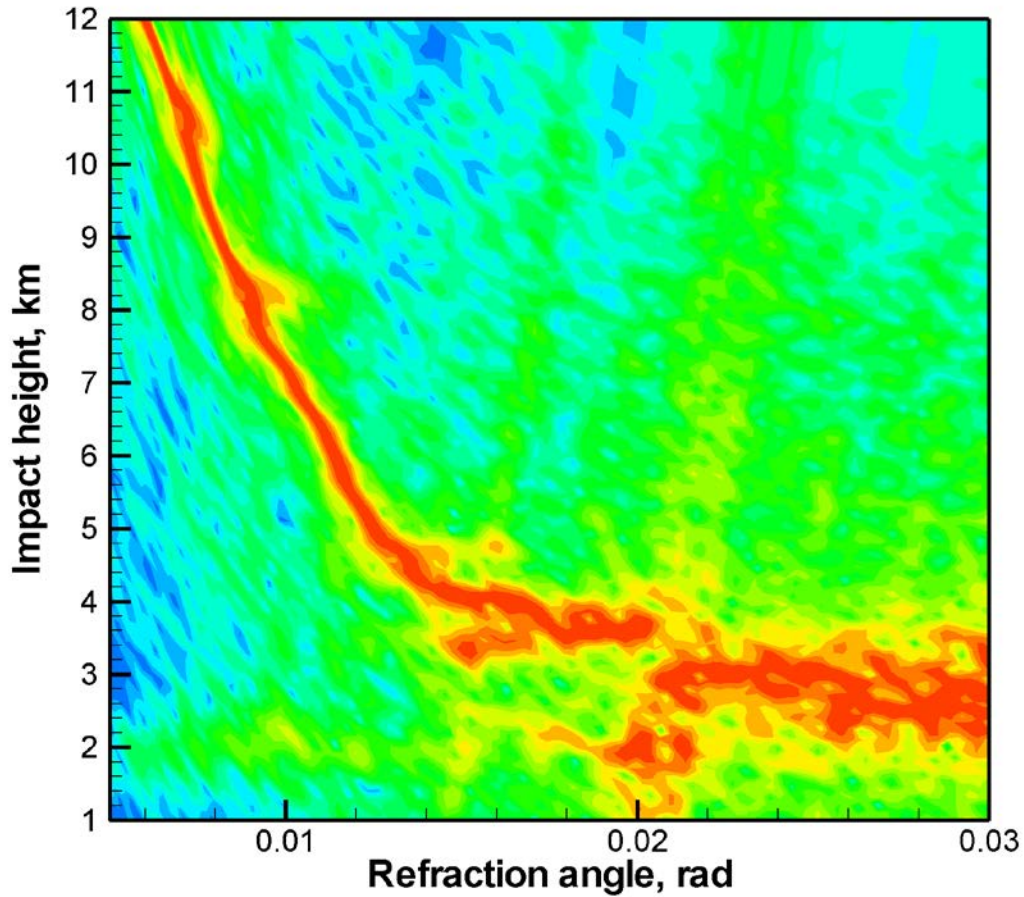
Figure 50 shows an example of event classified as unclear. Our algorithm gave this event the reflection index as large as 18.224. The visual inspection of the plot supports the conclusion that this event does indicate a strong and clear reflection over the ocean.

(1)

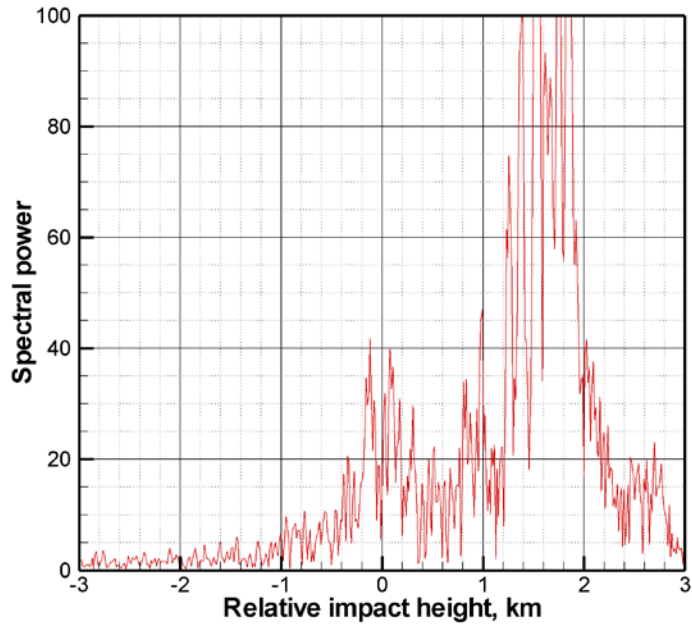
2008/11/01; 06:38:59.000; 29.19S 106.00E; 1.335



(2)



(3)



(4)

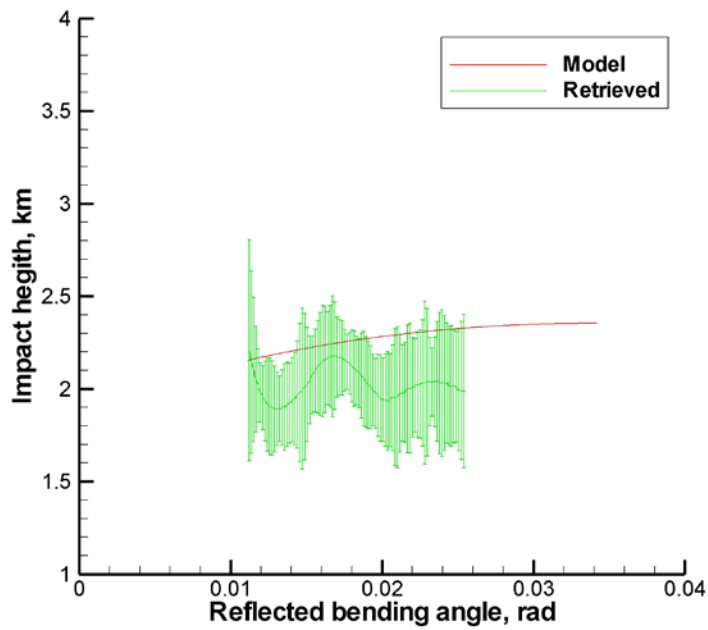
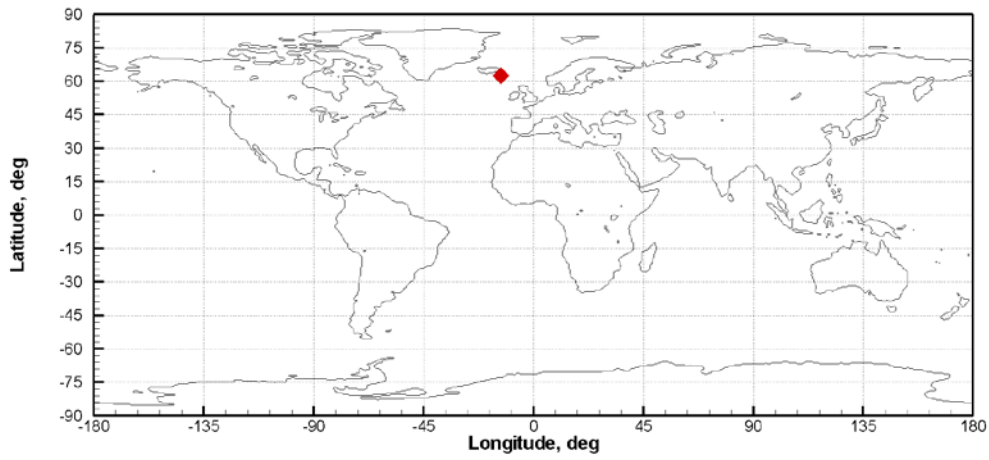


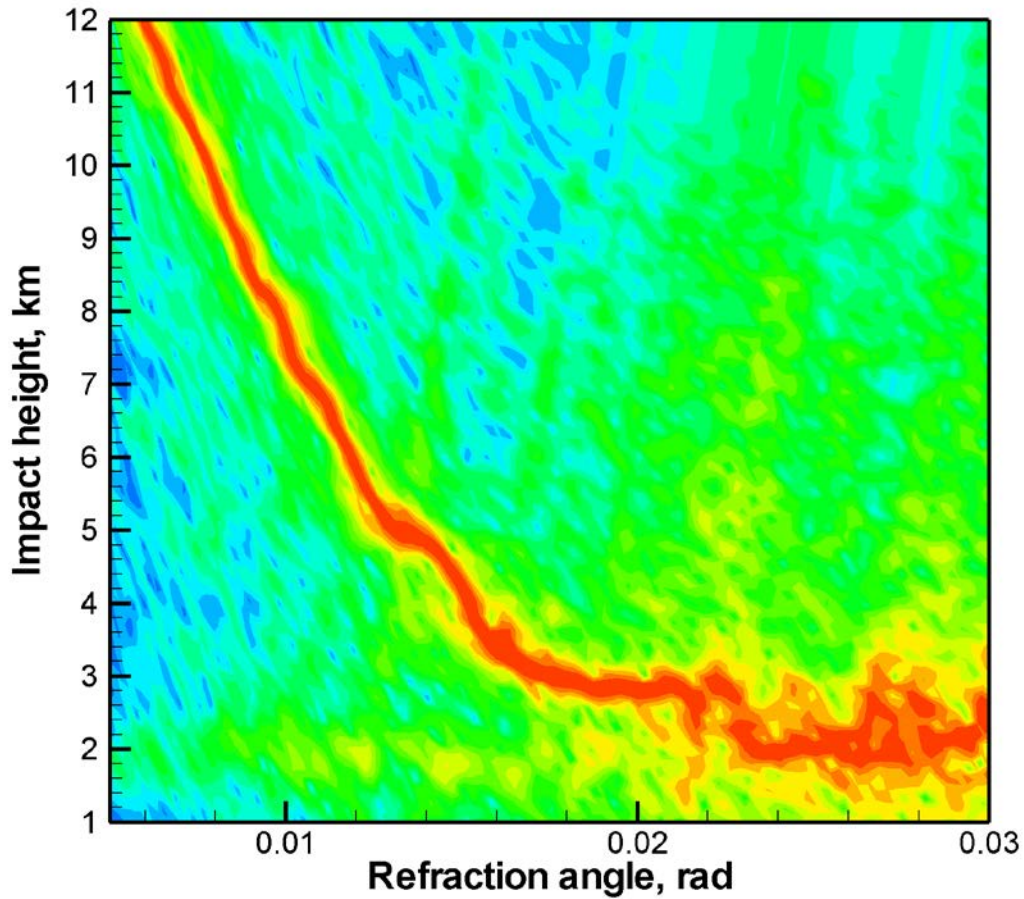
Figure 51. Occultation event with weak reflection classified as clear reflection. Reflection index 1.335. Panels from top to bottom: (1) location map, (2) spectrogram, (3) radio holographic spectrum, and (4) model and retrieved reflected bending angles with radio holographic error estimates.

(1)

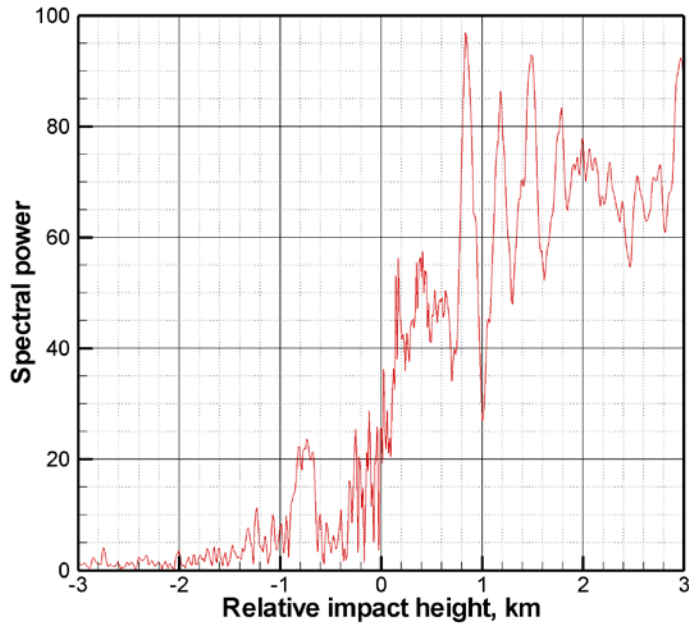
2008/11/01; 11:42:39.000; 62.63N 13.19W; 0.480



(2)



(3)



(4)

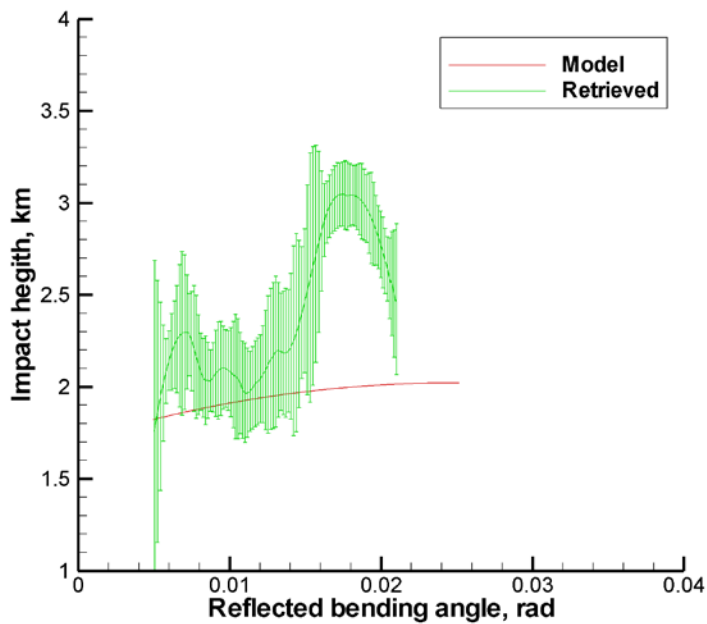
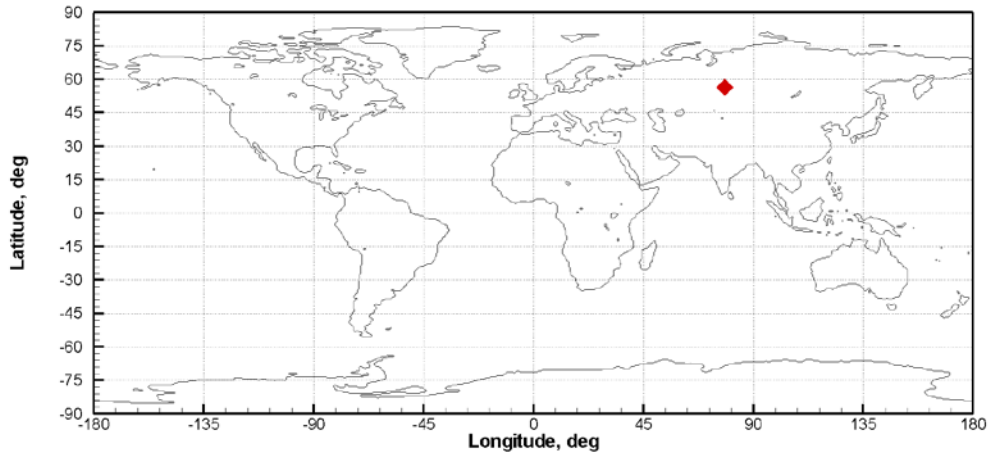


Figure 52. Occultation event with weak reflection classified as clear reflection. Reflection index 0.480. Panels from top to bottom: (1) location map, (2) spectrogram, (3) radio holographic spectrum, and (4) model and retrieved reflected bending angles with radio holographic error estimates.

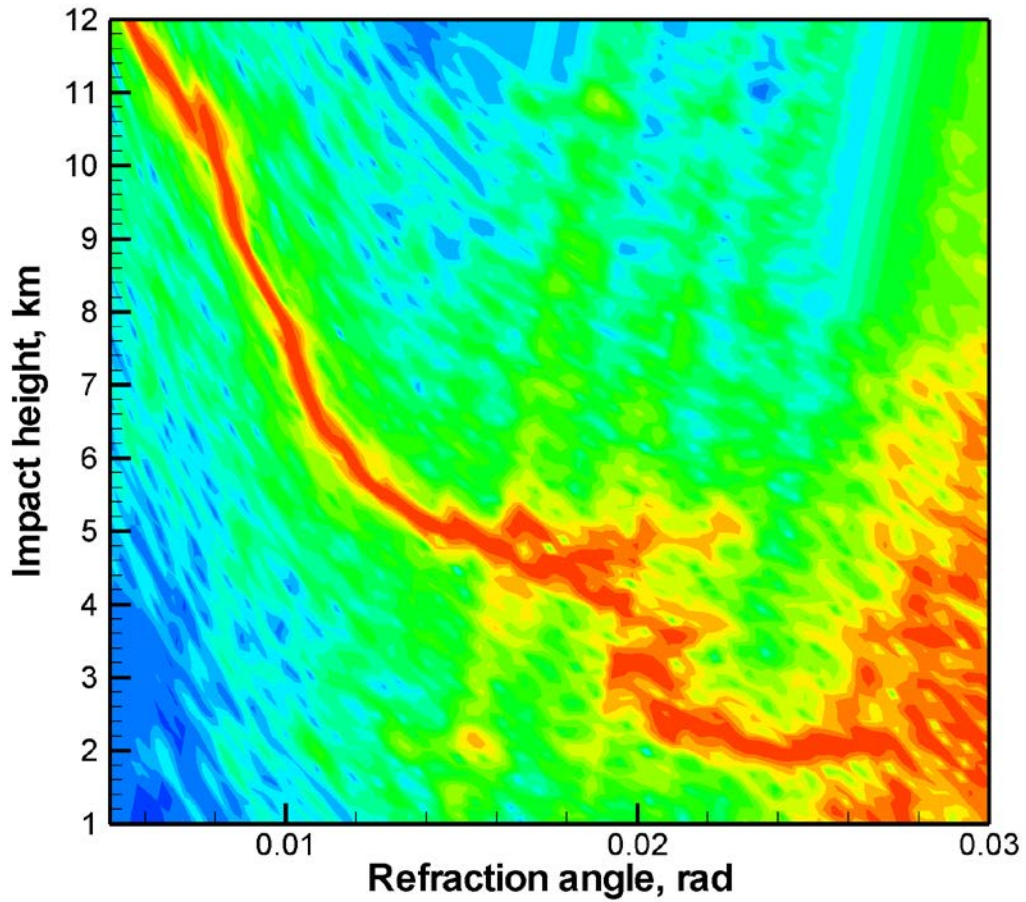
Figure 51 and Figure 52 show two occultation events classified as clear reflection. Our algorithm gave these events as low reflection indices as 1.335 and 0.480. The spectrogram shows that these events indicate weak, blurred, and intermittent reflection pattern, which is not clearly seen in WDF and is better visualized by the spectrogram. Such events could have been classified as unclear ones.

(1)

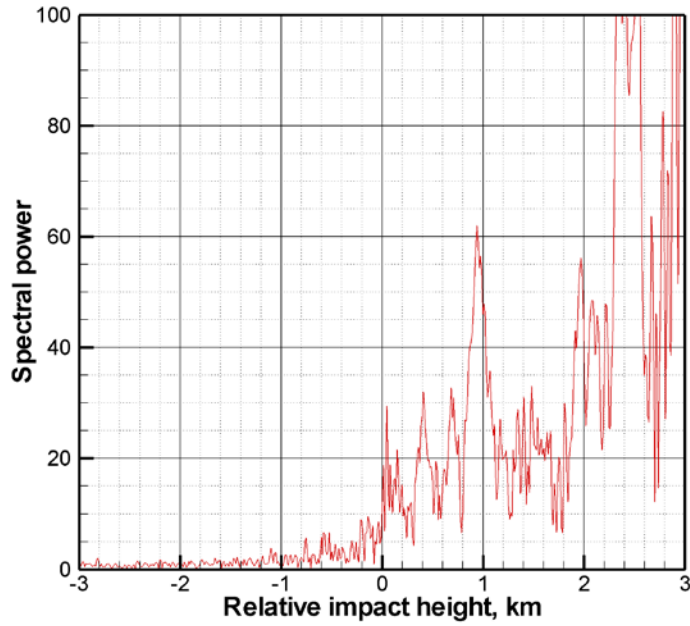
2006/07/31; 12:48:19.000; 56.40N 78.42E; 4.304



(2)



(3)



(4)

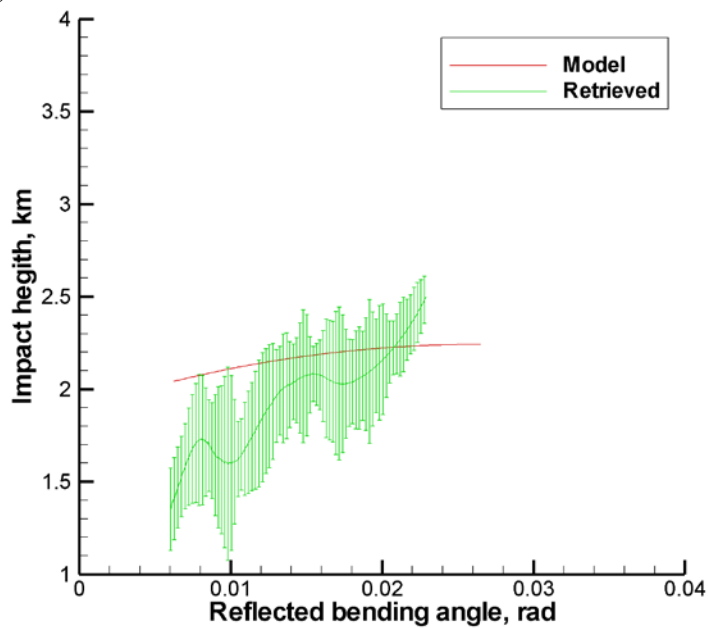
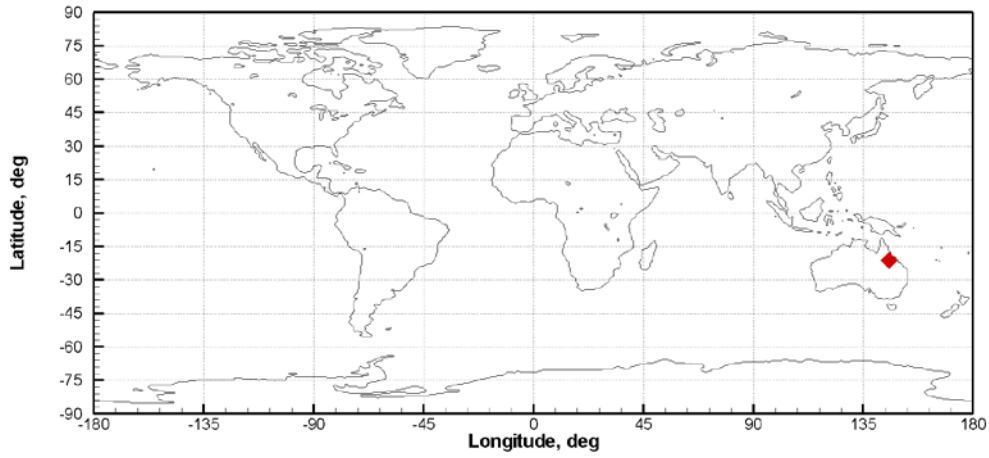


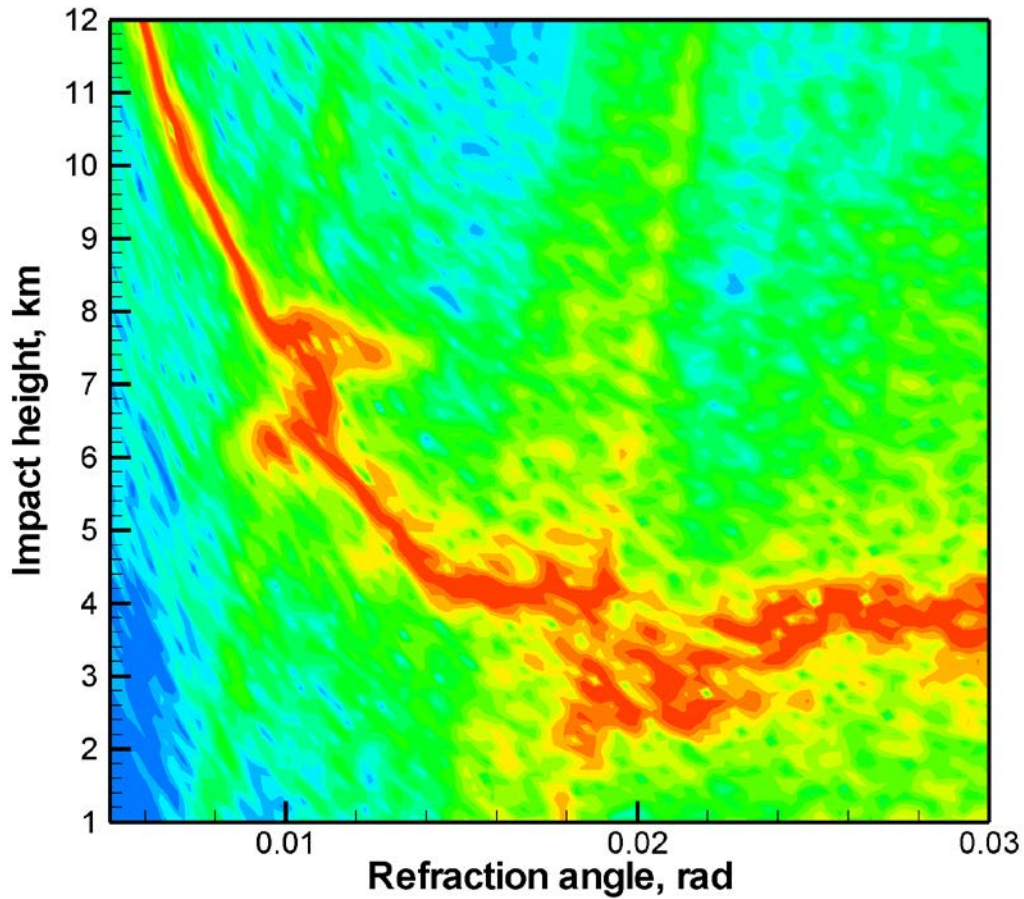
Figure 53. Occultation event without reflection classified as no reflection. Reflection index 4.304. Panels from top to bottom: (1) location map, (2) spectrogram, (3) radio holographic spectrum, and (4) model and retrieved reflected bending angles with radio holographic error estimates.

(1)

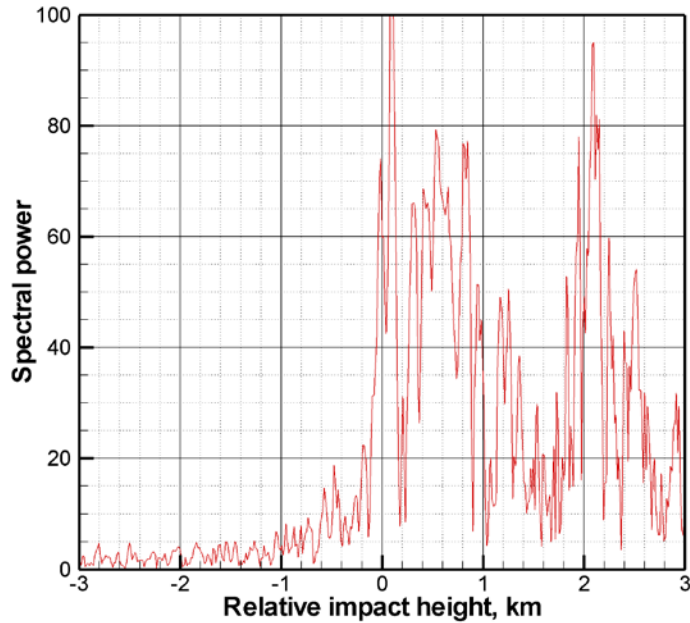
2007/08/09; 07:57:51.000; 21.10S 145.62E; 3.172



(2)



(3)



(4)

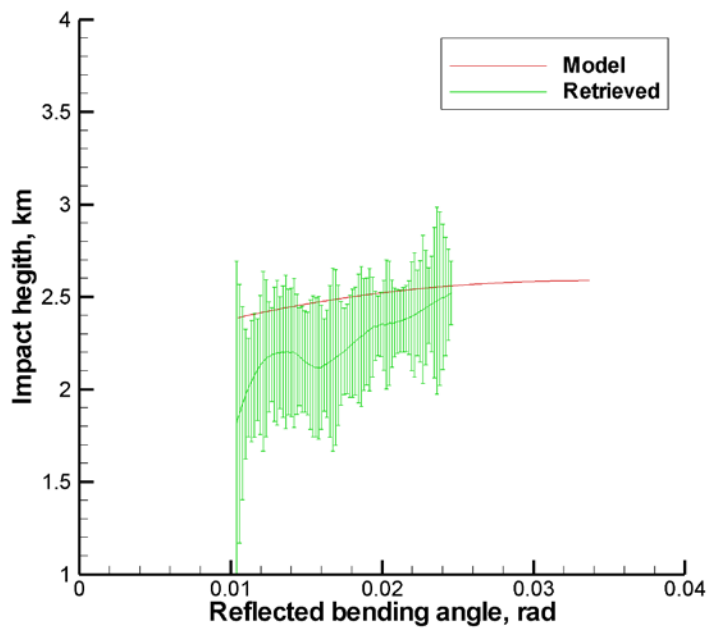


Figure 54. Occultation event without reflection classified as no reflection. Reflection index 3.172. Panels from top to bottom: (1) location map, (2) spectrogram, (3) radio holographic spectrum, and (4) model and retrieved reflected bending angles with radio holographic error estimates.

Figure 53 and Figure 54 show two events without reflection, classified as no reflection cases. Our algorithms gave these events as high reflection indices as 4.304 and 3.172. These values are located at the PDF tail and are explained by the random nature of the RO signals.

This allows for the following conclusions. Our results, in general, indicate a good agreement with the ROM SAF database. There are, still, some event the misclassify by the database. This can be explained by subjective, human factor when processing large series of events. There are also some cases where our algorithm overrates reflection index. These are explained by the random nature of radio occultation signal resulting in the fact that the reflection index is also a random value with its own probability distribution.

8. Conclusions

In this report, we described our modification of the CT technique for the retrieval of bending angle profiles of reflected rays. Our approach uses the combination of the filtering in the impact parameters space with the standard GO retrieval. The filtering uses the FIO in order to map the observed wave field to the impact parameter space. The field in the transformed space is multiplied with the filter function which suppresses the direct ray and let only pass both the not aliased and aliased components of the reflected ray. The filtered field is mapped back to the time domain. The phase of the resulting field is re-accumulated in the vicinity of the phase model of the reflected ray.

We use the radio holographic spectra in order to estimate the reflection index and the expected error of the impact parameter. The reflection index characterizes the strength of the reflection. We validated our reflection index definition by a comparison with the ROM SAF database. In general, our reflection index indicates a good agreement with the database. Some discrepancies are partly explained by the misclassification of some events in the database, and partly by the random nature of RO signals resulting in an overrated reflection index for some tropical events. These events are located on the distribution tails. Based on this comparison, it is possible to estimate the threshold values of the reflection index. Its values exceeding 5 allow for speaking about a definite presence of reflection. Its values below 3 are typical for the absence of reflection. Values between 3 and 5 may correspond to different cases with likely or unlikely reflection.

8.1 Acknowledgments

The work on Chapters 1 and 4–6 was supported by EUMETSAT and ROM SAF CDOP-2 funds in the framework of the Visiting Scientist program (VS-27). The work on Chapter 2 and 7 was supported by Russian Science Foundation (grant RSCF No. 14-27-00134). The work on Chapter 3 was supported by Russian Foundation for Basic Research (grant RFBR No. 16-05-00358 A).

9. References

- 1 Beyerle, G. & Hocke, K. (2001), 'Observation and Simulation of Direct and Reflected GPS Signals in Radio Occultation Experiments', *Geophys. Res. Lett.* **28**(9), 1895–1898.
- 2 Beyerle, G.; Hocke, K.; Wickert, J.; Schmidt, T.; Marquardt, C. & Reigber, C. (2002), 'GPS Radio Occultations with CHAMP: A Radio Holographic Analysis of GPS Signal Propagation in the Troposphere and Surface Reflections', *J. Geophys. Res.* **107**(D24), 27-1–27-14.
- 3 Cardellach, E., C.O. Ao, M. de la Torre-Juárez, and G.A. Hajj (2004), Carrier phase delay altimetry with GPS-reflection/occultation interferometry from low Earth orbiters, *Geophys. Res. Letters*, **31**, L10402, doi:10.1029/2004GL019775.
- 4 Cardellach, E., S. Oliveras, and A. Rius (2008), Applications of the Reflected Signals Found in GNSS Radio Occultation Events, Proceedings of GRAS SAF Workshop on Applications of GPS radio occultation measurements, ECMWF, Reading, UK 16-18 June 2008. <http://www.ecmwf.int/publications/>
- 5 Cardellach, E., S. Oliveras, and A. Rius, GNSS Signal Interference Classified by means of a Supervised Learning Method Applied in the Time-Frequency Domain, IEEE Proceedings of 2009 2nd International Congress on Image and Signal Processing, Tijuana, China, 17-21 October 2009, published by Institute of Electrical and Electronic Engineers, ISBN 13: 978-1-4244-4130-3.
- 6 E. Cardellach, S. Oliveras and A. Rius, Tropospheric Information Content Embedded in GNSS RO Reflected Signals, The International Beacon Satellite Symposium BSS2010.
- 7 Cardellach, E., S. Oliveras, and A. Rius, GNSS Signal Interference Classified by means of a Supervised Learning Method Applied in the Time-Frequency Domain, IEEE Proceedings of 2009 2nd International Congress on Image and Signal Processing, Tijuana, China, 17-21 October 2009, published by Institute of Electrical and Electronic Engineers, ISBN 13: 978-1-4244-4130-3.
- 8 Jensen, A. S.; Lohmann, M. S.; Benzon, H.-H. & Nielsen, A. S. (2003), 'Full Spectrum Inversion of Radio Occultation Signals', *Radio Sci.* **38**(3), 6-1--6-15.
- 9 Jensen, A. S.; Lohmann, M. S.; Nielsen, A. S. & Benzon, H.-H. (2004), 'Geometrical Optics Phase Matching of Radio Occultation Signals', *Radio Sci.* **39**(3), RS3009.
- 10 Gorbunov, M. E. (2002), 'Radio-Holographic Analysis of Microlab-1 Radio Occultation Data in the Lower Troposphere', *J. Geophys. Res. - Atm.* **107**(D12), 7-1--7-10.
- 11 Gorbunov, M. E. (2002), 'Radioholographic Analysis of Radio Occultation Data in Multipath Zones', *Radio Sci.* **37**(1), 14-1–14-9.
- 12 Gorbunov, M. E.; Lauritsen, K. B. & Leroy, S. S. (2010), 'Application of Wigner Distribution Function for Analysis of Radio Occultations', *Radio Science* **45**, RS6011.
- 13 M. E. Gorbunov, K. B. Lauritsen, S. S. Leroy, Analysis of RO data retrieved from the Wigner distribution function, International Radio Occultation Working Group, 2nd Workshop, 28th March – 3rd April 2012, Stanley Hotel in Estes Park, CO, USA, 2012.

- 14 M. E. Gorbunov, Canonical transform method for processing GPS radio occultation data in lower troposphere, *Radio Science*, 2002, 37(5), 10. 1029/2000RS002592, 9-1–9-10.
- 15 M. E. Gorbunov and K. B. Lauritsen, Analysis of wave fields by Fourier Integral Operators and its application for radio occultations, *Radio Science*, 2004, 39(4), RS4010, doi:10. 1029/2003RS002971.
- 16 M. E. Gorbunov, K. B. Lauritsen, A. Rhodin, M. Tomassini, L. Kornblueh, Radio holographic filtering, error estimation, and quality control of radio occultation data, *Journal of Geophysical Research*, 2006, V. 111, No. D10, D10105, doi: 10. 1029/2005JD006427.
- 17 M. E. Gorbunov and K. B. Lauritsen, Radio Holographic Filtering of Noisy Radio Occultations, in: *Atmosphere and Climate Studies by Occultation Methods*, editors: U. Foelsche, G. Kirchengast, A. Steiner. – Springer, Berlin, Heidelberg, New York, 2006. – p. 127–134.
- 18 M. Gorbunov, Wave Optics Propagator Package: Description and User Guide, Technical Report for CONTRACT EUM/CO/10/460000812/CJA Order 4500005632, 2011.
- 19 E. Cardellach, J. Ma. Aparicio, H. Rodríguez: Preliminary assessment report on potential atmospheric products based on RO reflection inversion, ROM-043 Scientific Report, ROM SAF 2015.
- 20 M. E. Gorbunov, A. V. Shmakov, S. S. Leroy, and K. B. Lauritsen, COSMIC radio occultation processing: Cross-center comparison and validation, *Journal of Atmospheric and Oceanic Technology*, 2011, V. 28, No. 6, 737–751, doi: 10.1175/2011JTECHA1489.1.

10. List of Acronyms

BA	Bending Angle
CHAMP	Challenging Mini-Satellite Payload
COSMIC	Constellation Observing System for Meteorology, Ionosphere, and Climate
CT	Canonical Transform
CT2	Canonical Transform of Type 2
ECMWF	European Centre for Medium-range Weather Forecasts
EUMETSAT	EUropean organisation for the exploitation of METeorological SATellites
FIO	Fourier Integral Operator
FSI	Full-Spectrum Inversion
GNSS	Global Navigation Satellite System
GO	Geometrical Optics
GPS	Global Positioning System (USA)
GPS/MET	GPS/Meteorology
GRAS	GNSS Receiver for Atmospheric Sounding (on Metop)
Metop	Meteorological Operational Satellite
NetCDF	Network Common Data Form
NWP	Numerical Weather Prediction
PDF	Probability Distribution Function
PM	Phase Matching
RO	Radio Occultation
ROM SAF	Radio Occultation Meteorology (ROM) Satellite Application Facility (SAF) (EUMETSAT)
WDF	Wigner Distribution Function
WO	Wave Optics
WOP	Wave Optical Propagator